PRODUCTION AND DISTILLATION OF THE THERAPEUTIC RADIONUCLIDE ASTATINE-211 AT THE TEXAS A&M CYCLOTRON INSTITUTE

A Dissertation

by

THOMAS MICHAEL MARTIN

Submitted to the Office of Graduate and Professional Studies of
Texas A&M University
in partial fulfillment of the requirements for the degree of

DOCTOR OF PHILOSOPHY

Chair of Committee,	Gamal Akabani
Committee Members,	Craig Marianno
	John W. Poston, Sr.
	Michael Deveau
Head of Department,	Yassin Hassan

August 2017

Major Subject: Nuclear Engineering

ABSTRACT

The use of the alpha particle emitting radionuclide ^{211}At for clinical therapy of primary and metastatic tumors via targeted methods is an attractive modality for increasing cancer management and survivability. While the potential for therapeutic use is great, widespread commercial production capability of ^{211}At is currently very limited. Development of targetry and distillation apparatus utilizing commercially available and/or easily adaptable technology is of paramount importance in developing and maintaining the preclinical and clinical availability of ^{211}At. Previous preliminary studies have proven the feasibility of ^{211}At production at the Texas A&M Cyclotron Institute utilizing the ^{209}Bi (α, 2n) ^{211}At reaction. The goal of this research is to further develop routine ^{211}At production equipment and methods to facilitate ongoing *in vitro, in vivo,* and preclinical research.

Drawing from previous research, an inclined external solid target was developed capable of undergoing extended (8+ h) irradiations of 29-MeV (7.25 MeV u^{-1}) alpha particles at currents up to 7 μA_e. A dry distillation apparatus and process were developed to recover the astatine while negating radiochemical contamination from target byproduct materials. Several production irradiations were performed with favorable results. Production yields ranged between 10.73 – 39.17 MBq μA_p^{-1} h^{-1} (0.290 – 1.058 mCi μA_p^{-1} h^{-1}), consistent with published yields, at average beam intensities on the order of 5-10 times that used in previous experiments (2-3 μA_p). Recovered yields were on the order of 740 MBq (20 mCi) per production run after initial development (median 22.09 mCi ±

0.77). No contamination by ^{210}At or ^{210}Po was detected in any of the experiments performed.

Overall, production utilizing these methods has proven feasible for small-scale studies utilizing 1-20 mCi per experiment. Development of further process automation and miniaturization, as well as quality assurance and current good manufacturing process (cGMP) protocols, will be required for forthcoming standardized production. Proposed improvements and protocols are provided for future work.

ACKNOWLEDGEMENTS

I would like to thank my committee chair, Dr. Gamal Akabani, for his guidance and backing throughout the course of this research. Without his dedication and care, none of this would have been possible.

Next, I would like to thank the faculty and staff of the Cyclotron Institute for their assistance and support in completing this research. I would also like to thank the Radiation Safety group at MD Anderson Cancer Center for their support in finishing this project while maintaining a full-time job. I would like to thank my parents for their encouragement all through my academic career.

Finally, thank you to my wonderful wife for her support, patience, and love; to my children, for their love and the motivation they have provided to finish what I started; and to God, for providing this opportunity and all that I have and have accomplished.

CONTRIBUTORS AND FUNDING SOURCES

This work was directed by a dissertation committee consisting of Professor Gamal Akabani and Professors Craig Marianno and John W. Poston, Sr. of the Department of Nuclear Engineering, and Professor Michael Deveau of the Department of Veterinary Medicine.

All work for the dissertation was completed by the student, under the advisement of Dr. Gamal Akabani of the Department of Nuclear Engineering.

Graduate study was partially funded by the Department of Energy, grant numbers DE-SC0007371 and DE-SC0008433, and supported in part by assistantships from Texas A&M University. The content of this research is the sole responsibility of the authors and do not necessarily represent the official views of the Department of Energy.

NOMENCLATURE

AuNP	Gold nanoparticle(s)
cGMP	Current good manufacturing practices
CRPC	Castration-resistant prostate cancer
DSB	Double strand break(s)
FDA	United States Food and Drug Administration
FWHM	Full width at half maximum
EOB	End of bombardment
HNSCC	Head and neck squamous cell carcinoma
IRBRB	Interdisciplinary radioisotope production and radiochemistry program
ISO	International organization for standardization
LET	Linear energy transfer
mAb	Monoclonal antibody(ies)
μA_e	Electrical microampere
μA_p	Particle microampere
RBE	Relative biological effectiveness
RCP	Radionuclidic purity
RCY	Radiochemical yield
TRT	Targeted radionuclide therapy
USP	United States pharmacopeia

TABLE OF CONTENTS

LIST OF FIGURES

Page

LIST OF TABLES

Page

1. INTRODUCTION

The use of the alpha-particle-emitting radionuclides for clinical therapy of primary tumors and metastatic disease via targeted methods is an attractive modality for increasing the therapeutic effectiveness of cancer treatments. One of the most promising of these radionuclides for the development of targeted therapy is ^{211}At. Primary advantages of this radionuclide are the clinically useful physical half-life of 7.214 h, as well as the low range in tissue and high linear energy transfer (LET) of its alpha particle emissions. These characteristics lead to high cytotoxicity, independent of physiological or metabolic oxygen levels, lack of dose rate effects, and reduced or negligible dose to non-targeted tissues. The resulting high relative biological effectiveness (RBE), coupled with well-known halogen chemistry, lends ^{211}At to immunoconjugation and targeted delivery utilizing monoclonal antibodies or novel colloidal nanoparticle techniques. While the potential for therapeutic use is great, widespread production of alpha-particle emitting radionuclides is currently very limited. To increase the availability of this radionuclide, design and implementation of targetry and distillation equipment must be completed at the few facilities capable of producing ^{211}At in sufficient quantities for on-going preclinical and clinical research.

1.1 Molecular Radiotherapy of Primary and Disseminated Disease

Molecular radiotherapy or targeted radionuclide therapy (TRT) using immunoconjugation, small molecule drugs, and nanoparticle delivery strategies, are attractive modalities for the treatment of cancer. These modalities enable the delivery of therapeutic levels of radiation to diseased tissue while leaving healthy tissue relatively unharmed (Williams et al. 2008, Ting et al. 2009, Ting et al. 2010). Radionuclides utilized for TRT are conjugated to biologically active molecules, such as peptides or monoclonal antibodies, or molecules with specific organ uptake, such as colloidal nanoparticles. Targeting molecules preferentially bind to cancer cells by targeting tumor-specific antigens or other over-expressed cell surface receptors (Chattopadhyay et al. 2010, Yang et al. 2011). In general, TRT strategies have focused on the attachment of one or more radioactive nuclei to a single targeting molecule (Williams et al. 2008). The recent utilization of nanomaterials has made it possible to attach several radioactive nuclei to multiple targeting molecules, potentially increasing target specificity and therapeutic efficacy (Panchapakesan and Wickstrom 2007, Ting et al. 2009, Jokerst et al. 2011, Nduom et al. 2012). Based on their unique targeting properties, in addition to treating solid tumors, these molecules may find value in treating disseminated and systemic disease.

1.2 Alpha-Particle-Emitting Radionuclides Used in Molecular Radiotherapy

The development of molecular radiotherapy or TRT drugs utilizing alpha-particle-emitting radionuclides is particularly desirable due to increased efficacy of cell killing of alpha particles when compared to beta particles (Dadachova 2010, Dashko et al. 2010). The majority of United States Food and Drug Administration (FDA) approved TRT drugs utilize the beta emitters ^{90}Y and ^{131}I (Williams et al. 2008, Ersahin et al. 2011). However, the recent acceptance of the drug Xofigo® ($^{223}RaCl_2$), utilizing the alpha emitter ^{223}Ra for the treatment of castration-resistant prostate cancer (CRPC) bony metastases, has shown the usefulness of alpha emitters in TRT (Cheetham and Petrylak 2012).

Alpha particles are generally emitted with energies ranging from 4-6 MeV, as opposed to beta particles, which are emitted with lower maximum energies, on the order of 1-2 MeV. In addition, alpha particles have a maximum range in tissue of approximately 150 μm. The resulting high linear energy transfer (LET) leads to a high density of energy deposition near the particle track, increasing the probability of inactivating critical cell components. This increase leads to a much higher relative biological effectiveness (RBE) and probability of cell death than that obtained with beta-emitting radionuclides or conventional external beam radiotherapy. It is estimated that less than 20% of energy from ^{131}I and less than 2% from ^{90}Y is deposited in tumors of 200 μm diameter. The remaining energy is deposited in surrounding healthy tissue. (Chen et al. 2012). Put another way, 95% of beta energy is deposited within 0.992 mm by ^{131}I, and in 5.94 mm by ^{90}Y (Hopkins et al. 1998, Zalutsky 2004).

Conversely, the range of typical alpha particles is comparable to the dimension of most eukaryotic cell clusters (10-50 μm). Coupled with common alpha-particle ranges, 80-100% of the kinetic energy is deposited within few cells. Therefore, healthy tissue cells surrounding a solid tumor volume may be spared, as the alpha particle and most secondary electrons are incapable of reaching these cells. From a practical standpoint, alpha-particle emitters may be able to sterilize cells via self-irradiation, whereas achieving the same level of cellular effects with beta emitters leads to toxicity effects due to total drug concentration in the body (Sgouros et al. 2010).

1.2.1 Advantages of Astatine-211

Among the many known alpha emitters, only a handful are suitable for use in targeted therapies, including ^{211}At, ^{212}Bi, ^{213}Bi, ^{223}Ra, ^{225}Ac, and ^{227}Th (Guerard et al. 2013). The radionuclide ^{211}At is an ideal candidate for alpha emitter TRT strategies due to its relatively short half-life and desirable decay chain, as shown in Table 1 (Zalutsky et al. 1989, Guerard et al. 2013). Both ^{211}At and its daughter ^{211}Po (branching ratio of 0.582) decay by alpha emission (Lambrecht and Mirzadeh 1985). In addition, several x-rays are emitted during decay, which allow potential *in vivo* imaging and accurate estimation of internal dose distributions (Zalutsky and Pruszynski 2011). Compared to the other radionuclides shown, ^{211}At has the most clinically useful half-life. Half-lives shorter than a few hours prove difficult to manufacture, transport, and administer before significant

decay has occurred. Unlike routinely produced radionuclides with short half-lives used in positron emission tomography, the processing and labeling procedures for therapeutic drugs have not been automatized to the same degree. Half-lives longer than a day or two introduce issues with specific activity, labeling efficiency, and committed doses. At first, the significant energy yield of alpha particles associated with the heavier radionuclides would seem beneficial. However, due to the multiple decays involved, it is likely that daughters will have dissociated from the targeting molecule and been transported away from the tumor site, such that further emissions are ineffective (Palm et al. 2004, Guerard et al. 2013). This is especially true when targeting micro-metastases and cell clusters (Aurlien et al. 2000).

Table 1. Common alpha-particle-emitting radionuclides suitable for molecular radiotherapy and their physical characteristics. Energy yield includes contributions from daughters. Radium, actinium, and thorium have multiple alpha-emitting daughters (Zalutsky et al. 1989, Guerard et al. 2013).

Radionuclide	**Half-life**	**α Energy × Yield (MeV Bq^{-1} s^{-1})**
^{211}At	7.214 h	6.92
^{212}Bi	60.55 m	7.92
^{213}Bi	45.61 m	5.85
^{223}Ra	11.43 d	19.93
^{225}Ac	10.0 d	25.15
^{227}Th	18.68 d	25.79

Astatine-211 is produced via the ^{209}Bi (α, 2n) ^{211}At reaction. Production of the impurity radionuclide ^{210}At competes with this reaction via the ^{209}Bi (α, 3n) ^{210}At reaction (Hermanne et al. 2005, Schultz et al. 2006). The impurity radionuclide ^{210}At decays primarily to the radionuclide ^{210}Po. The decay schemes of ^{211}At and ^{210}At are illustrated in Fig. 1.

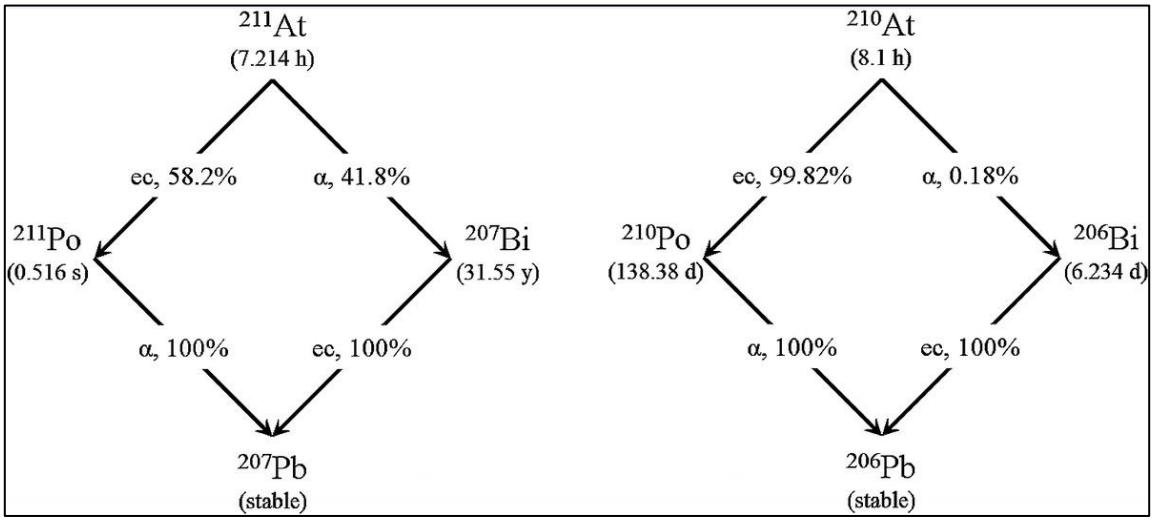

Figure 1. The decay schemes of ^{211}At and ^{210}At. The radionuclide ^{210}At is unsuitable for molecular radiotherapy because of the long half-life of ^{210}Po.

The deposition and retention properties of ^{210}Po, coupled with the high radiotoxicity of this radionuclide, dictate that even trace amounts of ^{210}At impurity present in a sample of ^{211}At will make the product unfit for pre-clinical use (Schultz et al. 2006, Scott 2007, Ansoborlo et al. 2012). To minimize production of ^{210}At, the nominal incident alpha particle beam energy must be maintained below the 28.6 MeV threshold, where the cross-section for ^{210}At production is minimal while ^{211}At production cross-section remains substantial (cf. Fig. 2) (Lambrecht and Mirzadeh 1985, Hermanne et al. 2005, Martin et

al. 2014). The theoretical lower threshold for ^{211}At production is 20.72 MeV (Morzenti et al. 2008).

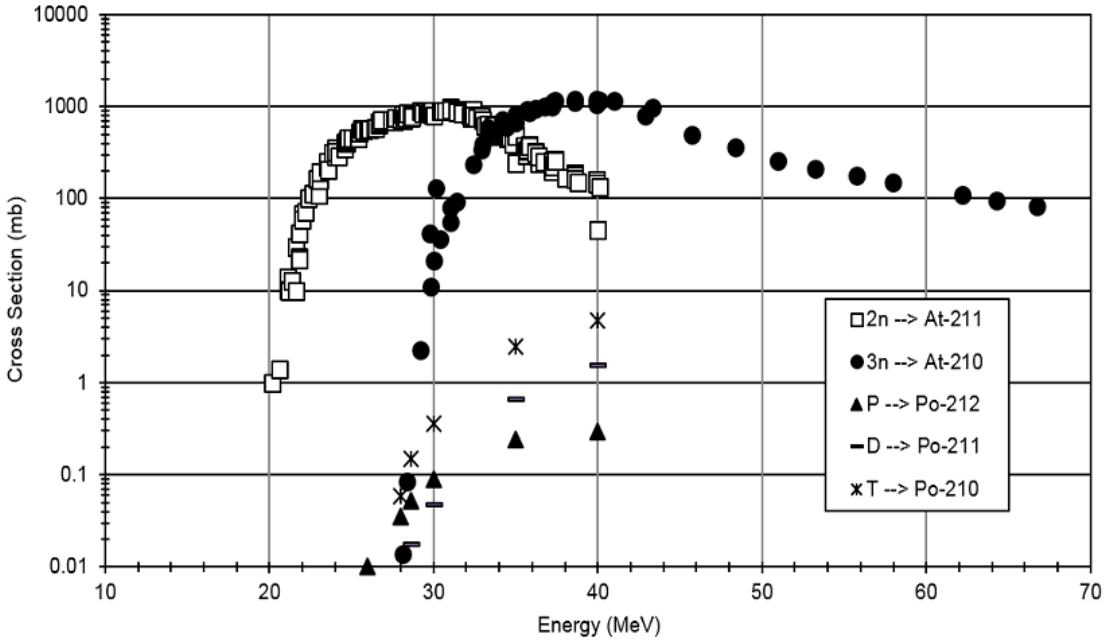

Figure 2. Excitation functions for the most probable reactions are shown for ^{4}He nuclei incident on ^{209}Bi. Cross sections were extracted from JANIS, using data from Kelly 1949, Ramler et al. 1959, Lambrecht et al. 1984, Patel et al. 1992, Hermanne et al. 2004, and TENDL 2009 (JANIS 2016).

1.2.2 In-Vitro, In-Vivo, and Pre-Clinical Use of Astatine-211

There have been many studies geared towards the preclinical use of ^{211}At, mostly focusing on immunoconjugation for radioimmunotherapy. Initial studies incorporating *in vitro* research have been translated into *in vivo* use; a few of these studies have progressed

to pre-clinical trials stage. An overview of the most widely received of these studies is provided below.

Early *in vitro* studies have shown survival fractions of 0.37 (D_0) occurring with one to two nuclear crossings by alpha particles, when conjugated to mAb's targeting human glioma and melanoma cells (Larsen et al. 1998). Similarly, successful results were shown with anti-HER2/anti-CD340 labeled astatine in effective therapy of the breast cancer cell lines SKBr-3, BT-474, and MCF7 (Akabani et al. 2006). Relative biological effectiveness of the trastuzumab (anti-HER2/anti-CD340) labeled astatine showed a relative biological effectiveness on the order of ten times higher than external photon irradiation.

As an alternative to immunoconjugation, one study looked at the effectiveness of 5-[^{211}At]Astato-2'-deoxyuridine for incorporation into DNA. Treatment of Chinese hamster V79 lung fibroblasts showed impressive results; untargeted cells were killed by neighboring cells, and the incidence of double-strand-breaks (DSB) was approximately an order of magnitude higher than what was found for an ^{125}I labeled homolog. Other groups have reported similar findings regarding the incidence of DSB (Lyckesvard et al. 2014). Dosimetry analysis concluded that D_0 levels were reached with 1.2-1.5 decays per cell. DNA incorporation greatly increased the effectiveness and reduced the dependence on nuclear crossing when compared to cell-surface-receptor targeted moieties (Vaidyanathan et al. 1996). Other groups have shown that alpha radiation from ^{211}At results in approximately three times as many DSB as compared to low LET radiation (Claesson et al. 2007).

A similar study was undertaken to compare the efficacy of ^{211}At radiation to more common methods in creating aberrations in thyrocytes. Due to a chemical similarity to iodine, free astatine naturally accumulates in thyroid tissue. This study showed that alpha-particle radiation was more effective in causing damage to stationary and cycling cells when compared to gamma rays from ^{60}Co. This result could lead to ^{211}At use in the treatment of benign thyroid diseases in children with less risk of inducing cancer risks over the long term (Lyckesvard et al. 2014).

More recently, colloidal gold nanoparticles (AuNP) have been investigated for targeted delivery of radionuclides, specifically ^{198}Au and ^{125}I (Kannam et al. 2006, Paciotti et al. 2006, Hamoui 2015). The most interesting research has focused on size control for organ-specific uptake, coupled with mAb or peptide labeling for therapy of micrometastases (Chattopadhyay et al. 2010, Kim et al. 2011, Martin and Akabani unpublished data 2012, Hamoui 2015). Due to the chemical similarity of iodine and astatine, this has been investigated as a method for delivering ^{211}At, as well as in mixed radionuclide theranostic use (Bartczak and Kanaras 2011, Martin and Akabani unpublished data 2012).

Pre-clinical and clinical trials have utilized both locoregional administration as well as systemic intravenously injected drugs. Locoregional administration has the benefit of quick delivery to the tumor cells; de-astatination of delivery proteins, as well as short biological half-lives of some targeting proteins themselves, may limit effectiveness in some moieties unless locally administered. On the other hand, intravenous injection is crucial for treatment of disseminated cancers, including micrometastases and cell clusters.

Anti-CD25 mAb 7G7/B6-labelled astatine was studies as a systemically administered therapeutic agent for leukemia in mice. Favorable results of 70% survival in approximately one and a half months were found, as compared to total population death in the control group in the same amount of time (Zhang et al. 2006a). Further studies investigated the use of this drug in combination therapy with daclizumab, an anti-Tac mAb. This has shown equally favorable results when compared to radionuclide therapy by itself, of 91% survival at three months versus 32% survival for the radionuclide alone. (Zhang et al. 2006b). The same group also studied ^{211}At-HeFi-1, an anti-CD30 mAb, for treatment of leukemia in mice, showing similar survival fractions for combined therapy utilizing daclizumab (Zhang et al. 2007).

A similar methodology was used to investigate ^{211}At-U36, an astatinated mAb which targets antigens widely expressed by squamous cell epithelium and squamous cell carcinomas originating in the neck, head, esophagus, cervix, and epidermis (Schrijvers et al. 1993). This study was used to evaluate treatment of head and neck squamous cell carcinoma (HNSCC) in mice via intravenous injection. There was a reduction of tumor volume in comparison with controls (Cheng et al. 2007). Systemic administration of radioastatine conjugated to smaller proteins, such as the antibody fragment C6.5, targeting HER2 receptors, has also been studied (Robinson et al. 2008).

Loco-regional administration has been studied extensively in the use of the mAb MX35-F(ab')2 labelled ^{211}At in the therapy of ovarian cancers (Andersson et al. 2000, 2003, 2009; Back et al. 2005, 2009; Elgqvist et al. 2006a, 2006b, 2006c, 2010; Frost et al. 2013, Gustaffson et al. 2012). This is important, as the several studies presented below

have led to Phase I clinical trials (Guerard et al. 2013). These studies have focused on ^{211}At-MX35 in the treatment of NIH:OVCAR-3 ovarian cancer cells in murine models. The antibody is effective in other forms of ovarian cancer, as it targets the Le^{y} antigen expressed in the majority of human epithelial ovarian cancers. These groups have studied the effects of tumor size, total administered activity, and fractionation. In general, the astatinated MX35 was found to be more effective in treating smaller tumors, supporting its use in the targeting of microclusters and disseminated disease. For fractionation, little difference was found when splitting doses (maximum of 800 kBq or ~22 μCi) between three equal administrations every four days versus a single dose. However, further studies showed weekly injections of 400 kBq (~11 μCi) per injection showed a significant increase in efficacy when administered three to six times (Elgqvist et al. 2010). The phase-I clinical trials of ^{211}At-MX35 were investigated as an adjunctive therapy for failed cases of phase-III trials. These trials were centered on HMFG1 labeled ^{90}Y for post-surgical treatment of ovarian cancer, which failed in some cases due to the inadequacy of beta-emissions in treating disseminated disease; as such, the alpha-emitting ^{211}At-MX35 proved to be a very promising option, although results are still pending (Guerard et al. 2013).

Another series of studies based on intravenous administration of ^{211}At-81C6 antibodies is equally important and was also taken to phase-I clinical trials (Zalutsky et al. 1994, 1997). The monoclonal antibody 81C6 targets tenascin, an antigen over-presented by gliomas, and has been actively studied in the treatment of apoptosis-resistant brain and central nervous system tumors (Blasberg et al. 1987, Zalutsky 2004, Azad et al. 2015,

Pozzi and Zalutsky 2017). Phase-I clinical trials used the chimeric form of the antibody to reduce possible immunogenicity effect, and focused on the treatment of residual disease following surgery, resulting in a statistically significant increase in median survival without significant short or long-term neurological side effects to date (Zalutsky et al. 2008).

Several other pre-clinical studies have been started. A large effort has been put forth investigating transcriptional response of mice tumors and dose rate effects and dependence *in vivo*. (Rudqvist et al. 2012, 2015). An additional study by this group has investigated response in healthy tissue following administration of ^{211}At. This *in vivo* model assessed transcriptional response in BALB/c nude mice and is a step forward in assessing long-term toxicity effects and side effects to normal tissue during therapy (Langen et al. 2015). More recently, a similar study has investigated the use of compounds targeting overexpressed sigma receptors in DU-145 cells (human prostate cancer) in mice with both ^{131}I and ^{211}At with good results (Ogawa et al. 2015)

1.2.3 Present-day Availability

Despite the attractiveness of ^{211}At for clinical therapeutic use, there are several hurdles that must be overcome prior to its adoption as a clinical radiopharmaceutical. Current production of ^{211}At is limited to a handful of cyclotrons around the world. Furthermore, a recent survey of available cyclotron facilities suggests that there are very

few cyclotrons capable of producing ^{211}At at levels needed for use in pre-clinical and clinical research (Zalutsky and Pruszynski 2011). The Texas A&M University Cyclotron Institute and Interdisciplinary Radioisotope Production and Radiochemistry Program (IRPRP) is one of the few facilities capable of producing ^{211}At at high yields; therefore, establishing routine production of ^{211}At will be a significant step towards overcoming this deficiency. In addition to limited production sources, further development of advanced radiochemical techniques for efficient isolation of ^{211}At is needed to minimize loss and maintain repeatability during post-production processing (Lindegren et al. 2001, Zalutsky et al. 2001, Zalutsky and Pruszynski 2011). Finally, a better understanding of chemical properties, *in vitro* and *in vivo* studies of uptake and retention profiles, as well as extensive pre-clinical trials are required for successful demonstration of the use of ^{211}At in TRT radiopharmaceuticals (Zalutsky et al. 1989, Kennel et al. 2002, Nakamae et al. 2009, Zalutsky and Pruszynski 2011)

1.3 Purpose of This Research

This report describes a routine production study of ^{211}At at the Texas A&M University Cyclotron Institute as part of the efforts of the IRPRP. The IRPRP's mission centers upon the production of radionuclides for use in diagnostic and therapeutic nuclear medicine and radiobiology research, with a primary focus on the development of novel, targeted radionuclide strategies. As the first step of establishing this program for targeted

radionuclide development, preliminary experiments were previously conducted at the Texas A&M Cyclotron Institute to establish the production of ^{211}At (Bhakta 2011, Martin and Akabani 2012, Martin et al. 2014). These initial experiments guided the next step towards routine production, the experiments and results of which are presented in this dissertation.

2. MATERIALS AND METHODS

2.1 Properties of Astatine-211

The radionuclide ^{211}At has a unique set of characteristics which make it suitable for use in targeted therapy. The physical properties of ^{211}At, such as half-life and double alpha-particle-emission combine well with biological effects of its emissions to effectively kill cancer cells.

2.1.1 Physical Properties

The radionuclide ^{211}At is an ideal candidate for therapeutic modalities due to its relatively short half-life of 7.214 h and emissions (Zalutsky et al. 1989). This half-life provides a reasonably high emission rate, while still being long enough to allow efficient tumor uptake and retention. Astatine-211 decays by electron capture to ^{211}Po (branching ratio = 0.582), which in turn decays by alpha particle emission. Alternatively, ^{211}At decays by alpha particle emission to ^{207}Bi, followed by electron capture. The decay scheme of ^{211}At and the impurity ^{210}At are shown in Figure 1. While ^{211}Po is available in the metastable state as ^{211m}Po from other production methods, it is not fed by ^{211}At decay due to high nuclear spin and associated low decay probability (Groppi et al. 2005).

In addition to the double alpha emission, several x-rays are emitted during decay, which allow for *in vivo* imaging and accurate estimation of internal dose distributions (Lambrecht and Mirzadeh 1985, Zalutsky and Pruszynski 2011). The most common emissions and energies are provided in Table 2 (National Nuclear Data Center 2016). More complete decay information is provided in Appendix A.

Table 2. The most probable decay emissions and energies are provided for ^{211}At, ^{210}At, and pertinent decay products (National Nuclear Data Center 2016). Decay modes with negligible yields are disregarded.

Radionuclide	**Emission**	**Energy (MeV)**	**Yield (Bq^{-1} s^{-1})**
^{211}At	α	5.870	4.18×10^{-1}
^{211}Po	α	7.450	9.89×10^{-1}
^{211}Po	α	6.892	5.46×10^{-3}
^{211}Po	α	6.658	5.37×10^{-3}
^{210}At	α	5.1 – 5.5	Less Than 10^{-3}
^{210}Po	α	5.304	1.0
Radionuclide	**Emission**	**Energy (keV)**	**Yield (Bq^{-1} s^{-1})**
^{211}At	γ	687.0	2.61×10^{-3}
^{211}Po	γ	569.7	5.35×10^{-3}
^{211}Po	γ	897.8	5.51×10^{-3}
^{211}At	$K_{\alpha 1}$	79.29	2.11×10^{-1}
^{211}At	$K_{\alpha 2}$	76.86	1.27×10^{-1}
^{207}Bi	$K_{\alpha 1}$	74.97	3.65×10^{-1}
^{207}Bi	$K_{\alpha 2}$	72.80	2.17×10^{-1}
^{211}Po	Various x-rays	74 – 85	Less Than 10^{-4}
^{210}At	γ	245.3	7.95×10^{-1}
^{210}At	γ	1181.4	9.93×10^{-1}
^{210}At	γ	1436.7	2.90×10^{-1}
^{210}At	γ	1483.4	4.65×10^{-1}
^{210}At	γ	1599.5	1.34×10^{-1}

In addition to the useful emissions, which will be discussed further under biological effects, ^{211}At has interesting and useful chemical properties. As a halogen, astatine functions as a homolog to iodine. Radioactive iodine isotopes, including ^{123}I, ^{124}I, ^{125}I, and ^{131}I, are widely used in diagnostic imaging via SPECT and PET, in therapy as sodium or potassium ^{131}I, and a wide variety of investigational and nuclear medicine techniques utilizing radiolabeled compounds. Free astatine accumulates in thyroid and stomach, similarly to iodine (Lyckesvard et al. 2014, Watanabe et al. 2016). The common use of radioiodine and these similarities make it a good candidate as a homolog for investigating astatine behavior both chemically and biologically. Despite the similarities, there are several significant differences (Appelman 1960, Aaij et al. 1975).

In general, astatine is less tightly bound that iodine in similar compounds, due to the size of the atom. This leads to the stability of carbon-halogen bonds to be weaker for astatine than corresponding iodine compounds (Wunderlich et al. 1989, Talanov et al. 2004, Ogawa et al. 2015). There are several consequences. First, more stable bonding structures may need to be used *in vivo* to prevent premature dissociation of the astatine and the targeting moiety. This premature dissolution requires the use of more complex chelating agents and transport molecules than are commonly used with iodine, such as tin based trimethylstannyl-benzamide immunoconjugates (Anaheim et al. 2015a, 2015b), tin based precursors to octreotide labels (Vaidyanathan et al. 2006, 2007b), rhodium based complexes (Rajerison et al. 2014), succinimidyl-astatobenzoate (Hadley et al. 1991) and other complex molecules (Friedman et al. 1977, Pruszynski 2015). In addition, astatine is

more easily volatilized than iodine, which, when coupled with its lower chemical stability, makes inhalation a concern during radiochemistry procedures.

Moreover, changes in the oxidation state of astatine in solution occur over time. It is generally believed that these changes are due to the formation of oxidative species by self-irradiation over time (Pozzi and Zalutsky, 2007). The various ionic states of astatine found in water or common elution media add to the difficulty in labeling and other processing. Especially during distillation, it is important to avoid the At(0) state, as it is easily absorbed on glass, quartz, or metal surfaces when acidity is introduced. Citrate buffer is commonly used in elution mixtures to help prevent this tendency. There is some argument in the literature regarding the existence of this state versus di-astatine (At_2) molecules. (Zona et al. 2008). Table 3 shows the known or expected ionic states of astatine (Appelman 1960, Zona et al. 2008). Guerard et al. provide an extensive review of the chemical properties of astatine in both inorganic and organic applications (Guerard et al. 2013).

Table 3. Common ionic states of astatine are presented with a description of each (Appelman 1960, Zona et al 2008, Guerard et al. 2013).

Ionic State	Description
At(-I)	Astatide, anionic form of At^-
At(0)	Neutral astatine, or di-astatine as found in At_2
At(I)	As found in the ipoastatite anion, $At(I)O^-$
At(III)	As found in astatite, $At(III)O_2^-$
At(V)	As found in the astatate anion, $At(V)O_3^-$

2.1.2 Radiobiological Effects

The biological effects of the emissions from ^{211}At are fundamental to its use as a therapeutic agent. Radiobiology and radiation effectiveness require an understanding of energy deposition and transfer mechanisms, linear energy transfer (LET), cellular response to radiation damage and radiations of different types, and other considerations.

At a microscopic level, heavy charged particles, such as alpha particles, interact in a wholly different manner than lighter ions, such as electrons or beta particles. While both particle types deposit energy directly through electronic interaction, the higher mass of alpha particles results in a relatively straight track with a high density of ionization surrounding the track. In comparison, beta-particles produce a widely divergent track with low density of ionizations. In addition, alpha particles are generally produced with kinetic energies on the order of 5-20 times larger than beta particles, resulting in a higher total number of ionizations. The total number of ionizations, coupled with the frequency with which they occur, play an integral part in the transfer of energy per unit path length as well as the probability of creating substantial damage.

The concept of the density of ionizations per unit path length is commonly given in terms of LET. Alpha particles have a higher LET by 2-3 orders of magnitude, resulting in much higher cytotoxicity and relative biological effectiveness (Chen et al. 2012, Hauck et al. 1998) The higher density of ionizations results in a higher concentration of double-strand breaks and other densely manifested lesions produced by alpha particles traversing the cell nucleus. The result is a much lessened cellular repair ability (Raju et al. 1991,

Dadachova 2010, Chen et al. 2012). Figure 3 shows the surviving cell fractions as a function of absorbed dose for various radiations (Bhakta 2011). The relative biological effectiveness of alpha emitters has been shown to be significantly greater than x-rays in all cell cycle stages (Claesson et al. 2011). Double strand breaks induced by ^{211}At have been shown to cause a skewed distribution in DNA fragment size, as compared to gamma irradiation and associated random fragment size distribution (Danielsson et al. 2013). It is not known whether this is one of the contributing factors for increasing RBE of alpha particles. (Claesson et al. 2007).

While assessing cell survival fractions as a function of absorbed dose has been the traditional method for assessing relative biological effects, it is more useful to consider other methods. The stochastic patterns of energy distribution along alpha tracks can lead to a wide variation of cell killing per unit absorbed dose. Attempting to describe these effects has led to the more useful measurement of the probability of creating lethal damage per particle transversal of the cell. Other models for assessing alpha-induced cellular damage include tumor control probability models and microdosimetric techniques (Roeske and Stinchcomb 1996, Roeske and Stinchcomb 1999, Roeske and Stinchcomb 2000, Unak 2003, Sgorous et al. 2010). These models are useful for determining effects in treating single cells and small tumor clusters.

The average number of particle transversal to result in a certain survival fraction is very dependent upon source distribution and concentration within the cells, cell cycle phase, and cellular geometry (Sgouros et al. 2010). To illustrate the role of geometry, Palm et al. noticed a large effect when studying ^{211}At effectiveness. When cell surface bound

^{211}At decayed to ^{211}Po, the polonium detached and diffused away from the receptor site prior to decay ($T_{1/2}$ = 0.516 s). The resulting change in solid angle reduced the effectiveness when compared to cell surface located decays by a factor of two (Palm et al. 2004). In other studies, alpha particle track autoradiography has been used to define *in vivo* cellular and intracellular distribution of ^{211}At radioactivity (Brown et al. 1992, Brown et al. 1994).

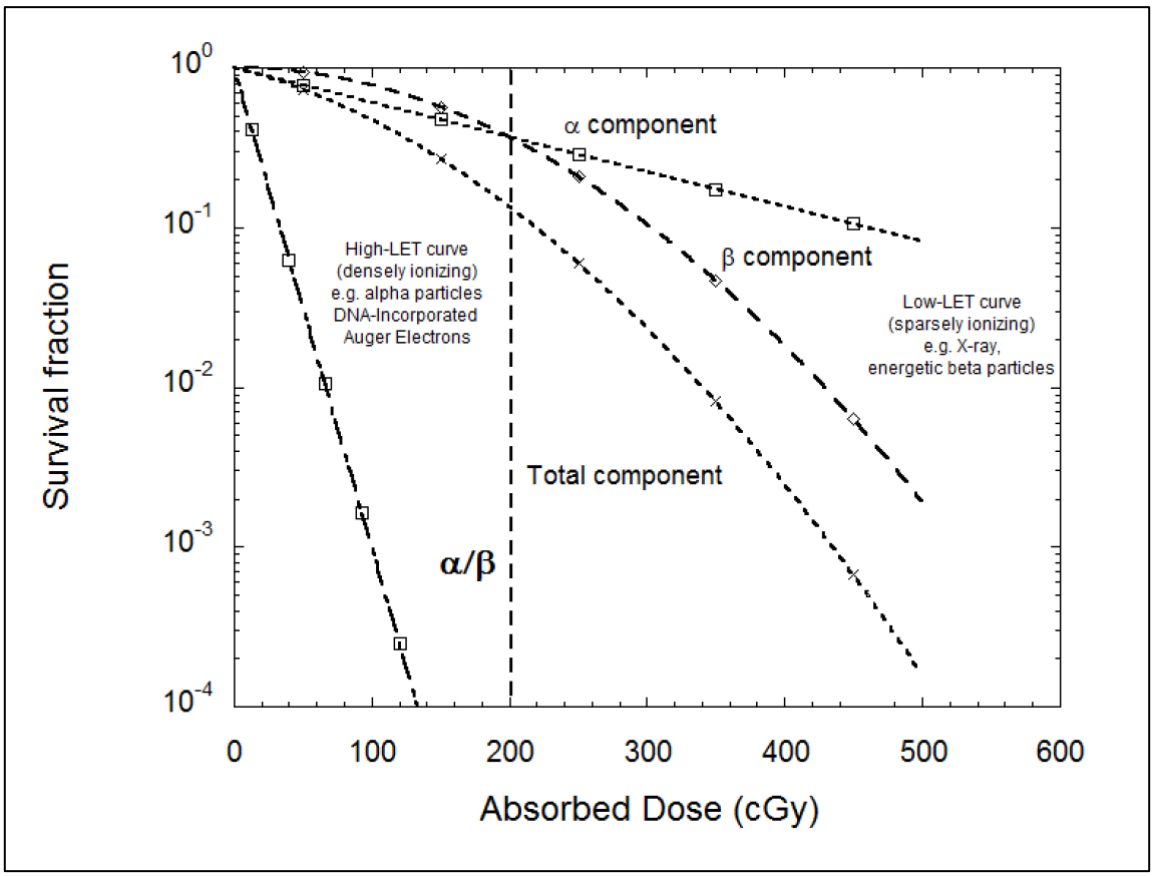

Figure 3. A comparison of radiobiological characteristics of various radiations as a function of absorbed dose, showing the relatively superior effectiveness of high LET radiation, such as alpha particles. Reprinted from Bhakta 2011.

An average of 1.5-3 transversals per cell nucleus is required to reduce survival to 37% (D_0), although the observed range of cellular traversals to achieve this number of nuclear traversals is anywhere from 1-20 per cell (Raju et al. 1991, Langen 2015, Rudqvist 2015). From these measurements, the mean free path between lethal events, λ, is derived, with an equally wide range of values, from 1.5-64.4 μm (Sgouros et al. 2010). Targeting methods that introduce astatine into the nucleus are even more effective. Astatine-211 labeled thymidine analogs in V79 lung fibroblasts in Chinese hamsters show better than ten times as many DSBs than similar ^{125}I labeled compounds. It is thought that this extreme radiotoxicity is related to the destruction of the genome. (Walicka et al. 1998).

In addition to studies on the effectiveness of ^{211}At, there has been some concern of toxicity related to the long-term effects of the daughter radionuclide ^{207}Bi. However, due to the long half-life (31.55 y) and smaller branching ratio (0.418), it is expected that long-term deposition in the bone, kidneys, and liver will be negligible (Guerard et al. 2013). Further studies into this issue and long-term radiotoxicity will be required when moving forward with FDA approvals.

2.1.3 Production Mechanisms

Nuclear reactions involving energetic charged particles are governed, to a large extent, by the kinetic energy of the incident particle and the composition of the target medium. At low incident energies, coulombic repulsion and energetic effects limit nuclear

interactions, resulting in scattering. As incident kinetic energy increased, it becomes possible for the charged particle to overcome this coulomb barrier. In many cases, a smaller energy than what is suggested by the coulomb barrier is permissible due to quantum tunneling (IAEA 2009a). Interactions of interest, such as the production of ^{211}At, are inherently endothermic by nature. Thus, the incident particle must also have sufficient energy to overcome this mass and binding energy difference, known as the Q-value. Excitation functions, or energy-dependent cross-sections, have been experimentally determined for many particles and energies incident on a variety of targets (Lambrecht and Mirzadeh 1985, IAEA 2009a, IAEA 2009b). These experimental results, as well as computational estimations from codes such as TALYS, have been compiled in a freely available database by the Organisation for Economic Cooperation and Development (OECD) and the Nuclear Energy Agency (NEA) (Koning 2008, JANIS 2016).

Astatine-211 is primarily produced via the ^{209}Bi(α, 2n)^{211}At reaction. While other reaction mechanisms are available, such as ^{209}Bi(^{7}Li, 5n)^{211}Rn$\rightarrow$ ^{211}At and ^{234}Th(p, cx)^{211}Rn$\rightarrow$^{211}At, these are not commonly used due to low yields and/or low availability of machines capable of using these methods (Maeda et al. 2015). The common helium on bismuth production method has become the most widely studied, due to the availability of machines capable of producing this reaction, ease and cost of obtaining materials, and control of contaminants.

2.2 Cyclotron Production of Astatine-211

The clear majority of ^{211}At is produced by the (α, 2n) reaction. This necessitates the availability of 20-28 MeV alpha particles at fluence rates of a large enough magnitude to produce useful quantities of the radionuclide (Henriksen et al. 2001). Practically speaking, this requires cyclotrons dedicated to the acceleration of alpha beams. The large number of biomedical cyclotron facilities in use have machines designed for proton and deuteron beams, optimized to produce positron-emitting radionuclides (IAEA 2009a). While there are dedicated biomedical cyclotrons available of newer manufacture capable of accelerating alpha particles, for example, the IBA Cyclone series, they have not yet been widely commissioned (Zalutsky and Pruszynski 2011). These cyclotrons are the most desirable for their high current capability when compared to large research cyclotrons intended for physics research. Large cyclotrons are optimised for high currents for heavier particles at higher energies, with a correspondingly low current available at the comparatively low energies necessary for ^{211}At production, as can bee seen from Eq. 1:

$$Q = kE^{v} \tag{1}$$

where Q is the beam intensity in μA_p, k is a machine-dependent constant, v is a machine-dependent constant (typically $v \approx 1.5$) and E is the particle energy in MeV (Kim et al. 2014). A similar equation, given maximum energy as a function of bending factor, K, is shown as:

$$E = KzM^{-1} \quad (2)$$

where E is the particle energy in MeV, K is the bending factor, z is the electric charge of the accelerated ion in Coulombs, and M is the mass of the accelerated ion in amu. Some smaller research cyclotrons have been adapted to radionuclide production use. For example, a Scanditronix MC-50 adapted to this purpose can produce alpha particles with energies of 27 MeV and beam intensities of up to 70 μA_e (Balkin et al. 2013). These are impressive yields, capable of producing activities greater than 19 mCi of ^{211}At in 45 minute at EOB.

The Texas A&M Cyclotron Institute is a large interdisciplinary research facility housing two cyclotrons. The K-150 88" cyclotron, a near copy of the unit at Lawrence Berkeley National Laboratory, was commissioned in 1967 and utilizes a new electron-cyclotron-resonance (ECR) ion source to produce positive ions. Using alpha particles in the +2 charge state, the expected maximum particle energy and intensity are 45 MeV u^{-1}, and 10 μA_p. This is assuming a bending factor of K = 140, and a maximum transmission of 25%. Using Eq. 1, the estimated maximum beam current at 28 MeV (7 MeV u^{-1}) is approximately 5 μA_e, considering machine variations. The K-500 cyclotron was constructed in the early 1980's and is primarily geared towards high energy physics experiments and production of rare beams. It utilizes an ECR source, but is not capable of producing large currents in the energy range necessary for direct bombardment of bismuth for astatine production (Laune et al 1983a, Laune et al. 1983b, Youngblood 1990,

Youngblood 1991). A schematic drawing of the Texas A&M University Cyclotron Institute is given in Fig. 4. The beamline with the astatine production target location is notated.

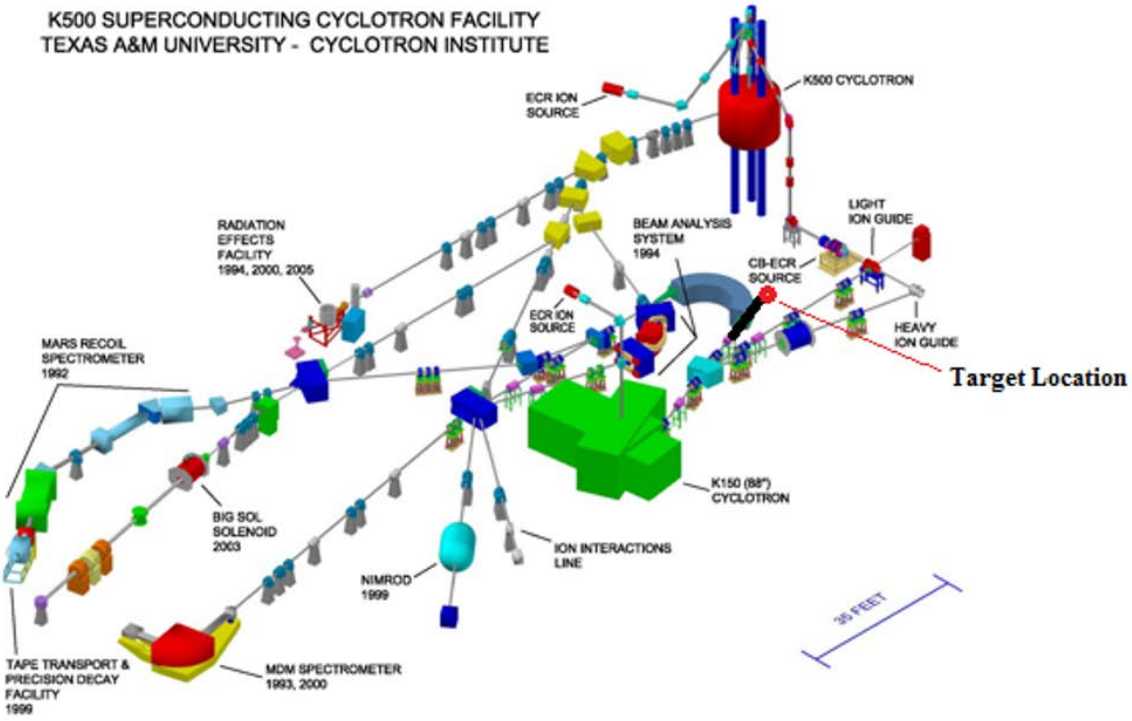

Figure 4. The Texas A&M University Cyclotron Institute facility layout. The astatine production target location is next to the large bending magnet near the K-150 cyclotron. Reprinted from Bhakta 2011.

Preliminary experiments and proof-of-concept irradiations were carried out using the K-500 cyclotron, as the K-150 was undergoing extensive restorative maintenance over a time frame of several years. Briefly, 80 MeV (20 MeV u^{-1}) helium atoms were extracted

and bombarded a set of aluminum and copper degradation foils before impinging on a bismuth target. These degradation foil packs were designed to reduce the beam energy to nominally 25.5 MeV (6.38 MeV u^{-1}) and 27.8 MeV (6.95 MeV u^{-1}), while allowing for higher currents than would have been available at endpoint energies. Still, currents on target were in the range of 0.10-0.15 μA_p. These experiments showed nominal yields on the order of those found in the literature and gave valuable experience in target design and materials handling (Martin et al. 2014). This was applied to the target development and utilization of the K-150 described in this research.

2.2.1 Targetry

Astatine-211 is produced by the (α, 2n) reaction on natural bismuth. In most cases, targetry consists of bismuth melted or plated onto an aluminum target backing plate (Birattari et al. 2004). Both internal and external targets have been used to varying degrees of success (Martin et al. 2014). Published yields and target descriptions comparing previous results are given in Table 4. As can be seen from these data, incident beam energy and target thicknesses are carefully controlled. These constraints are imposed by the excitation functions and particle interactions, as described in the following subsection.

Table 4. Reported yields of ^{211}At are shown from various sources at end of bombardment. Sources marked with an asterisk indicated an internal target was used.

Source	Incident Energy (MeV)	Target Thickness (μm)	^{211}At Yield EOB (MBq μA_p^{-1} h^{-1})
Martin et al. 2014	27.8	500	36.0
Martin et al. 2014	25.5	500	12.4
Wunderlich et al. 1986	28	20	4
Lambrecht & Mirzadeh 1985	28	100	5.3-10.4
Aaij et al. 1975	33	500	7.4-14.8
Rosch et al. 1985	28	500	8.56
Larsen et al. 1993	28	250	8-12
Hadley et al. 1991	28	500-800	10-12
Larsen et al. 1995	28	100	15.2-15.6
Hamwi et al. 1991	28	30	27.7
Groppi et al. 2005	28.8	-	31.9
Lebeda et al. 2005*	29.5	3-5	38
Larsen et al. 1996*	28	50	41
Schwarz et al. 1998*	28-29	30-80	37-41
Schwarz et al. 1998	27.3	1000	10.6
Alfarano et al. 2006	28	250	48

In general, the clear majority of targets designed to produce ^{211}At have consisted of bismuth attached to an aluminum backing plate. Bismuth is ideal in that natural bismuth (100% natural abundance) can be used without the added expense and complication of isotopic enrichment.

Sample excitation functions were shown in Fig. 2, and are presented below in Fig. 5. The (α, 2n) cross section becomes negligible below energies of 18-20 MeV. An upper threshold of 28.6 MeV (7.15 MeV u^{-1}) is set to eliminate production of the impurity ^{210}At/^{210}Po, generated by the (α, 3n) reaction. As can be seen, careful control of incident

energy and target thickness is required to maintain the desired reactions, while minimizing contamination from unwanted interactions and maintaining target integrity.

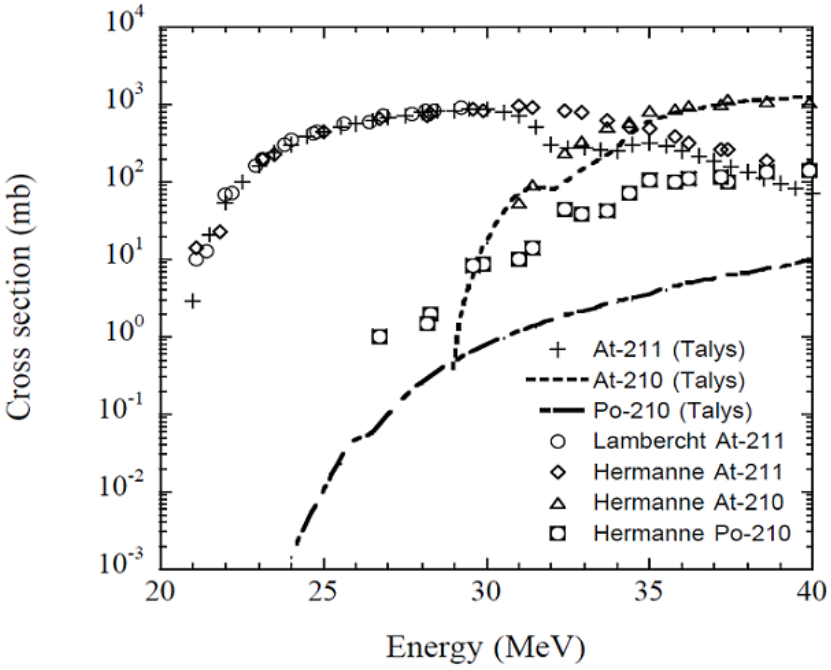

Figure 5. Excitation functions are shown for ^{210}At and ^{211}At production (Bhakta 2011).

The collision stopping power, dE/dX, or differential energy loss rate per distance, of a heavy ion interacting in matter, can be given by

$$\frac{dE}{dX} = 0.3071 \frac{z^2}{\beta^2} \frac{\rho Z}{A} \left[13.837 + \ln\left(\frac{\beta^2}{1-\beta^2} \right) - \beta^2 - \ln I \right] \tag{3}$$

where dE/dX is the collision stopping power in MeV cm^{-1}, ρ is the target material density in g cm^{-3}, Z is the target material atomic number, A is the target material atomic mass in amu, z is the charge of the projectile, I is the mean excitation potential, and β is the relativistic projectile velocity, which is in turn given by

$$\beta = \left[1 - \left(\frac{1}{\left(E \big/ M_0 c^2\right) + 1}\right)^2\right]^{1/2} \tag{4}$$

where M_0c^2 is the rest mass of the projectile. The mean excitation potential, I, is experimentally determined and depends solely upon the target material. Radiative stopping power is disregarded, as it is negligible in the energy range of interest for heavy charged particles (Attix 2004).

Using Eqs. (3) and (4), the continuous slowing down approximation range can be estimated using

$$R = \int_{E_f}^{E_i} \left(\frac{dE}{dX}\right)^{-1} dE \tag{5}$$

where E_i is the initial projectile energy in MeV, E_f is the final projectile energy in MeV, and R is the range, in cm. The continuous slowing down approximation range is only

approximate, as it does not take into account energy straggling and range straggling (Attix 2004).

The above equations can be used to determine the range of 28 MeV alpha particles incident upon natural bismuth. Taken to an endpoint of no residual kinetic energy ($E_f \approx 0$ MeV), the range is approximately 180-200 μm. However, taken to an endpoint of $Ef = 19$ MeV, the range is approximately 30-50 μm. These estimations are consistent with more rigorous computation using the code SRIM (Stopping and Range of Ions in Matter), as well as previously reported results (Lambrecht and Mirzadeh 1985, Ziegler et al. 2010). An example of ten thousand simulated 28 MeV alpha particles incident on bismuth is shown in Fig. 6. This is a graphical output from SRIM, showing straggling and lateral projections, which showcase the stochastic nature of radiation transport. Median range was computed to be 202 μm, with a straggling factor of 6.5 μm, and an average lateral dispersion of approximately 10 μm.

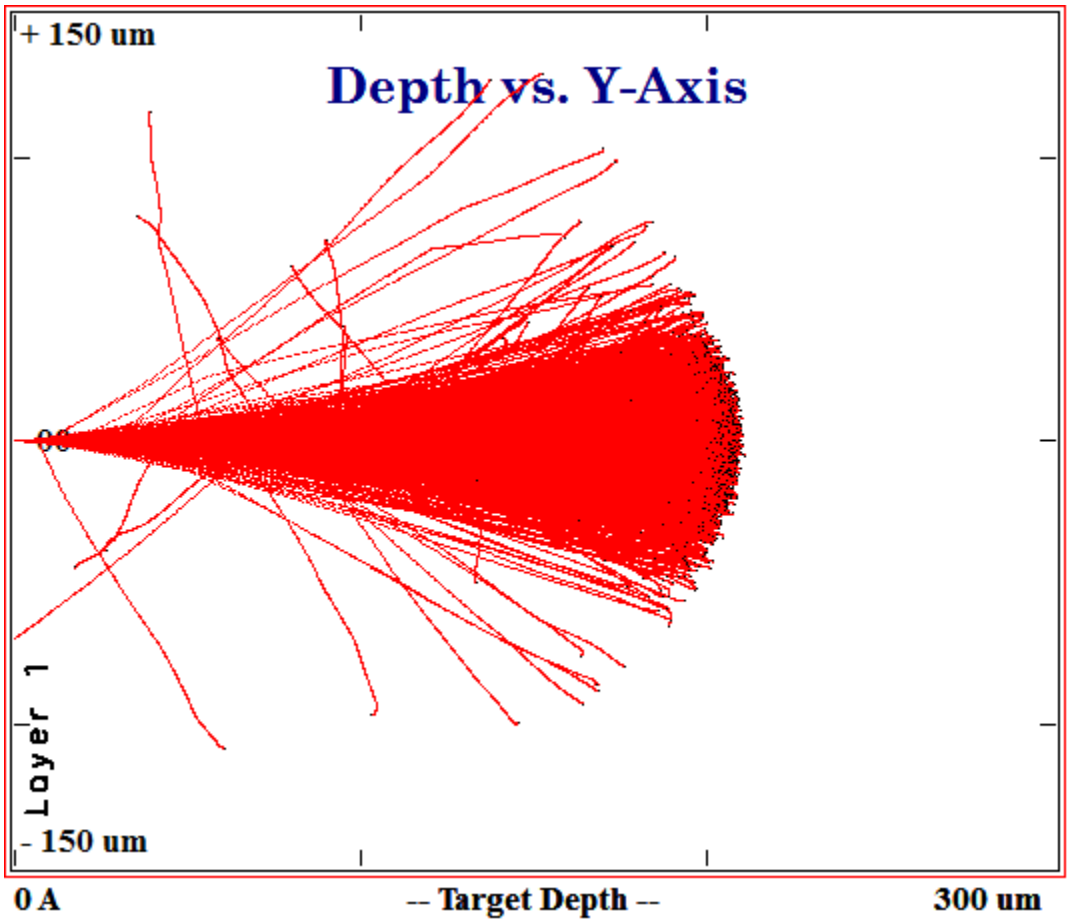

Figure 6. Particle track depth (ranges) is shown for ten thousand 28 MeV alpha particles incident on bismuth.

Projectile range as a function of energy has considerable impact on target design, given the energy deposition characteristics of heavy charged particles. These particles deposit energy with the typical Bragg peak, where the vast majority of the particle energy is deposited near the end of the particle track. For example, using 28 MeV alpha particles in bismuth, 14 MeV is deposited in approximately the last 65 μm, and 7 MeV in the last 25 μm. To illustrate this, stopping power for 30 MeV alpha particles incident on bismuth are shown versus energy in Fig. 7, and versus depth in Fig. 8. Data for these plots were

generated using SRIM. Because of this Bragg distribution, there is a decidedly non-uniform distribution of heat flux in the target volume.

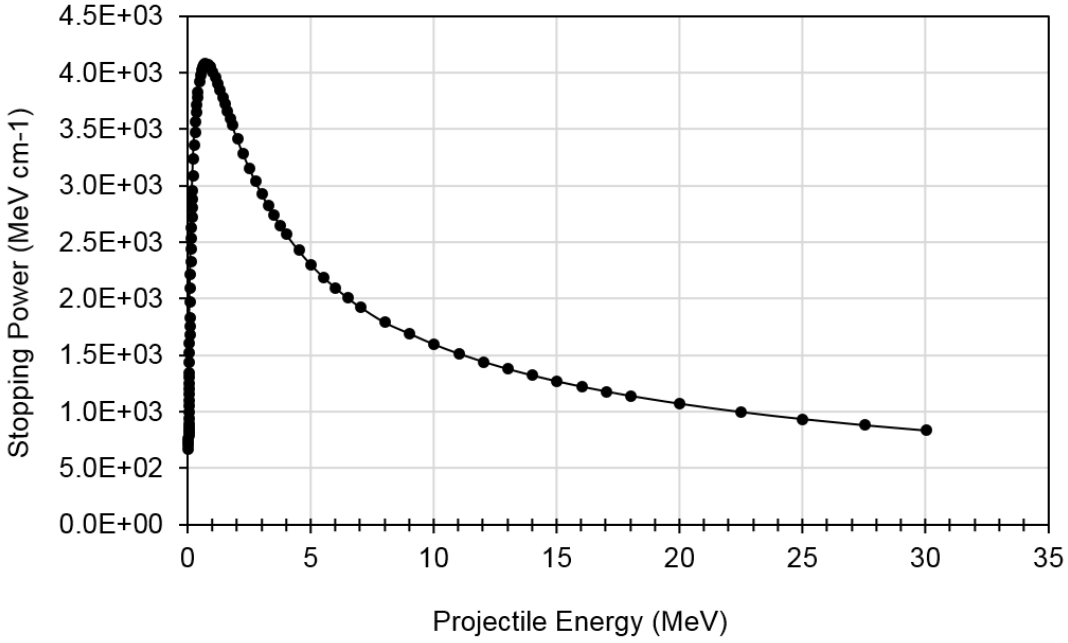

Figure 7. Stopping power for alpha particles incident on bismuth is shown as a function of energy.

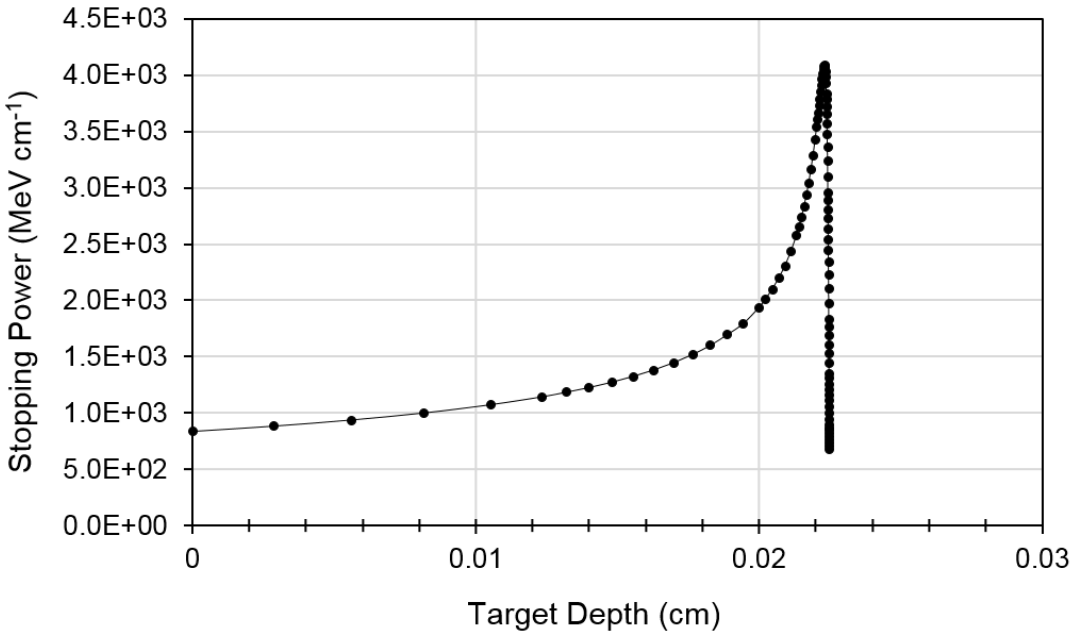

Figure 8. Stopping power for 30 MeV alpha particles is shown as a function depth in bismuth.

Some of the biggest obstacles in efficient target design for ^{211}At production are thermal considerations. The low melting point (272 °C) and the low thermal conductivity (7.86 W m^{-1} K^{-1}) of metallic bismuth limit the amount of heat flux that can be applied to a target without negative consequences, such as melting and loss of designed target geometry by deformation. For example, as ductile metals approach the melting point, the force exerted by their own mass can cause bending and deformation, affecting target geometry. Three main factors influence the thermal qualities of a target: characteristics of the incident heat flux, physical characteristics of the target, and heat removal qualities.

Incident heat flux is primarily driven by the incident beam characteristics. Focal spot size, beam energy, and beam intensity are the main considerations. As seen in Fig. 7, the fundamental physics involved in heavy charged particle transport results in non-uniform heat deposition as a function of depth in the target. Due to the physics involved both with cyclotron motion and beam steering, energy and intensity distributions are non-uniform in lateral and radial directions. Changes in focal spot size and shape can greatly affect these distributions, and localized “hot spots” are possible. When possible, after beam tuning, radiographic film is exposed in the location of the target holder to analyze these beam characteristics. However, in these experiments, the lack of a dedicated vacuum isolation valve made this impractical. It is imperative that all target regions remain below 336.8 °C, the boiling point of astatine, with a considerable safety factor. In practical terms, preventing liquefaction of the bismuth target will both preserve target geometry and provide adequate margin against localized hot spots which could cause evaporation of produced astatine (Martin et al. 2014).

One method of controlling thermal characteristics while maintaining higher current is to use an internal target. Several groups have experimented with this method (Larsen et al. 1996, Schwarz et al. 1998, Lebeda et al. 2005). The creation of a curved or angled target placed in the beam line within the cyclotron at a grazing angle allows the beam to spread out over a large area, thereby reducing incident heat flux. These targets have generally shown higher yields, at shorter run times, which makes them attractive for routine production. However, there are several possible drawbacks. First, any excessive or localized heating may cause contamination of the cyclotron. This is of minimal concern

during operation, as any off-gassed material will likely be captured in the cryopumps, and cyclotron internal components are already highly radioactive. However, during maintenance, and especially ion source replacement, effluent concentrations of astatine can become high (Hull and Roberson 2011). More importantly, maintaining vacuum with an easily removable target system can pose some difficulties. Reusable targets, made to the high tolerances required, are prone to damage during the distillation process. Disposable targets must be made to fairly high tolerance standards, which increases their cost. The end benefit of increased beam on target can negate these downsides; for example, beam currents of approximately 65 μA_e have been reported, as opposed to 15 μA_e for external targets (Zalutsky and Pruszynski 2011). Graphite leading edge and trailing edge monitors may be used on internal targets to provide some indication of beam distribution. (Larsen et al. 1996, Zalutsky and Pruszynski 2011).

Other groups have experimented with vertical beam irradiation of bismuth shot contained within a sealed aluminum capsule. This method reduces temperature considerations, as any volatilized astatine due to the melting of bismuth is contained within the capsule. Volatilized astatine is transferred back to a liquid or solid state following irradiation, but prior to dry distillation (Nagatsu et al. 2014).

Utilizing the stopping power equation and the nonlinear energy deposition with depth brings to light one of the most attractive methods for reducing heat deposition in the bismuth target. By utilizing an extremely thin layer of target material, a maximum of only 8-9 MeV may be deposited per particle. For example, calculations using SRIM showed that an approximately 30 μm layer of bismuth would reduce incident alpha energy from

28 MeV to 19.5 MeV. This energy range encompasses the useful cross section range of the (α, 2n) reaction, and allows the majority of the beam energy to be deposited in a more robust backing material, such as aluminum. The main difficulty lies in target manufacturing. Target foils of bismuth are not readily available in thicknesses of less than 150 μm. Machining an aluminum target backing plate with a slot to press or melt bismuth into is a standard practice; however, 30 μm corresponds to approximately 0.0012", which is close to the tolerance limit of most standard milling machines. Additionally, melting or pressing bismuth target material results in non-uniform target thickness, especially on the front face of the target. These complications leave electroplating or vapor deposition, which have not been thoroughly investigated, in part due to complexity and difficulty in setting up a system for small scale production (Larsen et al. 1996, Lindegren et al. 2001, Yordanov et al. 2004). The problem of target thickness is exacerbated when the target is angled. For example, a 30 μm target angled at 80° normal to the incident beam gives a perceived thickness of 173 μm. To create a 30 μm path length under these conditions would require a thickness of only 5.2 μm.

Preliminary ^{211}At production experiments at the Texas A&M University Cyclotron Institute utilized a 500 μm thick bismuth target normal to the incident beam, and did not utilize active cooling. However, beam intensities on-target were low, in the range of 0.096-0.163 μA_p, with an approximate incident heat flux of 13 W cm^{-2} (Martin et al. 2014). Copper and aluminum degradation foils, with high thermal conductivities (401 W m^{-1} K^{-1} and 237 W m^{-1} K^{-1}, respectively), coupled with the substantial aluminum target body, aided in heat dissipation.

Routine production experiments utilizing the K-150 cyclotron have an expected maximum incident heat flux of 375 W cm^{-2}, assuming a circular beam diameter of 10 mm and a uniformly distributed beam current of 5 μA_p on a thick target. Therefore, more robust cooling methods are required. Several solutions have been incorporated into the routine production target. First, the target has been oriented at an angle of 80° normal to the incident beam. This orientation results in a reduction of incident heat flux to approximately 65 W cm^{-2}. A maximum of 80 W cm^{-2} is designed for, to accommodate the Gaussian beam radial distribution. Second, cold deionized water, cooled to 4 °C, with an approximate flow rate of 1.5 L min^{-1}, may be flowed through a channel milled into the rear of the target holder. Third, pyramidal indentations have been implemented into the aluminum target backing. This increases the contact surface area between the bismuth and the aluminum, increasing conductive heat transfer, while also improving mechanical adhesion between the dissimilar materials. Fourth, silicon dioxide thermal grease is available for layering between the aluminum target backing and the target holder apparatus. This may increase thermal conductivity as well, by removing air gaps between the surfaces. However, this may prove problematic during dry distillation. The grease must either be removed satisfactorily by chemical means, or the bismuth-astatine matrix must be mechanically separated from the target backing while preventing contamination by this thermal grease. Finally, a quick-change clamping mechanism was developed to attach the target backing plate to the target holder. This was designed to provide a rapid release of the target, as well as provide increased pressure between the holder and backing plate to increase thermal conductivity.

A picture of the production target is provided in Fig. 9. In this figure, the alpha beam is incident from the right side and passes through a rectangular collimator slit, visible in the picture. The thermocouple for measuring target temperature is seen, as is the fitting for coolant water. Not present is the clamping device. Also, note the Teflon insulators on the two rods to which the collimator is mounted. This electrical isolation allows for monitoring of the incident beam electrical current during irradiation.

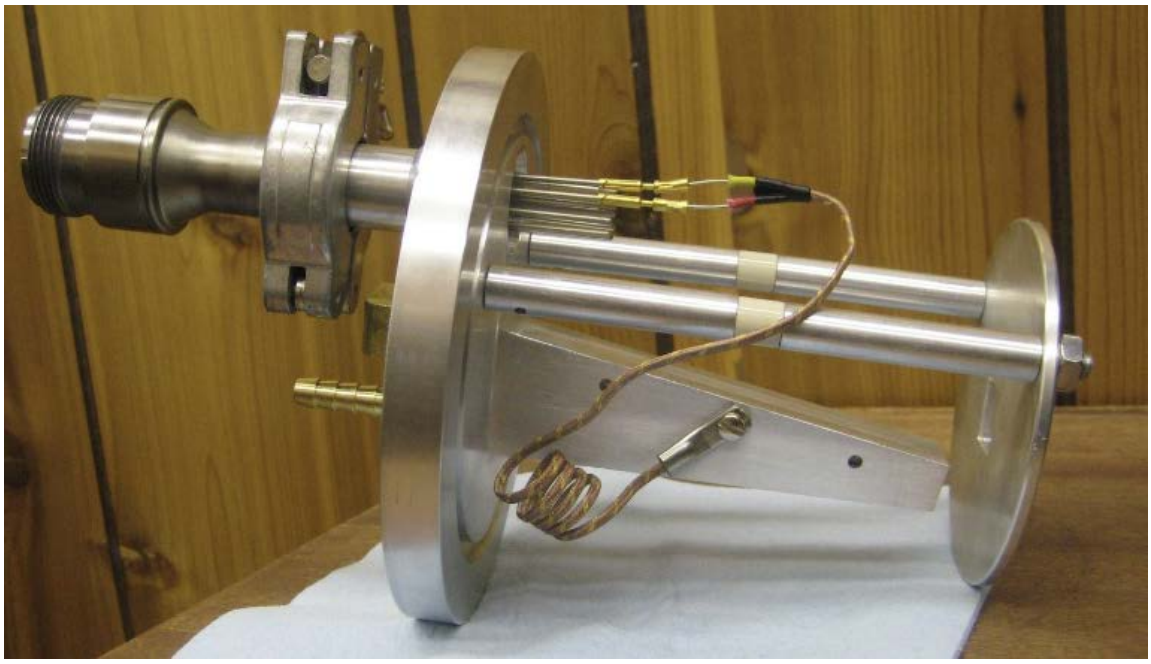

Figure 9. The production target holder is shown. Details of the apparatus are given in the text.

A depiction of the bismuth target and aluminum target backing is provided in Fig. 10. These show the original target backing, prior to incorporation of the pyramidal indentions. The aluminum backing plate measures 9.05 cm (3 9/16”) long by 2.06 cm

(13/16”) wide, by 0.32 cm thick (1/8”). Into this plate, a slot is milled that measures 1.27 cm (1/2”) wide, and 7.62 cm (3”) from end to end (or 2.5” center to center). This slot measures approximately 0.5 mm (0.02”) deep. A dimensioned drawing of the target is provided in Fig. 11. The result is a thick target, with a bismuth layer of approximately 500 μm. A target angle of 80° normal to the incident beam resulted in a path length of better than 2.8 mm. Pure bismuth beads (99.999%, Sigma-Aldrich) were melted and deposited into the target backing plate. During cooling, excess bismuth was scraped from the surface, while simultaneously pressing the bismuth into the slot. This process results in some non-uniformities in target volume (voids, unevenness, etc.), especially on the target surface, as seen in the figure. These variations led concerns of thermal conductivity through the target/target backing interface. Pyramidal indentations in the target backing slot were implemented to assist in this.

Figure 10. The basic target backing is shown, bare, and filled with bismuth.

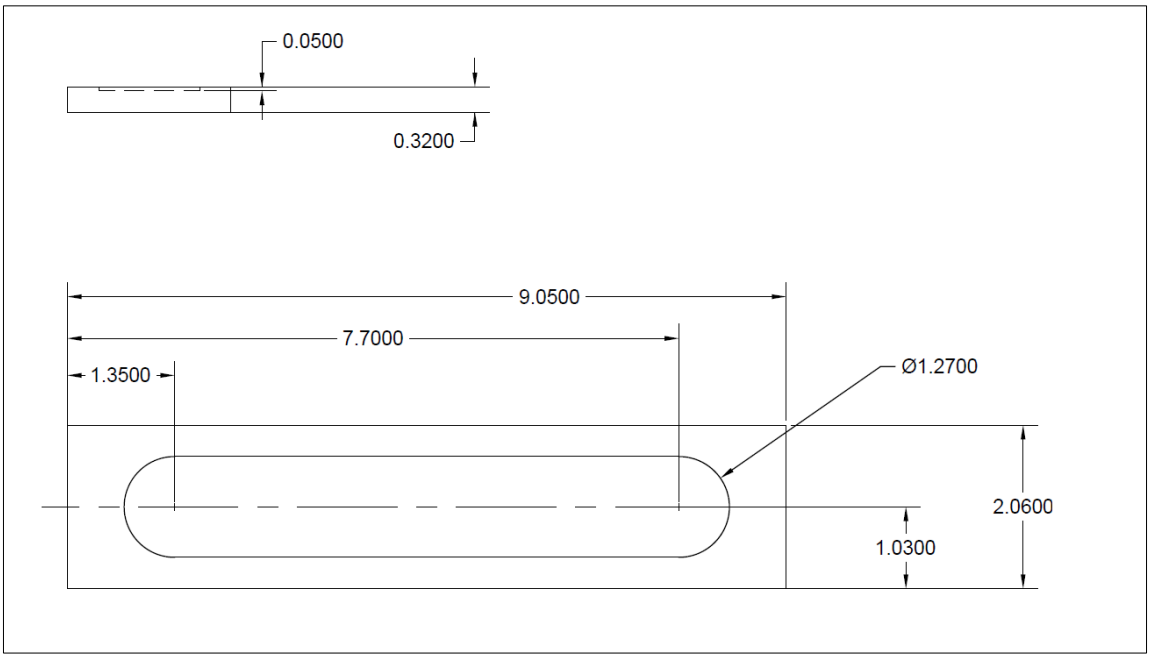

Figure 11. A dimensioned drawing of the target is shown. Dimensions are in cm.

2.2.2 Thermal Analysis

To determine approximate target thermal characteristics, a simplified thermal analysis was necessary. A more rigorous thermal analysis, utilizing computational methods, and with more complete characterization of beam parameters, will be necessary for future production of commercial targets. A preliminary calculation using a one-dimensional heat transfer model is provided below (IAEA 2009b, Williamson 2010).

Fourier's Law can be stated in terms of separable first order partial differential equations. Taken in a single dimension, this can be stated as

$$j_x = -k \frac{\partial T}{\partial x} \tag{6}$$

where j_x is the heat flux (W cm^{-2}) in the x direction, k is the thermal conductivity in W cm^{-1} K^{-1}, and $\partial T/\partial$x is the partial differential temperature in the x direction. Here, the assumptions are made that the x direction is normal to the target surface, heat transfer in the orthogonal directions is negligible, and that thermal conductivity remains constant as a function of temperature. While it is possible to calculate the heat deposition with depth utilizing the stopping power equation, some further simplifying assumptions can be made. All energy deposition is assumed to occur at the Bragg peak, or at a beam depth of approximately 200 μm. Using the target geometry, this results in a uniform plane 35 μm from the front surface of the target. A uniformly distributed, circular beam of 10 mm diameter is assumed which results in an ovoid projection measuring 10 mm in width by 57.6 mm long. Since it is assumed there is no heat transfer in orthogonal directions, and heat flux is normalized per unit area, beam size can be neglected. Finally, as the front target face is exposed to high vacuum of approximately 5×10^{-6} torr, heat transfer through the front surface is negligible. Coupled with the very poor thermal conductivity of bismuth, and to simplify initial estimates under steady state conditions, a constant temperature throughout the bismuth layer was assumed. A pictorial description of the problem is provided in Fig. 12.

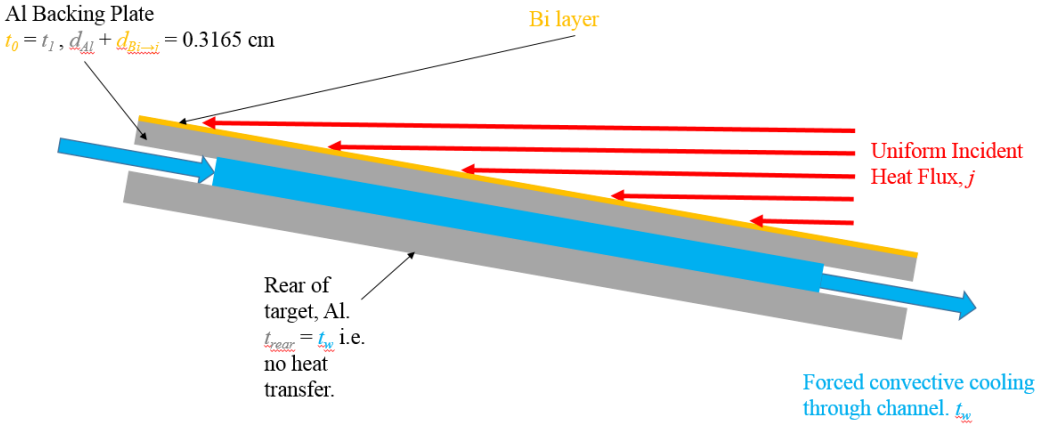

Figure 12. A pictorial description of the heat transfer problem is presented.

A coupled version of Eq. (6) is derived to describe conduction through the bismuth layer as well as the aluminum backing plate:

$$j_x = -k_{Al}\frac{(T_1 - T_2)}{d_{Al}} - k_{Bi}\frac{(T_0 - T_1)}{d_{Bi}} \tag{7}$$

where k_{Al} = 2.37 W cm^{-1} K^{-1} is the thermal conductivity of aluminum, d_{Al} = 0.27 cm is the thickness of the aluminum backing plate, k_{Bi} = 0.0786 W cm^{-1} K^{-1} is the thermal conductivity of metallic bismuth, d_{Bi} = 0.0465 cm is the thickness of the bismuth target

between the aluminum and the Brag peak, T_0 is the maximum temperature, T_1 is the temperature at the bismuth/aluminum interface, and T_2 is the temperature at the aluminum/water interface. Using the simplifications given above, the case where $T_0 = T_1$, which will allow a solution using convective heat transfer equations, was considered.

Considering one-dimensional heat transfer via forced convection, the heat flux removal is given by Eq. (8)

$$j_x = h\left(T_2 - T_w\right) \tag{8}$$

where h is the convective heat transfer coefficient in W cm^{-2} K^{-1}, and Tw is the bulk temperature of the water in the cooling channel. The convective heat transfer coefficient is highly dependent upon boundary layer, geometry, fluid properties, surface friction, and other contributing factors. Heat transfer also depends upon laminar or turbulent flow, and the ratio of convective heat transfer to conduction through the liquid. The Nusselt number (Nu) gives an indication of these properties, and is related to h by the equation

$$Nu = \frac{hD_h}{k_w} \tag{9}$$

where D_h = 0.423 cm is the characteristic length in cm, and k_w = 0.0058 W cm^{-1} K^{-1} is the thermal conductivity of water at 20 °C. For flow through a pipe or channel, the

characteristic length is equal to the hydraulic diameter, which for a rectangular cross section is given by

$$D_h = \frac{2ab}{a+b} \tag{10}$$

where a and b are the channel length and width, in cm. For relatively small differences between the bulk water temperature and the interface temperature, and smooth surfaces, the Nusselt number can be approximated by the Dittus-Boelter equation, given by

$$Nu = 0.023\,\mathrm{Re}^{0.8}\,\mathrm{Pr}^{0.4} \tag{11}$$

where Re is the Reynolds number and Pr is the Prandtl number. These dimensionless numbers define viscous and diffusivity effects. In constrained flow, the Reynolds number is given by

$$\mathrm{Re} = \frac{\rho_w V D_h}{\mu_w} \tag{12}$$

where ρ_w = 0.998 g cm^{-3} at 20 °C, V = 124.4 cm s^{-1} is the flow velocity, and μ_w = 0.0098 g cm^{-1} s^{-1} is the viscosity of water at 20 °C. V is obtained using the known volumetric flow rate (1.5 L min^{-1}) and the channel cross sectional area (0.201 cm^2). The result is a Reynolds number of approximately Re = 5358, which indicates flow is turbulent.

The Prandtl number is given by

$$\mathrm{Pr} = \frac{\mu_w C_{p,w}}{k_w} \tag{13}$$

where $C_{p,w}$ = 4.186 J g^{-1} K^{-1} is the specific heat capacity of water at 20 °C. Solving Eq. (13) gives a Prandtl number of Pr = 7.07. Substituting these values of Re and Pr, and utilizing Eqs. (9) and (11), solve for a convective heat transfer coefficient of h = 0.663 W cm^{-2} K^{-1}.

Using water at 4 °C, the interface temperature can be calculated. Using this information, various temperature distributions and incident heat fluxes can be tabulated from iterative solving to provide an estimate of maximum beam currents give the simplified cooling conditions and a maximum bismuth temperature of 272 °C. These data are presented in Table 5, and are only approximate due to the number of assumptions and simplifications made. This may be especially true of Eq. (11) due to the large difference in temperature between T_w and T_2. Using a conservative maximum temperature of 260 °C to account for non-uniformities, and to keep localized heating well below the melting point of bismuth, the target design should readily handle up to 8 μA_p of incident current.

Table 5. Temperature ranges are reported for various values of incident heat flux.

Heat Flux, j **(W cm^{-2})**	**Current, Q** **(μA_p)**	T_w **(°C)**	T_2 **(°C)**	T_0 **(°C)**
165.2	10.3	4	253.2	272
160.2	10.0	12	253.7	272
155.3	9.7	20	254.3	272
163.9	9.2	4	251.3	270
159.0	8.9	12	251.8	270
154.1	8.7	20	252.4	270
160.9	9.1	4	246.7	265
155.9	8.8	12	247.2	265
151.0	8.5	20	247.8	265
157.8	8.9	4	242.0	260
152.9	8.6	12	242.6	260
147.9	8.3	20	243.1	260

2.2.3 Theoretical Yield

The yield, or activity produced, of a cyclotron-produced radionuclide is an overall measure of the target efficiency. Yield is generally given in terms of activity produced per incident particle, for instance in units of MBq μA_p^{-1} h^{-1}, or similar. As production and decay are dynamic processes, the time of determination of yield must be stated, and is customarily taken as the end of bombardment (EOB). Processing and distillation yields are usually stated in terms decay corrected back to EOB.

Maximum yields depend upon target thickness, composition, and irradiation time. Calculations are made easily when considering a so called 'thick' target; that is, a target in which incident particles are expected to stop, based on Eq. (5). Theoretical thick target yields are also calculated for irradiations of a sufficiently long time that the saturation factor approaches unity. The saturation factor is given by

$$SF = \left(1 - e^{-\lambda t}\right) \tag{14}$$

where λ is the decay constant of the produced radionuclide ($\lambda = \ln(2)\ T_{1/2}^{-1}$), and t is the irradiation time. Thus, the saturation yield goes to a maximum as the saturation factor goes to unity. This limit is approachable as the ratio of irradiation time to half-life increases. For example, irradiating for a period equal to $t = 3.3\ T_{1/2}$ gives a saturation factor of greater than 90%. This can be achieved for short-lived radionuclides; however, extremely long irradiations become impractical for long-lived radionuclides.

The rate of radionuclide production is given by Eq. (15)

$$A(t) = \frac{dN(t)}{dt} = \lambda N(t) = 1 \times 10^{27}\, \Phi\left(1 - e^{-\lambda t}\right) \int_{E_i}^{E_f} \frac{\sigma(E)}{dE/dx}\, dE \qquad (15)$$

where N is the number of radioactive nuclei, Φ is the incident fluence rate in particles cm^{-2} s^{-1}, and $\sigma(E)$ is the energy-dependent interaction cross section in mb. Note the saturation factor imbedded in the equation. This equation makes uses of several simplifying assumptions, including a constant and uniformly spatially distributed particle fluence rate, negligible burn-up (or activation) of daughter products, negligible decrease in target nuclei, and no radioactive or daughter nuclei at t = 0 (Knoll 2000, Attix 2004). Incident fluence rate can be calculated using the incident beam current and beam diameter by

$$\Phi = 6.25 \times 10^{12}\, \frac{Q}{a} \qquad (16)$$

where Q is the beam current in μA_p, and a is the beam cross sectional area in cm^2. This assumes that the beam diameter is smaller or equal to the projected target surface area, as well as a uniformly distributed beam in both energy and space. Utilizing equations (15) and (16), along with tabulated cross section data, maximum thick target yields can be calculated as

$$Y(E) = n\int_{E_i}^{E_f} \frac{\sigma(E')}{-dE'/dx} dE' \quad (17)$$

where *Y(E)* is the energy-dependent thick target yield in MBq μA_p^{-1}, and *n* is the number of target nuclei (Lambrecht and Mirzadeh 1985, Basunia et al. 2007). This can easily be solved using discretized versions of the stopping power and cross sections through reasonably narrow binning through the target. Tabulated cross section data are provided in Table 6 (Lambrecht and Mirzadeh 1985, Hermanne et al. 2005). These data are plotted in Fig. (13), with a fitted polynomial curve.

Table 6. Cross sections for the ^{209}Bi (α, 2n) ^{211}At reaction are tabulated as a function of energy. Data without energy error are from Lambrecht and Mirzadeh.

E **(MeV)**	**Error**	***σ(E)*** **(mb)**	**Error**	***E*** **(MeV)**	**Error**	***σ(E)*** **(mb)**	**Error**
21.1	2.0	14.0	2.0	25.6	--	561.8	16.9
21.4	--	12.8	1.0	26.4	--	589.6	17.7
21.8	1.8	23.0	3.0	26.7	1.2	651.0	65.0
22.0	--	68.3	2.6	26.8	--	715.2	21.5
22.2	--	72.2	2.2	27.7	--	761.1	22.8
22.9	--	164.3	5.0	28.1	--	826.7	24.8
23.1	1.8	195.0	23.0	28.2	1.2	733.0	73.0
23.5	1.6	224.0	27.0	28.3	1.0	770.0	77.0
23.8	--	309.8	19.7	28.4	--	837.7	24.8
24.0	--	348.8	10.5	29.2	--	906.5	26.9
24.7	--	432.2	13.0	29.6	1.0	868.0	87.0
24.8	--	450.5	13.5	29.9	0.9	822.0	82.0
25.0	1.3	454.0	54.0				

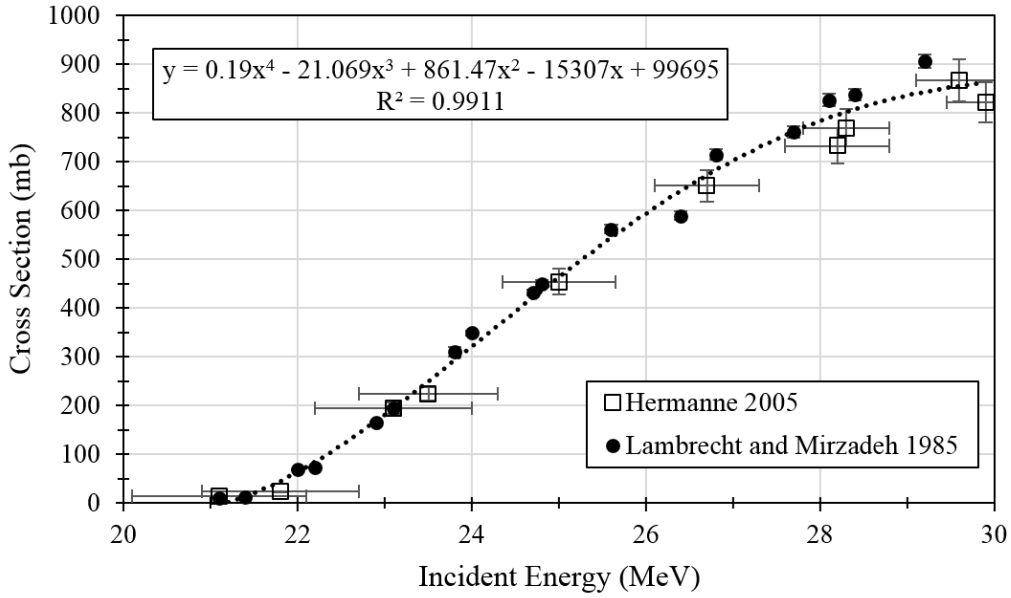

Figure 13. The fitted excitation function for the ^{209}Bi (α, 2n) ^{211}At reaction is shown.

Using stopping power and range data from SRIM (c.f. Fig. 7), second order polynomial equations were fitted to the data between 20 MeV and 30 MeV. In this range, stopping power ($R^2 = 0.9999$) and range ($R^2 = 1$) can be estimated by:

$$\frac{dE}{dx} = 0.7139E^2 - 59.338E + 1975.4 \tag{18}$$

$$R = 0.00001E^2 + 0.0004E - 0.0013 \tag{19}$$

where dE/dx is in MeV cm^{-1}, R is in cm, and E is in MeV. Using equations (17-19), the thick target saturated yield can be calculated for this target. The result is shown in Fig. 14, and compares favorably with published yields, as seen in Fig. 15 (Lambrecht and Mirzadeh 1985). The actual product yield may be calculated from radiation measurements. This is discussed further in section 2.4.

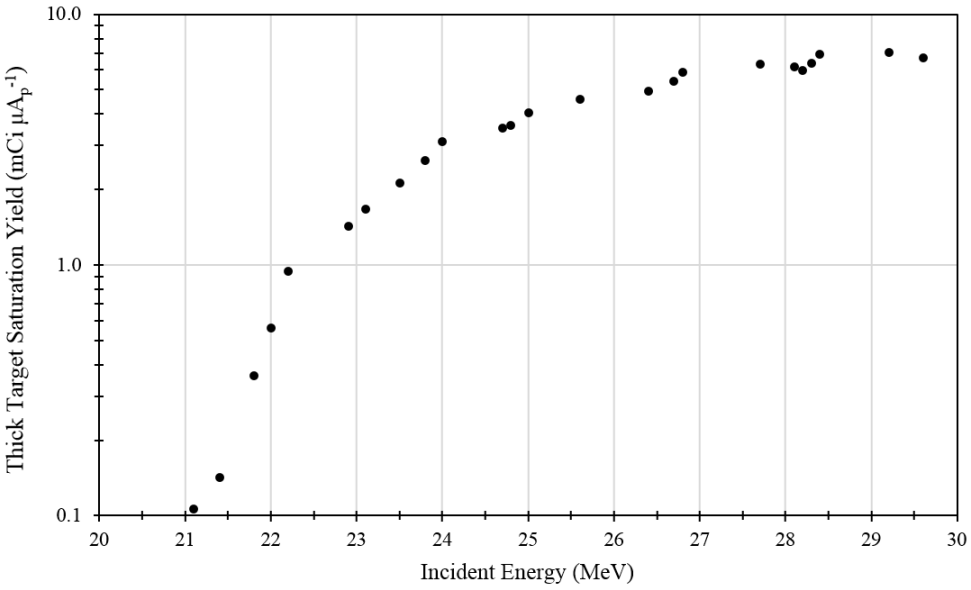

Figure 14. The thick target saturated yield is shown, as calculated, from 21.1-29.9 MeV.

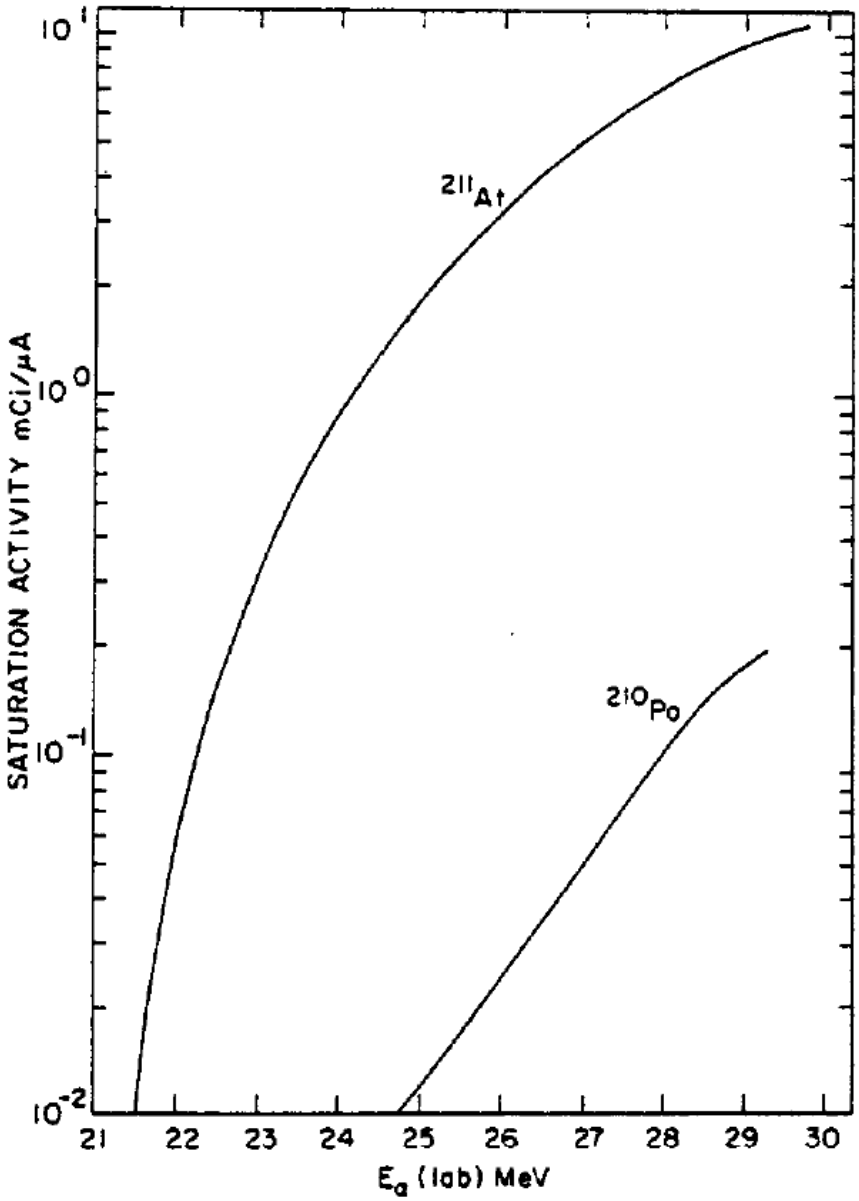

Figure 15. Published thick target yields are shown for comparison with the calculated data in Fig. 14.

The nuclear reaction code TALYS was used to estimate production yields and validate the theoretical calculations. In the TALYS code, multiple nuclear models are used

to simulate nuclear reactions, and provide complete reaction channel and yield analysis for given bombardment parameters (Koning 2008). The relevant input and output decks are provided in Appendix B, along with the results. In summary, negligible impurity production was expected at energies below 26.8 MeV. Production thick target yields for ^{211}At were calculated as 16.2 – 23.5 MBq μA_p^{-1} h^{-1} for 4 h bombardments of 26 MeV incident particles, resulting in a thick target saturation yield of approximately 116.6 MBq μA_p^{-1} (3.15 mCi μA_p^{-1}), comparable to the analytical estimates of 159.5 MBq μA_p^{-1} (4.31 mCi μA_p^{-1}). The yield calculated using TALYS falls in the middle of the range reported in the literature (c.f. Table 4), and is approximately 25% lower than the analytical solution at 26 MeV.

2.3 Recovery Methods

There are various recovery methods used to separate ^{211}At from the target bismuth material and other impurities. Most researchers utilize dry distillation, while some have investigated wet chemistry recovery methods. Here, chemical methods will be briefly discussed, followed by an in-depth analysis of the dry distillation methods used in these sets of experiments.

Few groups have pursued the route of wet chemistry recovery methods as a feasible method for routine distillation of ^{211}At. However, from an automation and routine production standpoint, wet extraction methods may be more consistently reproducible,

and are certainly easier to scale to production capabilities (Balkin et al. 2003; Yordanov et al. 2004). Liquid methods would also be more easily implemented in standard-sized module enclosures utilized in existing facilities. The insulation and component size needed for dry distillation methods dictate a reasonably large volume to incorporate the furnace and cold trap in well-shielded hot cells or chemistry module enclosures. The reduction in needed space adds to the attractiveness of liquid recovery methods.

One seldom used method of ^{211}At production is via decay of ^{211}Rn. Maeda et al. pursued this route as a generator system, however little further development has occurred. This lack of interest is primarily due to several logistic details, as well as the relatively exotic production method, consisting of 60 MeV ^{7}Li particles incident on a natural lead and bismuth targets to produce both bismuth, and astatine directly, via the ^{209}Bi(^{7}Li, 5n)^{211}Rn and ^{nat}Pb(^{7}Li, xn)$^{209\text{-}211}$At reactions (Maeda et al. 2015). Considerable chemistry and radionuclidic purity issues are present with this method.

More practically, papers by Balkin, Bourgeois, and Zona have explored wet extraction of astatine produced by the standard (α, 2n) reaction (Bourgeois et al. 2008, Zona et al. 2008, Balkin et al. 2013). Balkin focused on wet chemistry methods dissolving the irradiated bismuth target in concentrated nitric acid. The acid was removed by distillation at relatively low temperatures to prevent volatilization of astatine, and the residue was re-dissolved in hydrochloric acid. The ^{211}At was extracted from this solution into di-isopropyl-ether (DIPE), and thence back extracted from DIPE into sodium hydroxide. Extraction yields resulted in 71-78% efficiencies over many experiments (n=55). However, the difficulty arises in the various ionic states of the recovered astatine.

HPLC analysis showed significant variations in astatide, astatate, and other species, and occasional inclusion of trace impurity metals, which complicated further labeling steps. Zona et al. pursued a very similar procedure to Balkin, with yield claims in the 90-97% range. However, the various astatine ionic states remained a problem (Zona et al. 2008).

Bourgeois et al. pursued a wet chemistry recovery method, however they differed in extracting the astatine by binding it to a stannylated active ester (*N*-hydroxysuccinimide-*meta*-trimethylstannylbenzoate ester, MeSTB) and extracting it with DIPE in the presence of *N*-chlorosuccinimide (NCS). This proved beneficial in further immunoconjugation techniques, as so called NHS/EDC coupling chemistry is a widely-used method (Fischer 2010). In this technique, *N*-hydroxysuccinimide (NHS, which forms the base of MeSTB), is used with (*N*-(3-dimethylaminopropyl)-*N'*-ethylcarbodiimide hydrochloride) (EDC) and several buffers to link proteins, such as monoclonal antibodies, to other molecules (Lewis et al. 2001, Fischer 2010, Bartczak and Kanaras 2011). The procedures used by Bourgeois resulted in 85% recovered yields, with 20-25% labeling yields. This method showed promise for radiopharmaceuticals based on tin precursors, but may prove difficult for other delivery molecules. A similar method by Rajerison produced rhodium complexed radioastatine and radioiodine following extraction utilizing hydrochloric acid and DIPE back extraction. Again, this showed decent recovery efficiencies, but with limited end-use capabilities (Rajerison et al. 2014).

2.3.1 Dry Distillation

Dry distillation makes use of the relatively low boiling point of astatine (336.8 °C), by heating the target and extracting the gaseous product. In most applications, this consists of a quartz crucible that contains the target within a miniature tube furnace. The crucible is sealed, apart from a flow of inert gas which is used to entrain volatilized astatine and carry it to another location for capture. The gas flow is normally extracted through microcapillary tubing. There are two primary methods of astatine recovery following volatilization. In the cold trap method, the outlet capillary is coiled and immersed in a cold bath, such as a mixture of methanol or ethanol and dry ice. The cold trap, at -70 to -80 C, causes the astatine to solidify and remain in the capillary. Various eluents are then used to extract the astatine from the capillary tubing (Friedman et al. 1977, Larsen et al. 1996, Lindegren et al. 2001, Zalutsky et al. 2001). In the direct recovery method, the volatilized astatine is bubbled through chilled chloroform, which captures the astatine directly (Zalutsky et al. 2001). Either method is suitable for conjugation to tin-based immunoconjugates or other labeling modalities (Aneheim et al 2015b, 2015c, 2015d).

The basic procedure is to introduce the irradiated bismuth and aluminum target into the room temperature, or lightly preheated, furnace, on a quartz plate or crucible. Quartz can withstand significantly higher temperatures than required for the distillation, and will contain the liquefied aluminum and bismuth mixture. If practical, it is beneficial to remove the bismuth/astatine layer from the aluminum target backing to reduce the distillation time, as well as remove an additional source of contaminants. Once sealed, the

furnace is heated, and a flow of dry argon or nitrogen is used to purge the crucible volume during the heating. Once the operational temperature range is reached, the gas flow will entrain the gaseous astatine and remove it from the crucible. Gas is passed at a volumetric flow rate in the range of 15-50 mL min^{-1} (Aneheim et al. 2015a). The experimental configuration used in these experiments is shown in Fig. 16.

A nominal temperature profile for the furnace and target as a function of time is provided in Fig. 17. This shows the initial furnace temperature profile and phase change temperatures of the elements involved. Also shown is the approximate target temperature as a function of time. In preliminary studies, the target temperature was recorded using a blank target sample and an infrared thermometer through the quartz tubing, so temperatures are only approximate. The nominal temperature profile shown is developed based upon furnace capabilities, as well as empirical measurements from the literature (Hadley et al. 1991, Lindegren et al. 2001). A summary of representative distillation yields from the literature is given in Table 7.

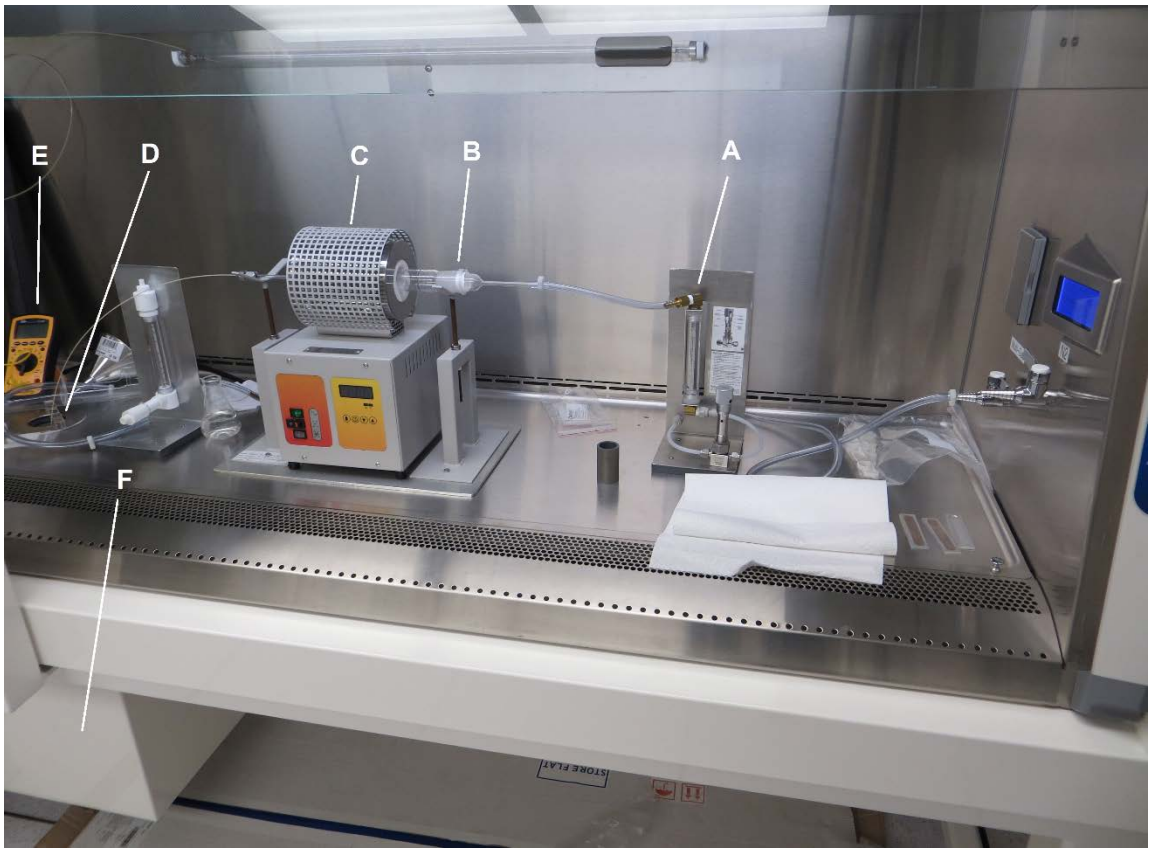

Figure 16. The distillation setup is shown. Argon is flowed through the regulator on the right (A), through the quartz tube (B) located within the tube furnace (C), and then through the capillary on the left into the cold trap (D). The cold trap is monitored for temperature (E) and is located in the shielded dose calibrator well (F), which allows for online monitoring of radioactivity (qualitative only).

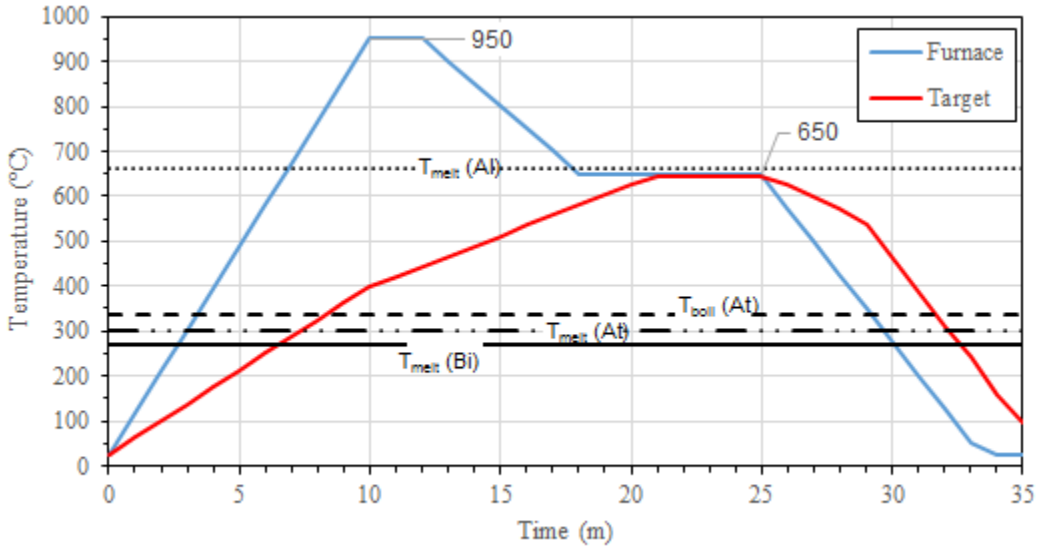

Figure 17. The temperature of the furnace and target during the distillation procedure are shown as a function of time.

Table 7. Dry distillation yields are shown as a function of distillation temperature as summarized from the literature (Hadley et al. 1991). The sources used somewhat arbitrary temperature binning. Recovered yields varied wildly.

Furnace Temperature (°C)	Recovered Yield (%)
600	29
600-625	44
600-650	21, 58, 18
625-675	19
650-675	30
650-700	75, 52, 45, 20

Using the dry distillation method, gaseous distillate activity concentration as a function of time and flow rate can be approximated by

$$C(t) = C_0 e^{-\left(kFt/V\right)} \tag{20}$$

where $C(t)$ is the activity in the still at time t, C_0 is the initial activity, k is an experimental constant, F is the average argon volumetric flow rate, V is the still volume, and t is the time (Nagatsu et al. 2014). The assumptions are that distillation starts immediately at time $t = 0$, that temperature is constant at some value above the boiling point of astatine, and that there are no losses or secondary trapping effects. However, this approach is overly simplistic and does not consider several factors, including the time taken to ramp the furnace to distillation temperatures, fractional bypassing of the cold trap, and non-uniformities in target heating and astatine migration or diffusion within the bismuth matrix. Importantly, the surface tension of molten bismuth and mobility of astatine bubbles may significantly slow this process.

2.3.2 Elution

Recovery of the solid phase astatine from the capillary tubing requires flushing with a solvent or carrier phase. In this process, the capillary coils are removed from the cold trap and allowed to warm to room temperature. A small amount of fluid is then passed

through the capillary, into a recovery vial. Alternatively, the eluent may be passed back and forth through the capillary repeatedly, to increase recovered yield.

Preliminary experiments showed poor elution with ethanol, with much better results when sodium citrate solution was used. Others have used methanol to good success in a similar process (Ogawa et al. 2015). Methanol mixed with N-iodosuccinimide (MeOH/NIS), a mild oxidant, has shown good eluent yields on the order of 90%. This is comparable with the effective, but less desirable, elution yields of chloroform (Aneheim et al. 2015a). Chloroform was used widely in initial astatine recovery experiments, and has been shown to be a good eluent with high recovery yields. This has been especially helpful in preclinical trial situations, where the astatine/chloroform solution is stable for several hours. However, there are two main drawbacks. First, chloroform tends to be "messy" in the laboratory, having a relatively low boiling point, and correspondingly high vapor pressure and volatility. Coupled with the volatility of astatine, this can lead to contamination of the work area, especially in the preclinical environment. Second, most immunoconjugation procedures of interest with astatine are not conducive to use with chloroform. In these instances, the chloroform must be evaporated, with the astatine dissolved into another carrier (Aneheim et al. 2015a).

It is desirable to use a minimum amount of eluent to maintain a high specific activity. Labeling efficiency and activity concentration are highly dependent upon minimizing eluent volume. For example, commercially available radionuclides, such as ^{125}I, are available in the range of 5-10 mCi per 100 μL. Because of the predominantly low beam currents available for astatine production as most facilities, and the resulting low

produced activity, it is imperative to use the minimum eluent volume possible. However, this is compounded by flushing efficiency. Reports of 20-40% recovery per 500 μL flush are common, contrasted with 60-90% recovery for 1 mL to 3 mL flushes (Lindegren et al. 2001, Nagatsu et al. 2014). One strategy, implemented in these experiments, is to repeatedly flush with the original 0.5 mL volume. Other limiting factors are the dead volume involved with the coiled capillary cold trap, as well as difficulties in handling such small volumes both routinely, and reproducibly.

High specific activity is a critical factor in the radiolabeling process, as well as in *in vivo* studies. First, specific activity can greatly affect the required volumes and labeling efficiencies during immunoconjugation. This is even more apparent when performing colloidal nanoparticle synthesis with incorporated radioactivity, as the distribution of radioactive atoms per nanoparticle is entirely dependent upon specific activity (Kannan et al. 2006, Paciotti et al. 2006, Chattopadhyay et al. 2010, Kang et al. 2010). Second, specific activity, in terms of total administered mass, can affect both *in vivo* effects of the drug by altering cell receptor sensitivity, or by toxicity. These effects are carefully studied in preclinical and Phase I clinical trials (Hoffman et al. 2001, Pruszynski et al. 2015).

2.3.3 Preparation for End Use

As stated previously, use of automated methods to reduce manual processing in synthesis and labeling operations is crucial for adapting ^{211}At to routine production for

widespread phase II and phase III clinical trials, as well as commercial uses (Aneheim et al. 2105a, 2015d). Contrary to manual labeling methods, future routine production chemistry will likely lean towards astatination of active molecules (mAb's, peptides, proteins) after the linking molecule has been conjugated to the biomolecule complex. This approach has several advantages. First, having as many steps accomplished prior to astatination reduces the lead time between end-of-bombardment and end use. This also reduces the amount of time the complex molecules are in the presence of the high specific activity alpha radiation, which can lead to radiolysis and degradation of the drug over time (Pozzi and Zalutsky 2005a, 2005b, 2007, 2017). Second, studies have shown that conjugated biomolecule precursor material can be prepared in advance and stored for long periods, provided proper temperature and pH conditions are met (Aneheim et al. 2015c). Advance preparation allows components to be shipped and stored similarly to other components in common cyclotron produced drugs in current use.

Several standard methods are in use for astatination of biomolecules. The most widely used method involves the coupling of a stannylated succinimide ester to lysine on a mAb of interest. Astatine is then substituted for the $Sn(CH_3)_3$ group via an electrophilic substitution reaction using N-iodo-succinimide (NIS) (Aneheim et al 2015d). An exhaustive analysis of vial and column rinse efficiencies has been compared by the same group for various solvents, including 5% NIS solution in methanol, methanol, ethanol, acetonitrile, 2-propanol, citrate, 15% methanol diluted in citrate, and 50% methanol diluted in citrate. Of these, the reference 5% NIS solution in methanol gave by far the best results (Aneheim et al. 2015d). This research has built on the similar methods developed

by the earlier users (Aaij et al. 1975, Garg et al. 1990, Foulon et al. 1996, Larsen et al. 1998c).

It is critical during recovery, elution, preparation, and labeling, that all processes and steps conform to FDA-mandated current Good Manufacturing Practices (cGMP) and United States Pharmacopeia standards, specifically USP 797 guidelines for pharmaceutical compounding. Chemical and microbial purity must be maintained at all times during the manufacture of drugs intended for human use. While this is not necessary for preliminary *in vitro* studies, it is beneficial to conform to these standards as it allows an easy transition into preclinical and clinical trials (Anaheim et al. 2015d).

2.4 Product Analysis

Radioactive and chemical analysis of the recovered astatine and end-product is essential for fully characterizing and understanding *in vitro* and *in vivo* behavior. Radioactive analysis, for determining radiochemical yield (RCY), radionuclidic purity (RCP), specific activity, and process efficiency, is carried out using radiation detection methods. This may be facilitated by gamma-ray spectroscopy, alpha spectroscopy, or other methods. Chemical analysis may be performed by use of electron microscope, high-performance liquid chromatography (HPLC), or reactions with specific reagents capable of detecting impurities (Frier and Hesslewood 1980, Mock et al. 1997, Yu 2006). A focus

on radioactive analysis is provided herein, as more than basic chemical analysis is beyond the scope of this study.

2.4.1 Detector Calibration and Analysis

The industry standard method for analysis of cyclotron produced radionuclides is via gamma spectroscopy. While not without some drawbacks, gamma spectroscopy provides a relatively quick and well-proven method, that is sensitive to radionuclides intended for medical use (Knoll 2000). In all cases, it is preferable to use detectors with high energy resolution, such as high purity germanium (HPGe), as opposed to inorganic scintillators such as NaI and CsI. The increase in availability and decrease in cost of HPGe detectors over the last decade, as well as improvements in cooling methods (e.g., mechanically cooled), make it unreasonable to use detectors with inferior energy resolution for radiopharmaceutical purity measurements.

While gamma-ray spectroscopy is the method most commonly used, some groups have used alpha spectroscopy to determine ^{211}At and ^{210}At/Po purity (Schultz et al. 2006). However, alpha spectroscopy requires extensive preparation of standards and samples which are not needed with the accuracy and availability of high-energy-resolution gamma spectroscopy.

2.4.1.1 Gamma-ray Spectroscopy

Gamma-ray spectroscopy of cyclotron produced ^{211}At is carried out utilizing a liquid nitrogen cooled HPGe detector with fixed geometry and shielding. The experimental setup consists of a Canberra HPGe detector system (Canberra Industries, Inc., 800 Research Parkway, Meriden, CT 06450), utilizing an Inspector 2000 multichannel analyzer (MCA) and Genie data acquisition software package. Prior to analysis, the detector system is calibrated using NIST traceable radionuclide sources consisting of ^{57}Co ($T_{1/2}$ = 271.74 d) and ^{137}Cs ($T_{1/2}$ = 30.07 y) (RadQual, LLC, P.O. Box 82, Weare, NH 03281), as well as ^{152}Eu ($T_{1/2}$ = 13.517 y) (Eckert and Ziegler Isotope Products, Inc., 24937 Avenue Tibbitts, Valencia, CA 91355). Alternatively, a combination of ^{133}Ba and ^{137}Cs may be used, as their emissions cover most of the energy range of interest for these purposes. The useful spectral lines and intensities of these sources, and spectral lines related to ^{211}At/^{211}Po, are presented in Table 8 (Turkington 1993, NNDC 2016).

Table 8. Gamma and x-ray spectra and intensities are provided for the calibration sources and ^{211}At.

Energy (keV)	Yield (Bq^{-1} s^{-1})	Radionuclide	Energy (keV)	Yield (Bq^{-1} s^{-1})	Radionuclide
14.4	9.16×10^{-2}	^{57}Co	356.0	6.20×10^{-1}	^{133}Ba
76.9	1.27×10^{-1}	^{211}At	383.8	8.94×10^{-2}	^{133}Ba
79.3	2.11×10^{-1}	^{211}At	569.7	5.35×10^{-3}	^{211}Po
81.0	3.29×10^{-1}	^{133}Ba	661.7	8.51×10^{-1}	^{137}Cs
121.8	2.85×10^{-1}	^{152}Eu	687.0	2.61×10^{-3}	^{211}At
122.1	8.56×10^{-1}	^{57}Co	897.8	5.51×10^{-3}	^{211}Po
136.5	1.07×10^{-1}	^{57}Co	964.1	1.45×10^{-1}	^{152}Eu
244.7	7.55×10^{-2}	^{152}Eu	1086	1.01×10^{-1}	^{152}Eu
276.4	7.16×10^{-2}	^{133}Ba	1112	1.37×10^{-1}	^{152}Eu
302.9	1.83×10^{-1}	^{133}Ba	1408	2.09×10^{-1}	^{152}Eu
344.0	2.83×10^{-2}	^{152}Eu			

Activity measurements are performed by correlating detected characteristic photon peaks to the radionuclides found present in the target sample. Calibration must be performed using a consistently repeatable geometry, such that solid angle and efficiency changes are kept to a minimum. Two counting locations are used in the experimental setup. The primary location is centered 200 cm from the detector face, and is partially surrounded by lead shielding blocks, with an opening towards the detector. This location is used to count bulk samples, such as the entire target, and is separated from the detector

by this large distance to reduce dead time to an acceptable level. This is especially important for initial target measurement, when short-lived impurities, such as ^{28}Al ($T_{1/2}$ = 2.245 min, $E\gamma$ = 1779 keV, 100%), are dominant. A second counting location was constructed using low-density polypropylene and was designed to hold a sample vial in a vertical position approximately 10 cm from the detector face. This position was used for small aliquots of activity. Activity at the end of bombardment, A_i (Bq), for a given radionuclide i, was calculated using Eq. (21)

$$A_i = \frac{\lambda_i N_{i,\gamma}}{\varepsilon_\gamma y_{i,\gamma}} e^{-\lambda_i t_{EOB}} \left(e^{\lambda_i t_1} - e^{\lambda_i t_2} \right) \tag{21}$$

where $N_{i,\gamma}$ is the number of net counts for photon γ from radionuclide i, λ_i is the decay constant of the radionuclide i (s^{-1}), ε_γ is the absolute efficiency for photon γ, $y_{i,\gamma}$ is the relative emission intensity of photon γ from radionuclide i, t_{EOB} is the bombardment time (s), t_1 is the time between EOB and initial counting time (s), and t_2 is the elapsed counting time. Quantities dependent upon experimental setup, such as ε_γ, are determined experimentally beforehand using NIST calibration sources. Background spectra are measured and subtracted from the experimental spectra using automatic algorithms contained within the Genie analysis software. Using ^{133}Ba and ^{137}Cs sources, with a standard background subtraction, the detector efficiency and energy calibrations may be performed. For preliminary purposes, all calibrations are performed at the 2 m counting location.

The detector efficiency at the 2 m location is shown as a function of gamma energy in Fig. 18. The detector energy calibration, showing the relationship between gamma energy and MCA channel number, is shown in Fig. 19. This fit a linear relationship very well, which was desirable. The proportionality should become nonlinear at low energies (approximately below 50 keV), however, this effect should be negligible for detection of the photons of interest listed in Table 8. Peak width, in terms of full width at half maximum (*FWHM*), is shown as a function of energy in Fig. 20, in units of keV. *FWHM* is defined as 2.35σ for Gaussian distributions, where σ is the standard deviation in counts. Radiation interactions follow a Poisson distribution, which very closely approximates the Gaussian distribution for a large number of events, and allows for easy discretization using the discrete number of MCA channels available (Knoll 2000). The dimensionless energy resolution, *ER*, is given by Eq. (22)

$$ER = \frac{FWHM}{E} \tag{22}$$

where *FWHM* and *E* are in units of keV. Energy resolution is shown as a function of energy in Fig. 21, and shows a value of approximately 0.2% at 661.7 keV, which is consistent with expected results.

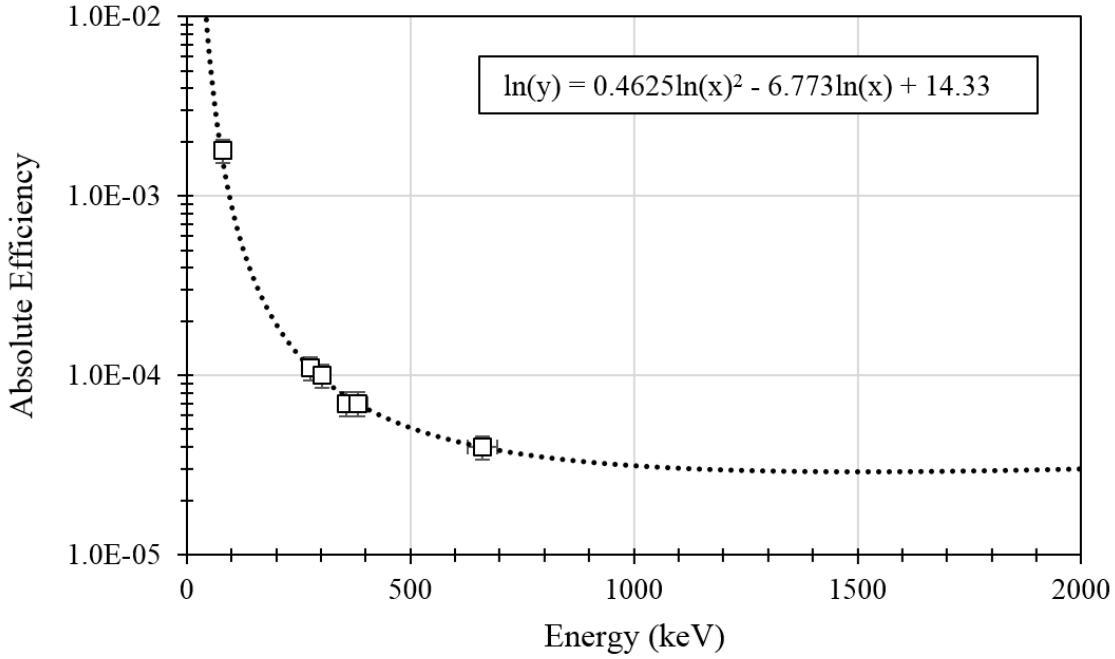

Figure 18. Detector efficiency for the 2 m source location.

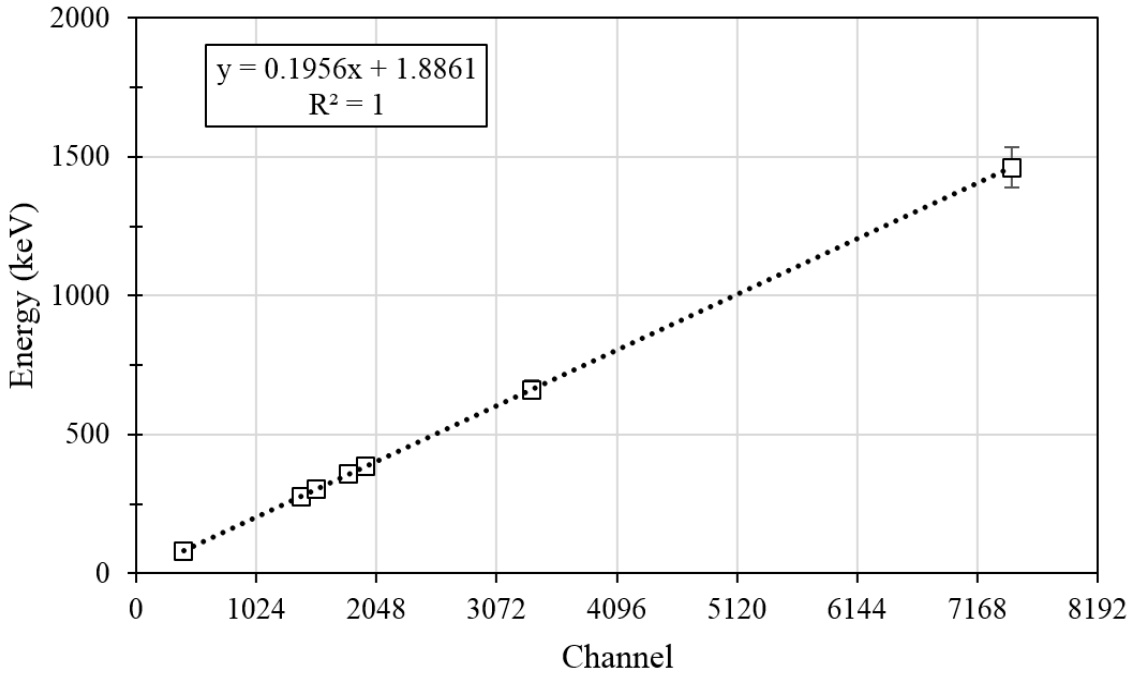

Figure 19. Linearity between photon energy and channel number.

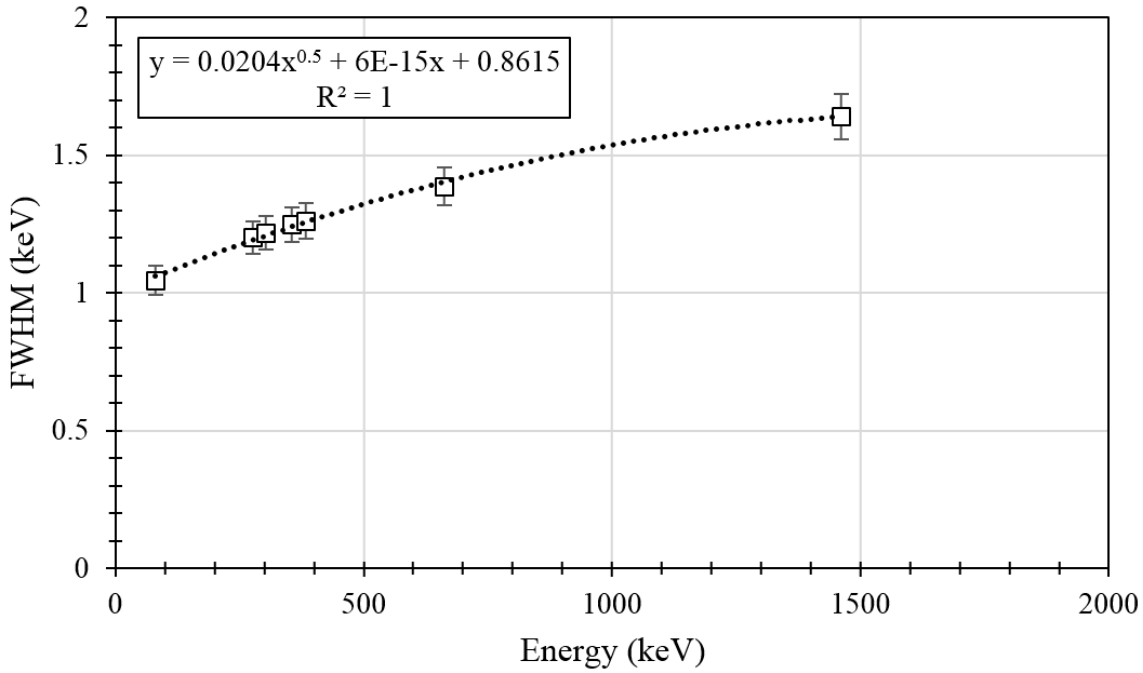

Figure 20. Peak width in *FWHM* is plotted as a function of energy.

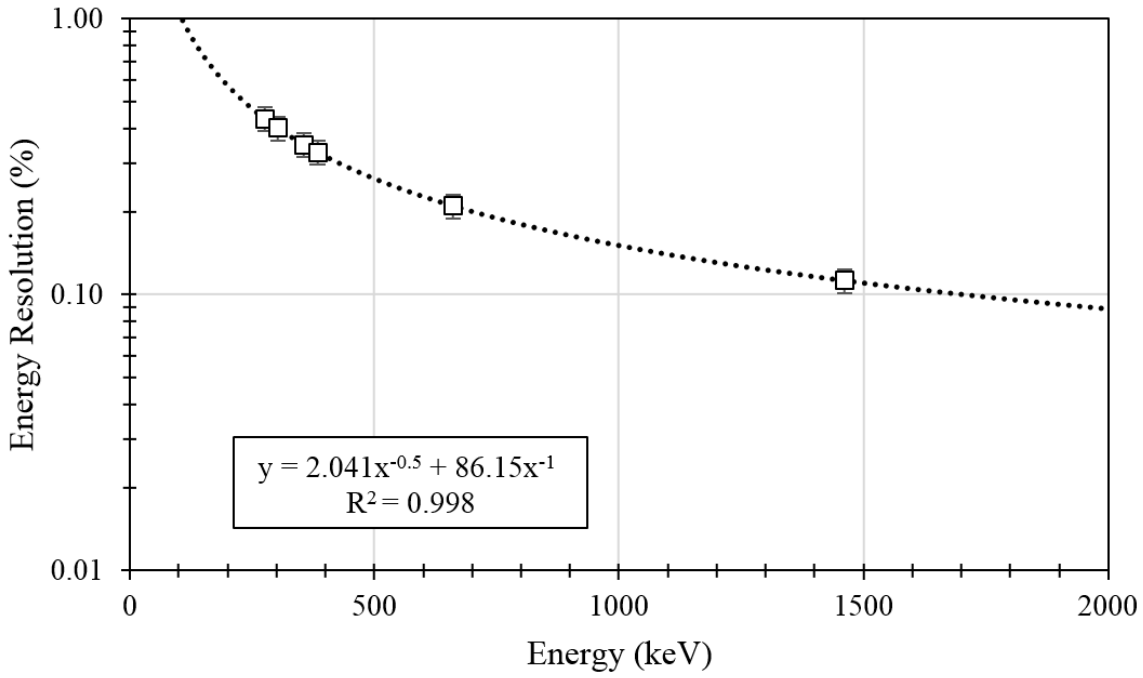

Figure 21. Energy resolution, in percent, as a function of energy.

spectroscopy. Utilizing activity calculations obtained via Eq. 21, the normalized production yield, Y (Bq $\mu A^{-1} h^{-1}$), can be calculated using Eq. (23)

$$Y = \frac{3600 A_i}{\int_o^{t_{EOB}} Q(t) dt} \tag{23}$$

where the integral over total cumulated cuurent (charge) given the total bombardment time in μA_p-s. In addition to yield analysis, identification of impurity radionuclides can be performed using standard spectroscopic analysis techniques (Groppi et al. 2005). Dominant gamma lines of expected impurities, namely ^{210}At and ^{210}Po, are given in Table 2. Other expected gamma lines include ^{28}Al, which will be present in the aluminum target holder and target backing. Secondary neutrons produced by the incident beam undergo radiative capture reactions on the natural ^{27}Al. However, the activated aluminum dies off quickly, with a half-life on the order of 2 minutes. Residual activity is expected to be detected in the initial target assay, however, none should be present in eluted samples following distillation. Other low-level background radiation is expected from activated cyclotron components elsewhere in the facility, as well as ^{40}K and other naturally occurring radionuclides.

2.4.1.2 Ion Chamber Measurements

Dose calibrators are widely used in nuclear medicine as means of efficiently measuring and verifying the activity of radiopharmaceuticals prior to patient administration. Dose calibrators typically consist of a pressurized ion chamber surrounding a well in which a dose vial or syringe can be placed. An example of a typical dose calibrator, and the same model used in these experiments (Biodex Atomlab 500, Biodex Medical Systems, Inc., 20 Ramsey Road, Shirley NY 11967), is shown in Fig. 22. As the detector in use is an ion chamber, air-kerma values are measured, and energy discrimination of emissions is not possible. Additionally, geometry dependence can be very extensive (Rayburn 2007). Generally, a set of 2-5 calibration sources of various radionuclides are used to calibrate the detector and to provide daily quality assurance checks. These sources must be NIST traceable for preclinical and clinical use. Calibration factors, or so called dial values, are set for these radionuclides. Dial values for other radionuclides are preset at the factory, using Monte Carlo simulation, empirical determination, or other methods. These values are adjusted based on any differences when using the calibration sources. This will consider variations in temperature, voltage, and any other effects (Rayburn 2007).

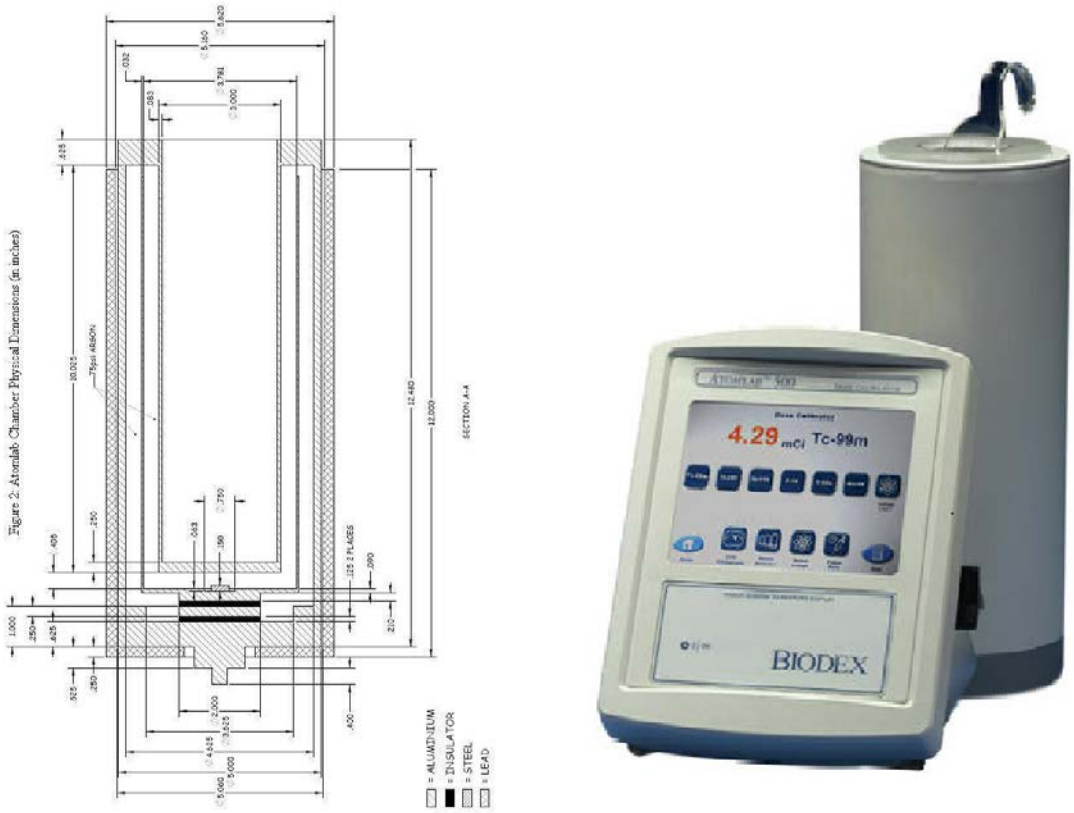

Figure 22. The Biodex Atomlab 500 dose calibrator is shown, with ion chamber dimensions (Rayburn 2007, © Biodex 2016). Reprinted from Rayburn 2007.

Sealed dose calibrators are incapable of detecting alpha particles or beta particles below 1-1.5 MeV, due to wall thickness. Bremsstrahlung photons from higher energy betas can provide some signal, although this is generally very unreliable. The wall thickness required to contain the pressurized detector gas also poses additional complications for low-energy photons, of approximately 70 keV and below. This energy range is in line with the x-rays produced by ^{211}At and ^{211}Po. These complications are

exacerbated by the geometry, container, and constitution of the sample being measured, due to significant attenuation and cubic dependence upon atomic number (Rayburn 2007).

One method of circumventing this difficulty in activity measurements is to empirically determine dial values by cross calibration with a different detector, such as an HPGe (Siegel et al. 2004, Balkin et al. 2013, Bergeron et al. 2014). As seen in Fig. 18, germanium detector efficiency is nonlinear at low energies, and as discussed, energy calibration can become difficult at low energies. These nonlinearities, coupled with the poor dose calibrator response to low-energy photons, makes it preferable to set dial values by using the emitted gamma-rays in the 600-900 keV range, even though the emitted yield is much lower. Using a different brand of dose calibrator (Capintec, Inc., Model CRC-15R), Balkin et al. calculated a dial value of 46 (Balkin et al. 2013). A recent version of the AtomLab 500 manual provides a factory dial value for ^{211}At of 61.6 (Biodex 2016). This is convenient, as comparison between dial values as a function of radionuclide for the different manufacturers has shown little to no correlation (Siegel et al. 2004).

Due to uncertainties related to volume of eluent, differences in container medium, and the lack of significant literature on the use of dose calibrators with ^{211}At for quantitative measurements, the ion chambers will be used for qualitative purposes only. Aliquots in standard vials will be measured with the dose calibrator; values will be closely examined in conjunction with HPGe measurements to validate the quantitative use of dose calibrators for future experiments. The dose calibrator located next to the distillation apparatus will be used for qualitative on-line measurement of eluted activity. In Fig. 16, location (F), the capillary coil and cold trap are located within the dose calibrator well.

Measured activity as a function of time will be used to confirm that distillation has reached a practical maximum. Referring to Eq. (20), and the expected temperature profile shown in Fig. 17, an expected cold trap activity can be estimated, as shown in Fig. 23.

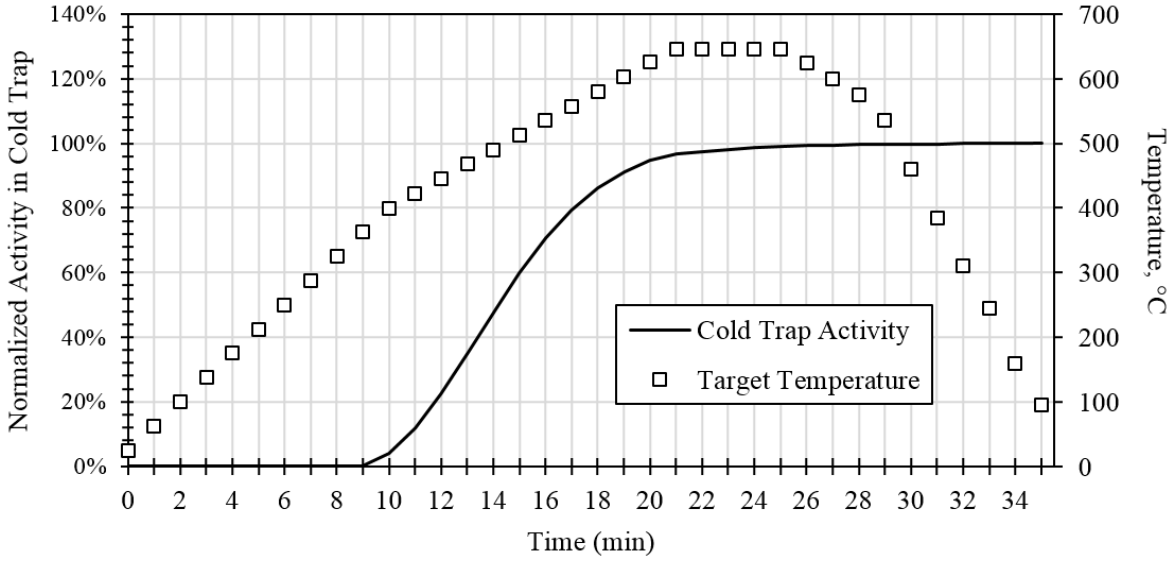

Figure 23. Expected cold trap activity, as measured by the dose calibrator, is shown as a function of time.

In Fig. 23, the rate of release of activity from the target is assumed to vary linearly with the temperature difference between the target and the melting point of bismuth, above the astatine boiling point threshold. It is expected that the astatine will be more easily extracted from the target as the bismuth reaches a higher temperature, allowing a greater diffusion rate through the material. The dose calibrator measurements will be used to

estimate when the plateau has been reached, approximately between 22 and 24 minutes after the beginning of distillation.

2.4.2 Radionuclidic Purity and Radiochemical Yield

The activity of each radionuclide can be measured by the HPGe detector, as demonstrated in the above section. While bulk activity measurements are useful in determining the initial target activity and the completion of distillation, the activity of each individual radionuclide is crucial for determining the radiochemical yield (*RCY*) and radionuclidic purity (*RCP*). Both quantities are used when determining the quality of a radiopharmaceutical product, especially as it applies to the suitability for clinical use (Clark 1990). These values also give an indication of the quality assurance and quality control procedures provided in a specific process (Decristoforo et al. 2000).

Radionuclidic purity gives an indication of the amount of impurity radionuclide present in a sample. Activity measurement of individual radionuclides is accomplished utilizing Eq. (21) and the gamma-ray spectrum of the product after distillation and elution. It is conventional to define *RCP* in terms of activity, although in some early cases it has been reported in terms of mass fractions (Smith 1964). Units are generally in terms of μCi of impurity per mCi of product, especially when given as limits by USP standards. In research, *RCP* is more commonly given in percentage of total activity. Radionuclidic purity can be quoted both prior to labeling, and for the end product. When quoted in

manufactured radiopharmaceuticals, the *RCP* is always quoted in terms of the end-product. However, in preclinical research, it can be beneficial to measure the *RCP* through various phases of the entire process.

Radiochemical yield is primarily quoted after the entire processing, labeling, or immunoconjugation process is completed. The *RCY* provides a measure of the efficiency of the labeling process, as well as an indication of the end use effectiveness (Eriksson et al. 2014). Radiochemical yield can be given by Eq. (24)

$$RCY = \frac{A_{product} RCP}{A_{reaction}}, \tag{24}$$

where $A_{product}$ is the total activity of the end product, $A_{reaction}$ is the total activity that went into the reaction, and *RCP* is given as the fraction of product radionuclide to total activity (Eriksson et al. 2014). This is not decay corrected, but can be done so using the standard method. Decay corrected activities are usually stated in terms of EOB activity.

2.5 Nanoparticle Formation

Colloidal gold nanoparticles may be formed with the inclusion of radiohalides for *in vitro* studies. Colloidal gold nanoparticles without radioactivity have been extensively studied in imaging and drug delivery research (Panchapakesan and Wickstrom 2007,

Gilijohann et al. 2010). Methods have been largely focused on increasing contrast in imaging due to high atomic number and specific organ or tumor uptake via targeted labelling (Kang et al. 2010); increased energy absorption to tissue in conventional radiotherapy and in laser ablation (Hainfeld et al. 2004, Chattopadhyay et al. 2010); and in enhancing quantification in pathology using surface-plasmon resonance and other optical properties (Jazayeri et al. 2016). Radioactive gold nanoparticles incorporating radioiodine (^{125}I) and ^{198}Au have been developed for internal radiation therapy and imaging purposes (Ting et al. 2010, Hamoui 2015, Clanton and Akabani 2016). We followed the one-pot modified Turkevich method described by Kumar, with modifications developed in the Systems Radiobiology Laboratory (Kumar et al. 2008, Clanton and Akabani 2016).

2.5.1 Nanoparticle Synthesis

Colloidal gold nanoparticles may be formed by the Turkevich method. In this process, $HAuCl_4$ in solution begins an aggregation process with the addition of a reducing agent, traditionally triosodium citrate ($Na_3C_6H_5O_7 \cdot 2\ H_2O$). In the case of sodium citrate, the citrate ions also act as capping agents, protecting the gold colloid and preventing further aggregation. Varying the relative concentrations of the reagents, and to some extent, the rate of addition of the reducing agent, controls the nanoparticle size (diameter) distribution; the reducing agent must be added quickly and consistently between experiments to maintain repeatability (Frens 1973). To produce approximately 50 mL of

30-40 nm diameter particles, at a concentration of 10^{11}-10^{12} particles mL^{-1}, the following steps are performed: 1) thoroughly wash all glassware with Aqua Regia (3 parts 5 N HCl, 1 part 6 N HNO_3), rinse with doubly-deionized (DI) water, and thoroughly dry; 2) bring 50 mL of DI water to a boil in a round bottom flask, with a condenser column attached to maintain volume; 3) prepare 1 mL of 12.7 mM $HAuCl_4$, and add it to the flask; 4) prepare 0.94 mL of 38.8 mM sodium citrate solution, and add it quickly to the reaction flask. Following addition of the sodium citrate, the reaction will take place over the course of 2-3 min. Visible changes in the color of the solution provide feedback as to the state of the reaction. After 0.5-1 min, the solution will begin to darken, transitioning first to a translucent grey and then to a light translucent blue. After 2-3 min, the solution will quickly darken to a deep ruby color, indicating completion of the reaction. The solution is boiled for a few more minutes to ensure the reaction has gone to completion, before removing from the heat. A depiction of the experimental apparatus is shown in Fig. 24.

Incorporation of radioactive halogens into the nanoparticles was first investigated with stable iodine. An equal mixture of sodium iodide (NaI) and sodium hydroxide (NaOH) were added to the original sodium citrate solution at 20 mM concentration. The reaction was carried out as previously, with no noticeable changes, indicating that the new reactants did not negatively affect the reaction. Several trials were carried out using no-carrier-added ^{125}I in 0.1 M NaOH, as obtained from Perkin-Elmer (940 Winter St., Waltham, MA 02451). Added activities ranged from 120 μCi to 2 mCi. Results showed nanoparticle formation and size distribution consistent with non-radioactive samples, and maintained 87-94% retained activity following washing and labelling procedures. This

indicated that most activity was bound to, or incorporated within, the gold nanoparticles. Similar results were expected when incorporating ^{211}At into the sodium citrate solution.

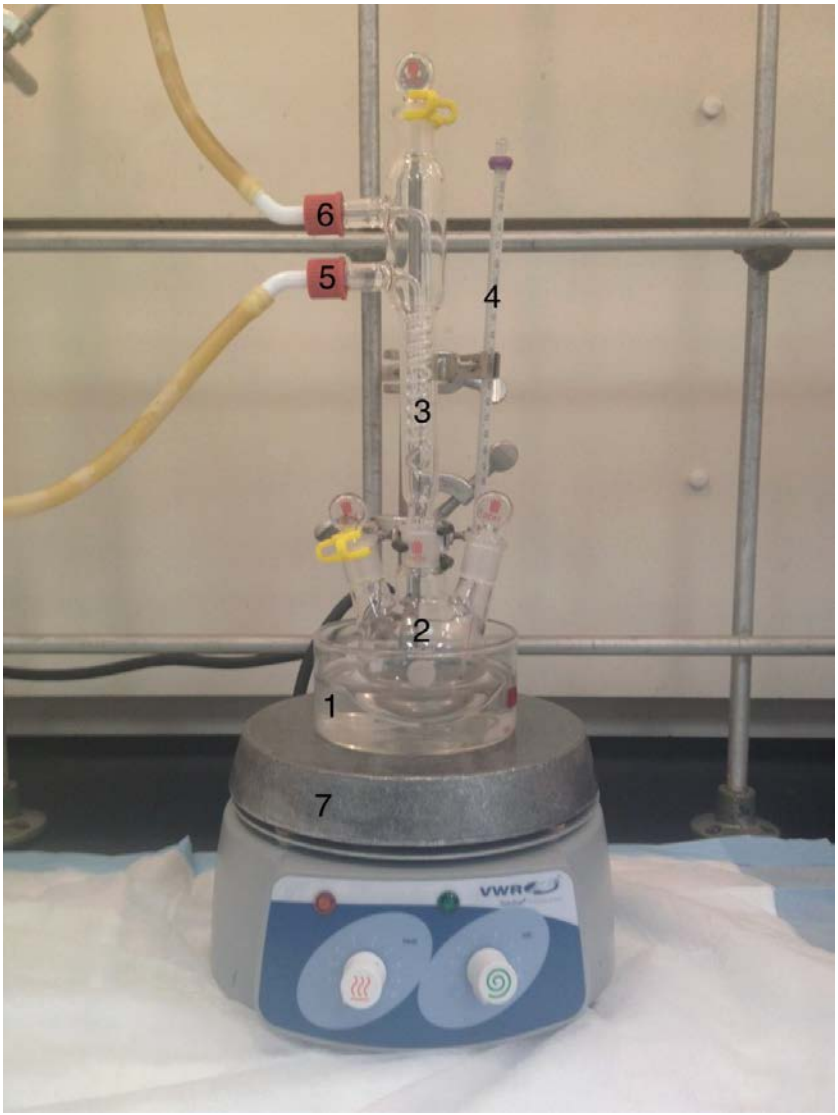

Figure 24. Experimental apparatus to produce gold nanoparticles: (1) crystallization dish, containing silicone oil and stir bar for heat transfer purposes; (2) 100 mL round bottom flask (3-neck), containing stir bar and reactants; (3) reflux column; (4) thermometer for measuring oil temperature; (5) cold water inlet for reflux column; (6) reflux water outlet; (7) hot plate.

As mentioned above, one method of controlling nanoparticle diameter is to vary the concentration of sodium citrate added to the reaction. This method is suitable for producing nanoparticles in the range of 10-50 nm in diameter. Smaller and larger particles may be obtained by utilizing different reducing and/or capping agents, such as sodium borohydride ($NaBH_4$) or hydroquinone ($C_6H_4(OH)_2$) (Jokerst et al. 2011). The concentration of sodium citrate was varied from 20 mM to 38.8 mM, while maintaining the same volumes. The resulting range of nanoparticle diameters are presented in Fig. 25. Here, measurements were conducted for 5 samples of each combination via TEM analysis (described below in section 2.5.3). Nanoparticle diameter error was calculated from measured quantities, while concentration error was assumed to be 5%.

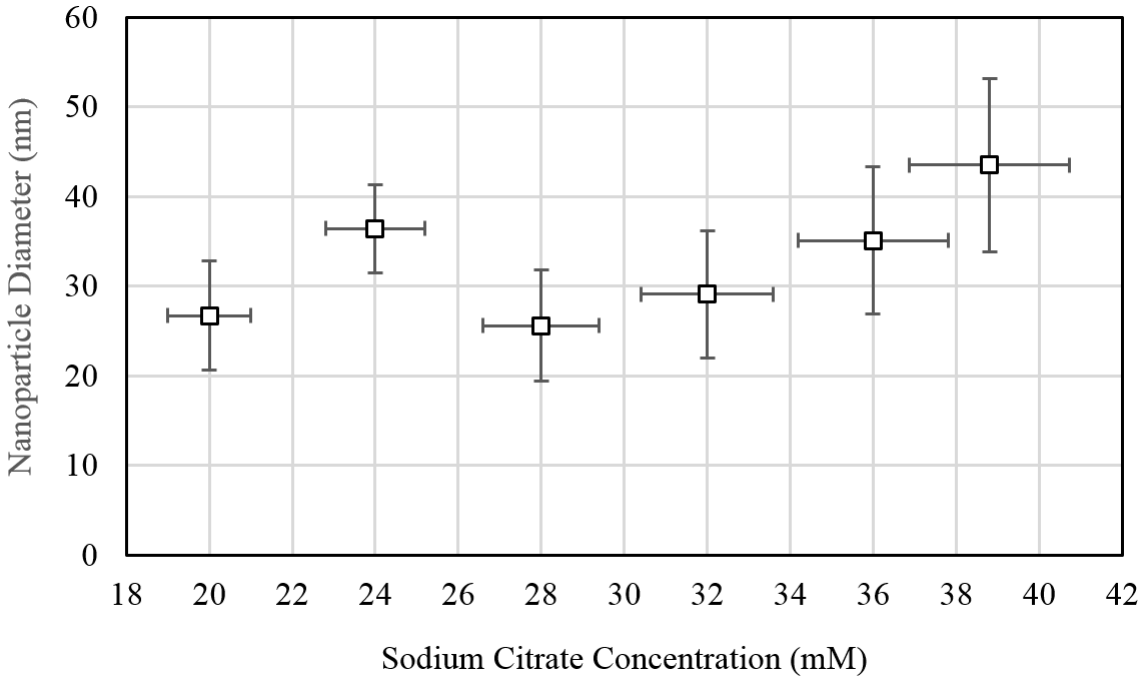

Figure 25. Gold nanoparticle size as a function of peak absorption.

When incorporating radionuclides in the formation process, the average number of radioactive nuclei per nanoparticle can be estimated using the Poisson distribution

$$P(k) = \frac{e^{\mu}\mu^{-k}}{k!} \tag{25}$$

where k represents the number of radioactive nuclei, $P(k)$ represents the probability of including k radioactive nuclei in each nanoparticle, and the average, μ, is the total number of radioactive atoms divided by the number of nanoparticles. This probability can be calculated based on known masses of reactants, added activity, and known nanoparticle

size and number density for a given reaction. It is apparent that nanoparticle size, the total reaction volume, and activity may be tailored to provide the desired results. As an example, 10 mCi of ^{211}At added to a reaction solution for producing 20 nm nanoparticles will have a large variation in the number of radioactive atoms per nanoparticle, dependent upon the total number of nanoparticles created. This is shown in Fig. 26 for reactions scaled to produce 10^8, 10^9, and 10^{10} nanoparticles.

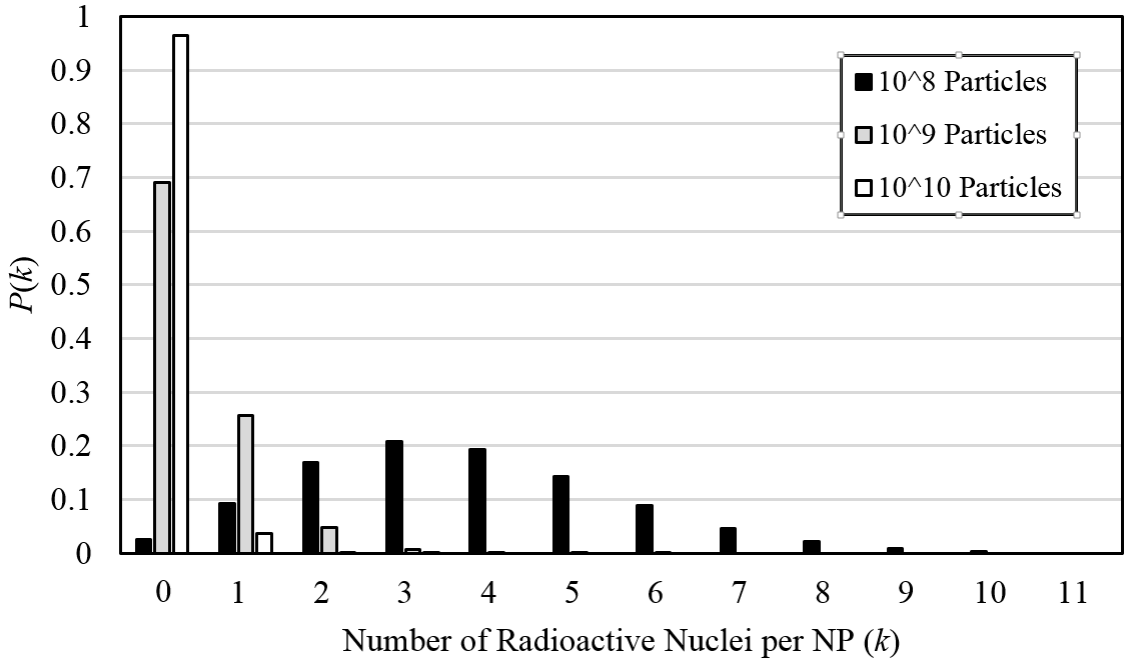

Figure 26. The probability of *k* number of radioactive atoms per nanoparticle is shown as a function of the total number of nanoparticles formed for 10 mCi of ^{211}At added to the reaction.

2.5.2 PEGylation and Labeling

Bare gold nanoparticles are unsuitable for *in vitro* and *in vivo* use, as they will aggregate in the biological environment, and have negligible circulation or uptake (Ting et al. 2010). It is therefore necessary to provide a surface protectant to limit aggregation, as well as to provide targeting properties. One method is to provide a biologically inert coating of polyethylene glycol (PEG) in a so-called "corona" (Ishii et al. 2004). In this case, 2-5 kDa PEG chains, labeled with a thiol group on one end, are put in solution with the gold nanoparticles at a ratio of 1000:1. The sulfur in the thiol compound covalently bonds to the gold nanoparticle surface, leaving the inert PEG corona to protect the nanoparticle, in a process known as PEGylation. In practice, variations in these PEG chains are included to tailor the chemical properties of the nanoparticles. Here, 2 kDa methoxy-PEG-thiol (CH_3O-$(CH_2CH_2O)_n$-CH_2CH_2SH), with the chemically inert methoxy group, is mixed in a ratio of 98:2 with 5 kDa carboxymethyl-PEG-thiol (CH_2COOH-$(CH_2CH_2O)_n$-CH_2CH_2SH). The carboxymethyl-PEG-thiol is greater than twice as long, such that the carboxymethyl- group is exposed on the PEGYlated nanoparticle surface. The carboxymethyl- group is activated for conjugation to targeting ligands (Fischer 2010). In a common technique, repeated here, *N*-hydroxysuccinimide (NHS) is used with (*N*-(3-dimethylaminopropyl)-*N'*-ethylcarbodiimide hydrochloride) (EDC) and several buffers to link proteins, such as monoclonal antibodies, to other molecules (Reist et al. 1999, Lewis et al. 2001, Fischer 2010, Bartczak and Kanaras 2011). In particular, anti-CD340 (ant-HER2) and EGFR (anti-HER1) were used to evaluate

specific and non-specific binding characteristics in the HER-2 positive SKBr3 cell line, similar to (Boskovitz et al. 2009).

2.5.3 Characterization and Measurements

Colloidal gold nanoparticles can be characterized by several methods. Two primary methods involve Transmission Electron Microscopy (TEM) and ultraviolet-visible spectroscopy (UV-Vis). Microscopic analysis consists of drying a sample of concentrated nanoparticles on a suitable sample grid, followed by TEM imaging. The resulting images are then analyzed using image analysis software, such as ImageJ, a tool provided through the NIH (Schneider et al. 2012). ImageJ was designed for analysis of medical DICOM images. The program can automatically create regions of interest (ROI), and can perform various measurement functions. The user can "calibrate" the software by measuring the standard included in the image. The user can also edit or manually add ROIs in images too complex for the built-in algorithm. The data from this analysis can be used to determine size distributions and to correlate number concentration, given the known volumes and masses used in the initial reaction. An example of a TEM image showing ~ 10 nm gold nanoparticles is provided in Fig. 27.

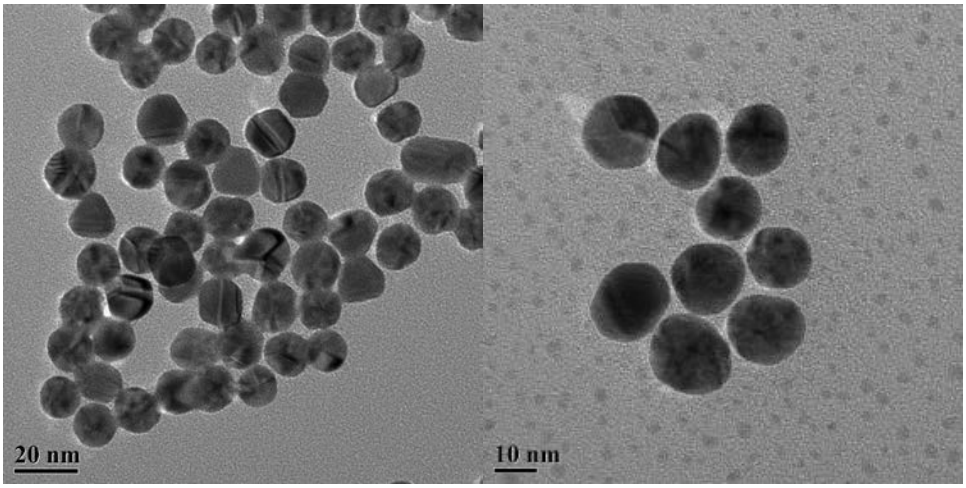

Figure 27. TEM images of approximately 11.6-23.5 nm diameter gold nanoparticles at different magnifications. Image analysis demonstrated a narrow particle size distribution.

UV-Vis spectroscopy is equally useful for determining plasmonic nanoparticle characteristics. Plasmonic nanoparticles, including colloidal gold, exhibit characteristic surface-plasmon resonance (SPR) emissions as a function of size. Surface-plasmon resonance involves resonant oscillation of conduction electrons on the outer surface of the nanoparticle when excited by visible or near-visible light. On the macroscopic level, this is manifested in different colors of nanoparticle solutions as a function of nanoparticle size. As an example, solutions containing nanoparticles of different sized distributions are shown in Fig. 28; note the differences in colors for each solution. These samples are the same as presented in Fig. 25.

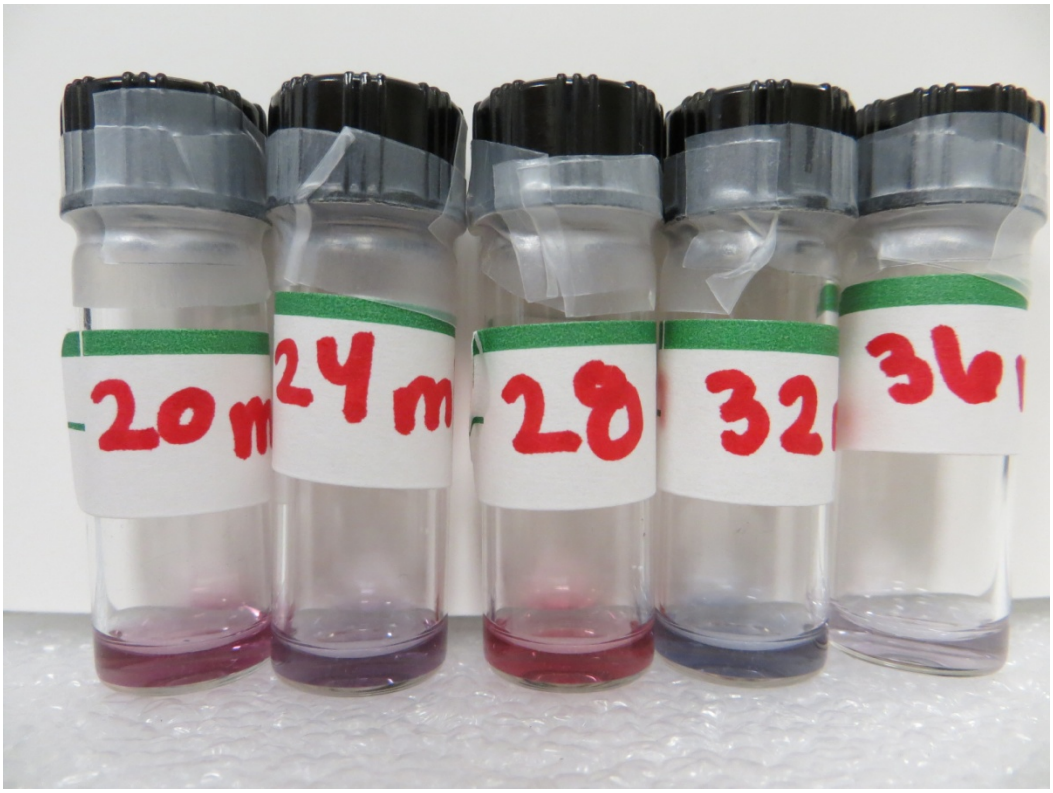

Figure 28. Nanoparticle solutions are shown of various sizes. Numbers on vials correlate to mM concentration of sodium citrate used in the formation reaction.

At an analytical level, UV-Vis absorbance has been shown to be dependent upon both nanoparticle size and concentration (Haiss et al. 2007, Amendola and Meneghetti 2009). Typically, the peak in light absorption, or SPR-peak, as a function of wavelength is dependent upon nanoparticle diameter. In addition, the relative magnitude and width of the SPR-peak provides information about concentration and the size distribution. Peak characteristics have also been shown to provide quantification of protein labelling and degree of conjugation (Kumar et al. 2008, Hamoui 2015). A miniaturized UV-Vis spectrometer, the NanoDrop 2000C (ThermoFisher Scientific, 168 Third Ave., Waltham,

MA 02451) was used in conjunction with commercially produced gold nanoparticle standards (Cytodiagnostics, 919 Fraser Drive Unit 11, Burlinton, ON, L7L 4X8, Canada) to develop an algorithm for determining nanoparticle size and concentration. These standards were supplied with NIST traceable certificates for nominal size and concentration. Particle sizes were verified with TEM image analysis. UV-Vis spectra, showing absorption peaks as a function of nanoparticle size, are shown in Fig. 29. Absorption peaks are shown as a function of nanoparticle diameter in Fig. 30. It is important to note that there is a red-shift of 3-5 nm in these values for nanoparticles following PEGylation and/or protein conjugation, as the added layer of material affects the surface refractive propertied (Kumar et al. 2008).

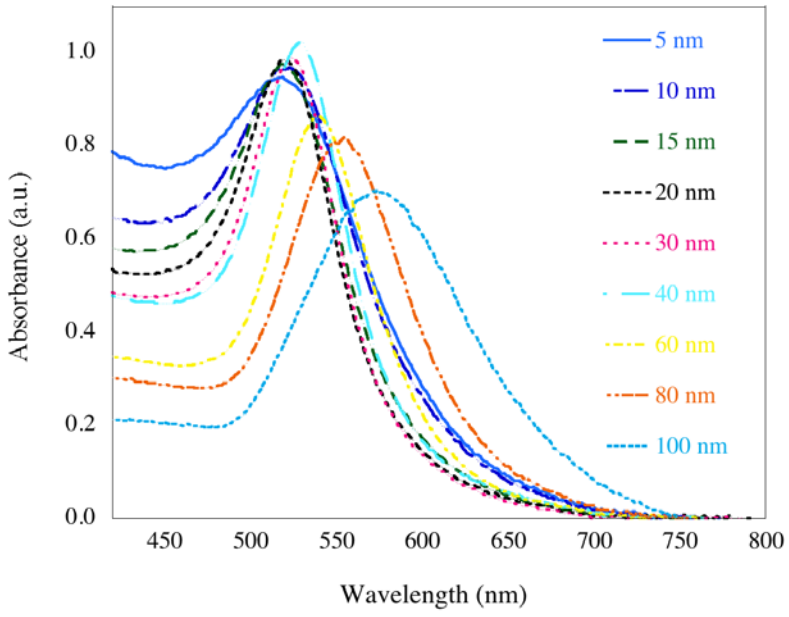

Figure 29. UV-Vis absorbance as a function wavelength (nm) for different AuNP standards of 5, 10, 15, 20, 30, 40, 60, 80 and 100 nm in diameter.

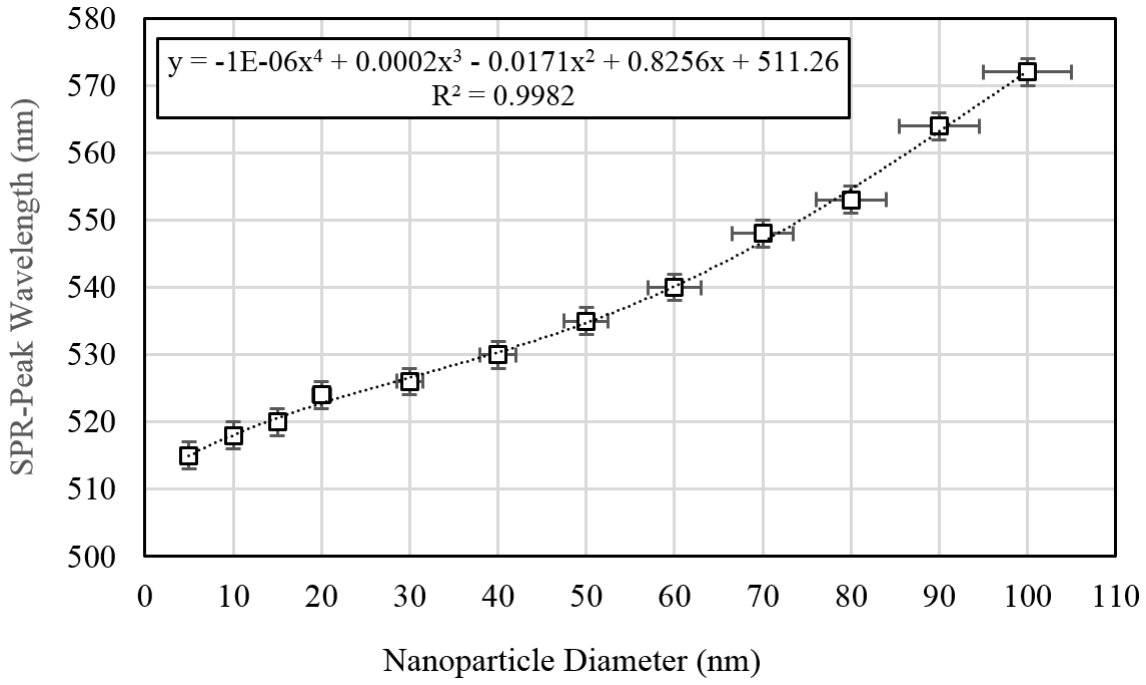

Figure 30. Characteristic SPR-Peak wavelength is shown as a function of nanoparticle diameter. Nanoparticle standards of 5, 10, 15, 20, 30, 40, 60, 80 and 100 nm were verified by TEM image analysis.

The molar concentration of gold nanoparticles for a given nominal diameter was calculated using the Beer-Lambert law expressed as $A = \varepsilon bC$, where ε is the extinction coefficient (M cm^{-1}), b is the path length (cm), and C is the molar concertation (M), and A is the absorbance peak (a.u.). The extinction coefficients, ε, were determined using UV-Vis spectroscopy for different particle sizes and surface ligands (Liu et al. 2007). The surface ligand in our case is trisodium citrate and the path length of the NanoDrop 2000C spectrophotometer is set at b = 1 cm. These data are presented in Fig. 31.

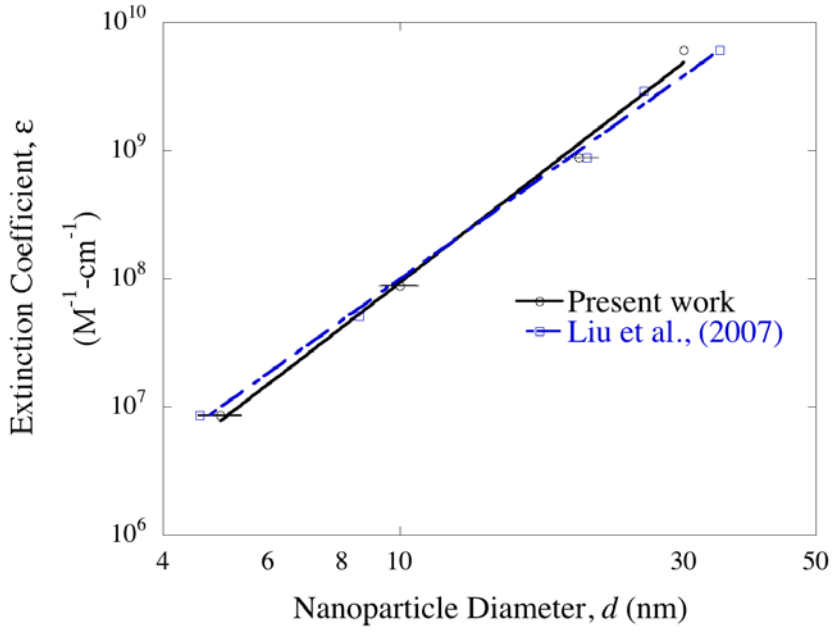

Figure 31. Extinction coefficient, ε, as a function of nanoparticle diameter, *d*, estimated by Liu et al., and those calculated using the standards.

When considering nanoparticles used *in vitro* and *in vivo*, the hydrodynamic diameter of the particles affects circulation, retention, and cellular uptake (Kumar et al. 2008, Jokerst et al. 2010). Hydrodynamic diameter represents the external diameter of the nanoparticle complex. Dynamic Light Scattering (DLS) is typically used to characterize this property, however, this instrumentation was not available. Hydrodynamic diameter was estimated based on similar procedures and results shown in the literature (Kumar et al. 2008, Chattopadhyay et al. 2010, Ting et al. 2010, Jokerst et al. 2011, Kim et al. 2011).

2.6 Radiological Safety

The wide range of situations involved in radionuclide production, radiopharmaceutical manufacturing, and *in vitro* experimentation present a diverse set of processes that must be performed safely. This is especially true in a university setting, where relatively untrained undergraduate students may be involved in the process, as well as graduate students and professionals (Martin and Akabani 2012). Experimentation using radioactive material *in vitro* is widely practiced, so will not be covered in detail herein. The focus will primarily be on radiological safety aspects during cyclotron production, and post-production processing.

2.6.1 Cyclotron and Radiochemistry Facility

Cyclotron facilities present many radiological hazards (IAEA 2009b). Of obvious concern is the intense gamma and neutron radiation fields produced when the cyclotron is operating. However, this hazard is largely mitigated through a series of radiation detectors, interlocks, and engineering and administrative controls (Zanzonico et al. 2008). Of equal concern, but somewhat less obvious, is the presence of highly activated targets and cyclotron equipment (Ogata et al. 2011). Again, this is somewhat protected against by radiation monitoring, shielding, and interlocks. The vast majority of activated products, which contribute to intense radiation fields, are short-lived, and decay away with half-lives on the order of seconds or minutes (Martin and Akabani 2012). Common examples

include ^{28}Al ($T_{1/2}$ = 2.414 min) and ^{55}Cr ($T_{1/2}$ = 3.497 min). Shielding in the laboratory during recovery, well-practiced procedures, efficient workflow, and other considerations are critical for radiological safety in the radiochemical facility.

2.6.1.1 Cyclotron Radiation and Activation Products

In previous research, estimations of the amount and type of activation products, and their impact on exposure rate, were analyzed for the ^{209}Bi (α, 2n) ^{211}At reaction (Martin and Akabani unpublished data 2012, Martin et al. 2014). Briefly, estimated cross sections and outgoing particle spectra were calculated for all open reaction channels produced by ^{209}Bi (α, X) reactions using the code TALYS (Koning et al. 2008). In order to approximate the total neutron production within a thick target, calculations were performed with alpha particle energies spanning the range of 0.001 MeV to 28 MeV. Many of the reaction channels resulted in negligible cross sections when compared to the primary reactions (α, 2n), (α, α'), (α, n), and (α, nα), listed in order of decreasing total yield. The neutron yield, angular dependence, and normalized differential cross sections produced by these data, Figs. (32-34), were used to create an input file for the transport code MCNPX (Martin et al. 2014).

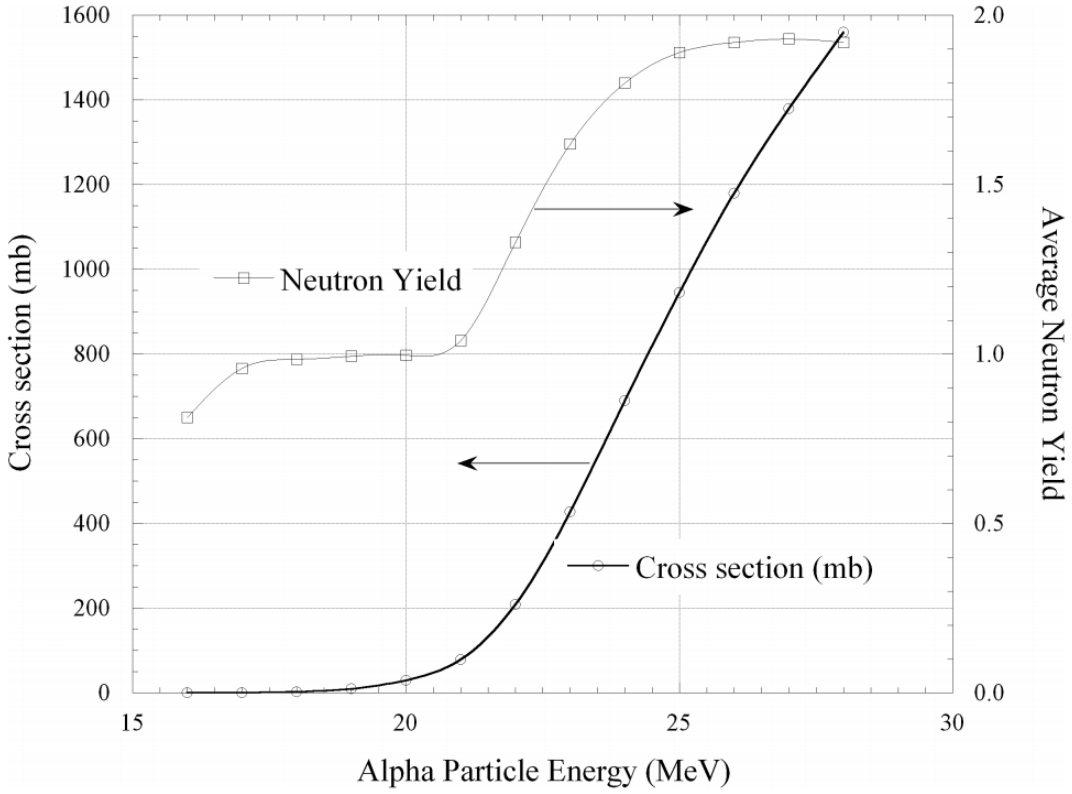

Figure 32. The total neutron production cross section and average neutron yield for the ^{209}Bi (α, xn) reaction are shown as a function of incident alpha particle energy. Reprinted with permission from (Martin et al. 2014).

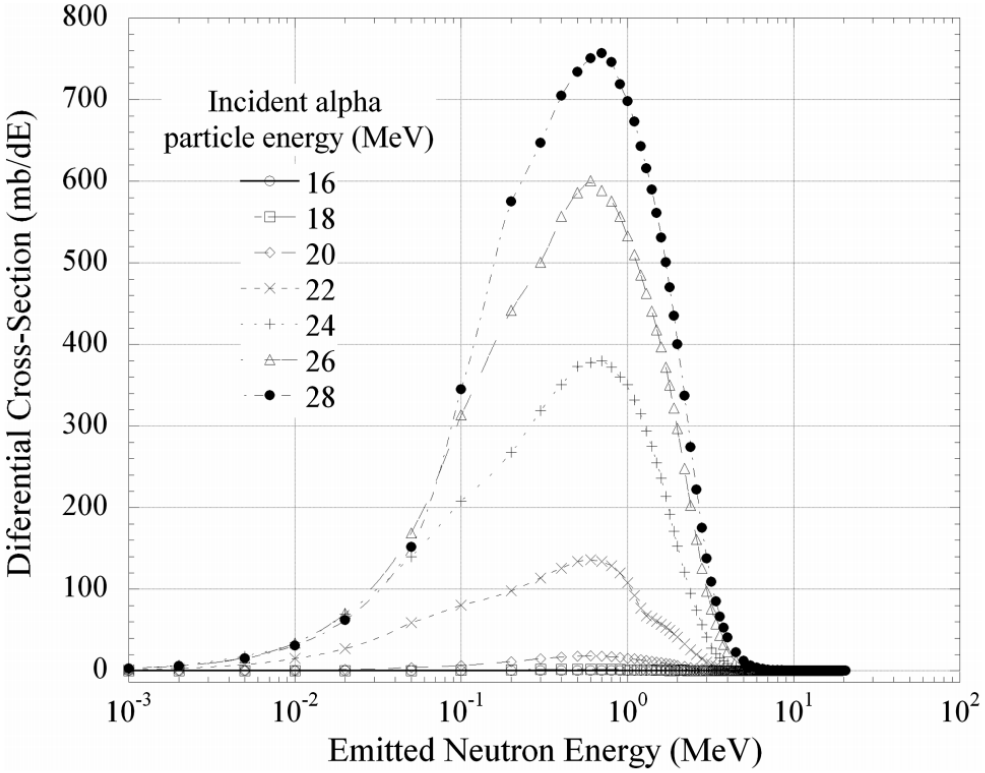

Figure 33. The differential cross section for neutron production is shown as a function of incident alpha particle energy on a ^{209}Bi target. Reprinted with permission from (Martin et al. 2014).

Activation analysis and dose rate analysis was performed using MCNPX (Pelowitz 2008). This analysis was carried out on a representative target, as well as arbitrary blocks of common material found in the cyclotron facility, including stainless steel, aluminum, and concrete. Activation product mass concentration was estimated with these data, and applied to known equipment of interest within the target area. The neutron beam is strongly biased towards the forward direction, as a function of energy (e.g., higher energy incident alpha particles result in a higher magnitude of forward bias). Because of this, it is

expected that the majority of the activation occurs in a small cone shaped area, in-line with the ion beam. Scattered and moderated neutrons throughout the rest of the facility were neglected in this analysis, as this is commonly encountered during normal cyclotron operation. Neutron dose was calculated using the flux-to-dose conversion factors provided by the International Commission on Radiation Units and Measurements (ICRU) Report 57, and was generally found to be negligible outside the cyclotron vault (ICRU 1998).

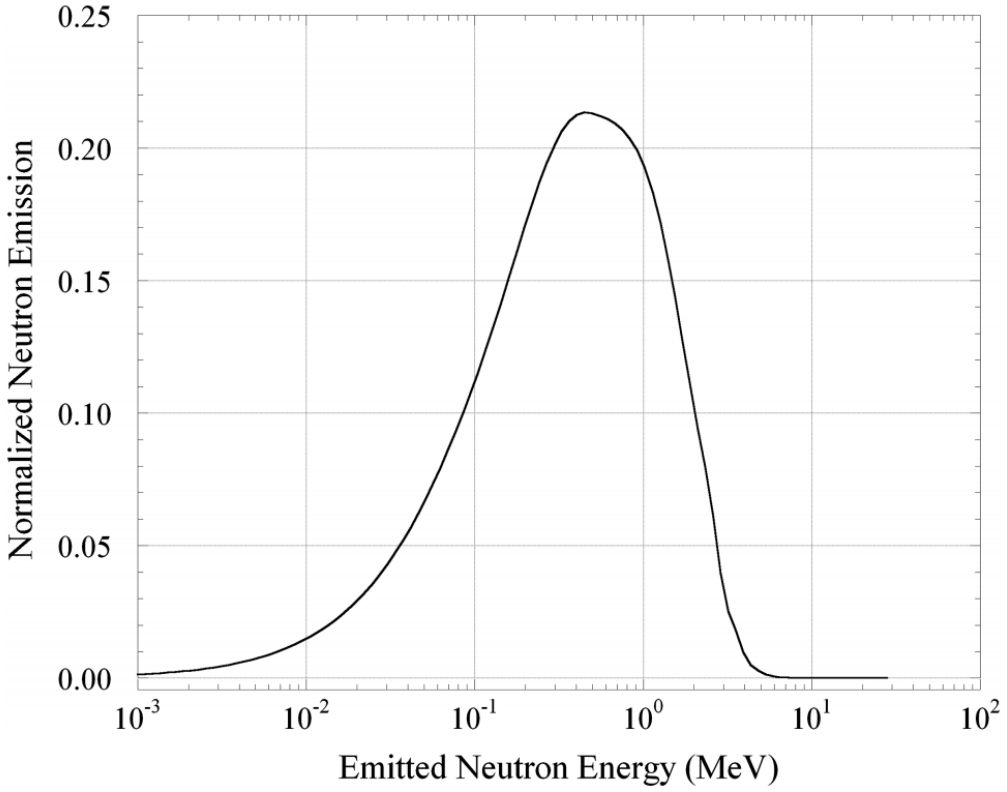

Figure 34. The normalized neutron energy spectrum is shown for the ^{209}Bi (α, xn) reaction. Reprinted with permission from (Martin et al. 2014).

Table 9 provides estimated yields of all significantly produced radionuclides, excluding radionuclides produced heavy charged particle interactions from the primary beam. Produced yields are given in terms of specific activity per integrated current. As can be seen, most activities are insignificant when compared to ^{24}Na, ^{28}Al, ^{55}Cr, and ^{211}At.

Table 9. Calculated yields of significant radionuclide activation products as estimated using MCNPX.

Radionuclide	**Half-life**	**Specific Activity per Incident Particle** **(Bq α^{-1} kg^{-1})**	**Specific Activity per Integrated Current** **(Bq μA_p^{-1} h^{-1} kg^{-1})**	**Primary Activated Material**
^{211}At	7.214 h	2.89×10^{-7}	6.92×10^{9}	Target
^{28}Al	2.414 min	1.15×10^{-10}	2.75×10^{6}	Target holder, instrumentation
^{51}Cr	27.70 d	1.47×10^{-16}	3.31×10^{0}	Beam pipe, structural supports
^{55}Cr	3.497 min	7.84×10^{-13}	1.76×10^{4}	
^{56}Mn	2.579 h	2.38×10^{-14}	5.35×10^{2}	
^{55}Fe	2.730 y	4.89×10^{-18}	1.10×10^{-1}	
^{59}Fe	44.50 d	1.33×10^{-17}	2.99×10^{-1}	
^{24}Na	14.96 h	9.54×10^{-16}	2.14×10^{1}	Concrete structure, shielding, wall plugs, etc.
^{27}Mg	9.458 m	7.90×10^{-16}	1.77×10^{1}	
^{49}Ca	8.718 m	1.60×10^{-17}	3.59×10^{-1}	
^{51}Ti	5.760 m	3.71×10^{-16}	8.34×10^{0}	

Following the end of irradiation of the target, it is customary to allow a so-called "cooling time" on the order of 15-30 minutes to allow the intense, short-lived activation products decay. The dose received by a worker, especially when a target must be manually manipulated, is significantly reduced by this brief waiting period (Zanzonico et al. 2008, Martin and Akabani 2012).

2.6.1.2 Radiochemistry Facility

It is important to incorporate standard safety considerations into the radiochemistry facility design. Shielding of waste containers and work areas, air handling and monitoring (discussed in the next section), access control to restricted areas, and proper equipment for reducing direct manipulation of the target or product are essential (IAEA 2009b).

The IRBRB has incorporated a shielded hot cell, two shielded chemical enclosures, and a shielded fume hood to provide adequate protection to personnel during recovery (Von Gahlen International Inc., P.O. Box 1550, Chatsworth GA 30705). The dual chemical enclosures and hot cell, equipped with remote manipulator arms, are designed with 3-inch lead shielding and are suitable for high-level production of positron emitting radionuclides. A view of the hot cell is provided in Fig. 35. While this level of shielding is overly protective for the low gamma emissions of ^{211}At, an end goal of the IRBRB is to pursue production of positron-emitting radionuclides, such as ^{64}Cu and ^{62}Zn/^{62}Cu, for

research in PET imaging and theranostics. However, the filtered ventilation provided by these units is ideal in preventing facility contamination via airborne alpha emitters, as produced in this study. The dual chemical enclosures, while not in use for processing, are currently configured to hold calibration sources, thereby reducing their influence on background, as well as holding high-dose-rate waste, such as the target backing and other activated components.

The shielded fume hood, actually a biological safety cabinet (BSC), shown in Fig. 16 and Fig. 36, provides 1.5-inch lead shielding on the sides, bottom, and rear of the device. An additional sliding shield, with 1.5-inch equivalent leaded glass, is used to provide shielding to the front of the worker. The fume hood is designed exclusively for use with the furnace and equipment dedicated to ^{211}At production. Filtration by high efficiency particulate air (HEPA) filters and activated carbon is provided to capture and release of radioactivity. Extensive shielding is not necessary for the astatine itself, but is beneficial for reducing the dose rate due to activated ^{28}Al in the target backing plate during distillation.

Figure 35. The hot cell, featuring remote manipulator arms, is shown. Note the control (lower right) for the dose calibrator (inside). Doors to the dual chemical enclosures are just visible to the left of the image.

Figure 36. The fume hood with movable front shield is shown. Detection and assay equipment are visible to the left of frame.

Workflow and other considerations can also lead to decreased dose to the worker. For example, removal of the bismuth/astatine matrix from the aluminum target backing for distillation not only decreases the distillation time, but also allows the activated aluminum to be placed in a shielded container. Performing preliminary steps prior to elution or astatination also reduces absorbed dose to both the user, as well as equipment. While chemistry module components are mostly made of radiation resistant materials, such as PEEK, long-term exposure will cause a degradation of materials (Anaheim et al. 2015a).

2.6.2 Air Handling and Facility Air Monitoring

Air handling and air quality play an important role in meeting standards for compliance in sterility and purity. In general, radiopharmaceuticals, especially immunoconjugates, cannot be heat sterilized prior to patient administration. This places a high importance on aseptic procedures and equipment (IAEA 2009c). Additionally, the establishment of a clean room environment is necessary for meeting future cGMP and USP requirements (US FDA 2009). With this in mind, the radiochemistry room of the IRPRP was designed and tested to as-built ISO Class 7 cleanroom standards as per the ISO 14644-1 classification system. These standards dictate particulate size and concentration standards, as detailed in Table 10. A schematic of the room is shown in Fig. 37.

To fulfill the as-built Class 7 standards, several system components are incorporated. These segments include air inlet and exhaust, differential room pressure, anteroom design, and non-permeable surfaces. At-rest and operational standards will require additional training on gowning and disinfecting procedures.

Conditioned inlet air is passed through several HEPA filters in parallel to both purify the incoming air and meet minimum volumetric exchange rates. Air intake occurs at the ceiling, and is exhausted by ducts near floor level. In this particular installation, room exhaust is also provided by continuous flow through a laminar flow hood or biological safety cabinet.

Table 10. Limits on particle concentration as a function of aerodynamic diameter are given for as-built ISO clean room standards.

ISO Class	Particulate Concentration by Aerodynamic Diameter, m^{-3}					
	5 µm	**1 µm**	**0.5 µm**	**0.3 µm**	**0.2 µm**	**0.1 µm**
ISO 1	--	--	--	--	2.37×10^{0}	1.0×10^{1}
ISO 2	--	--	3.52×10^{0}	1.02×10^{1}	2.37×10^{1}	1.0×10^{2}
ISO 3 (1)*	--	8.32×10^{0}	3.52×10^{1}	1.02×10^{2}	2.37×10^{2}	1.0×10^{3}
ISO 4 (10)*	--	8.32×10^{1}	3.52×10^{2}	1.02×10^{3}	2.37×10^{3}	1.0×10^{4}
ISO 5 (100)*	2.93×10^{1}	8.32×10^{2}	3.52×10^{3}	1.02×10^{4}	2.37×10^{4}	1.0×10^{5}
ISO 6 (1000)*	2.93×10^{2}	8.32×10^{3}	3.52×10^{4}	1.02×10^{5}	2.37×10^{5}	1.0×10^{6}
ISO 7 (10000)*	2.93×10^{3}	8.32×10^{4}	3.52×10^{5}	--	--	--
ISO 8	2.93×10^{4}	8.32×10^{5}	3.52×10^{6}	--	--	--
ISO 9	2.93×10^{5}	8.32×10^{6}	3.52×10^{7}	--	--	--

* Numbers in parentheses represent the approximate Class as defined by US Federal Standard 209E

Product open to the atmosphere must be manipulated within an ISO Class 5 environment. In the IRPRP installation, the shielded BSC and a specially filtrated hot cell and chemistry module enclosure meet this standard. The BSC is a commonly available unit from Labconco, which has been modified by the shielding vendor Von Gahlen. The Universal Hot Cell and Dual Chemical Enclosure modules are also provided by Von Gahlen. Inlet and exit HEPA filtration is provided in both units. The hot cell and chemistry module enclosure also contains an activated charcoal filter canister for exhaust scrubbing. The BSC and clean room exhaust pass through a large activated charcoal filter on the roof

of the facility prior to final exhaust. The HEPA exhaust filters are provided to remove radioactive particulates entrained in the exhaust, while the activated charcoal provides filtration of vapors.

An anteroom is provided for several purposes. Primarily, the anteroom acts as a barrier between the clean room and the unclassified space, as detailed below. Additionally, the anteroom provides a convenient location for gowning, a step-off pad, hand-and-foot contamination monitors, as well as storage of PPE when not in use.

Air quality is preserved by maintaining pressure differentials between rooms. Standard guidance is to maintain the clean room at a positive relative pressure, such that no contamination enters the room via penetrations or door openings. However, the IRPRP radiochemistry room is located in a facility that sees a large amount of research in others and has a correspondingly large traffic of cyclotron personnel, faculty, and students. The Radiological Safety Staff at Cyclotron Institute therefore required the room to be at negative pressure relative to the remainder of the facility, such that any airborne contamination would remain isolated in the IRPRP.

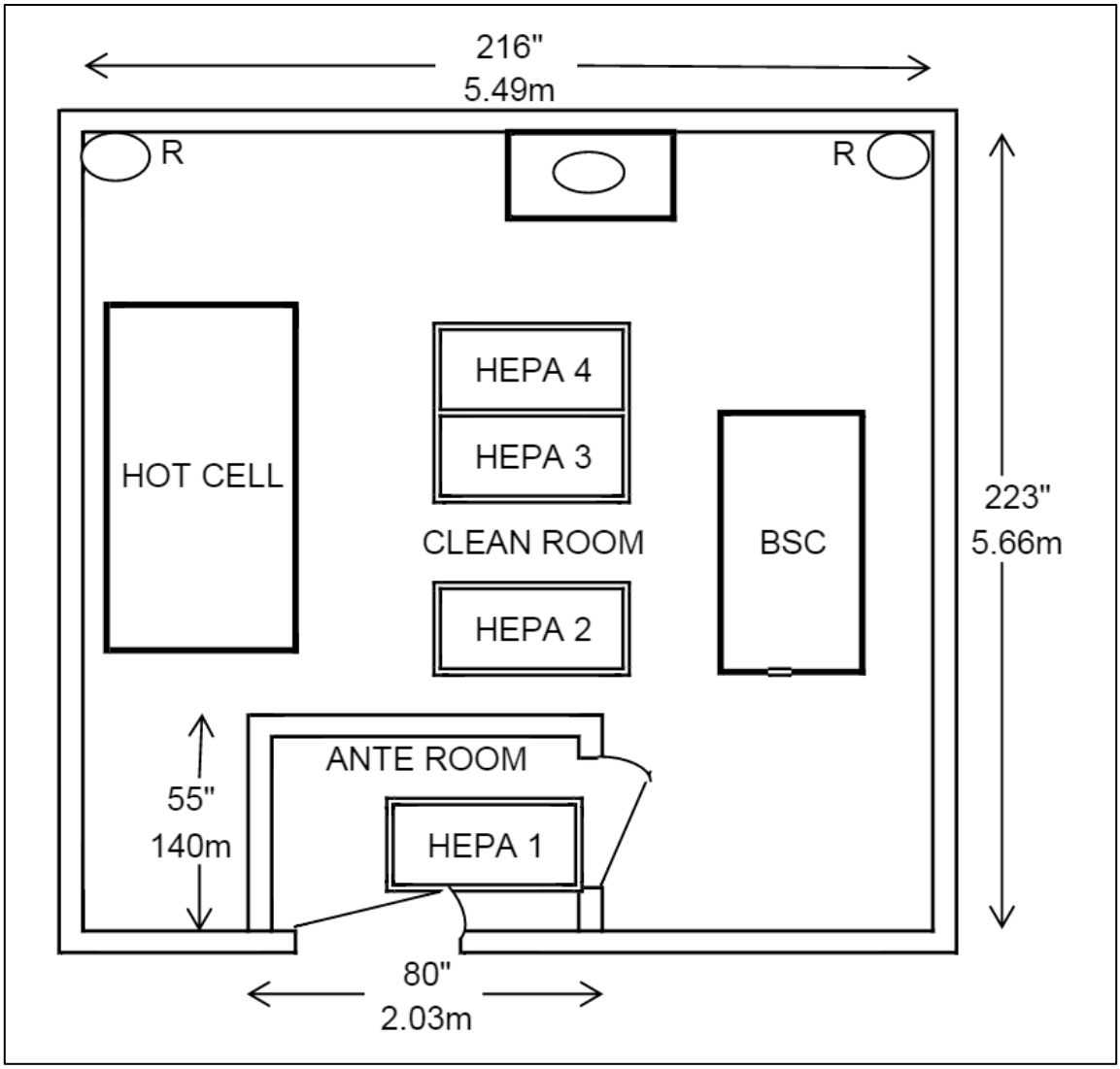

Figure 37. A schematic of the radiochemistry room floor plan is provided, showing locations of conditioned air inlet through HEPA filters, floor level return ducts (R), and approximate location of the hot cell and biological safety cabinet (BSC).

Facility effluent air monitoring in place at the Texas A&M Cyclotron Institute is optimized for the entire facility, and is not conducive to detecting alpha emitting radionuclides. Due to the potential of airborne release, based upon the volatility of astatine,

as well as the dry distillation operation, dedicated area monitoring and effluent monitoring equipment were installed in the IRPRP radiochemistry facility. Area radiation monitoring for gamma and x-ray radiation is provided by a Canberra G64 Area Gamma Monitor (Canberra Inc., 800 Research Pkwy, Meriden CT 06450). This unit consists of a solid state detector, and incorporates building power and is connected to the cyclotron control room alarm system. Air effluent monitoring is provided by a Canberra iCAM Alpha/Beta Air Monitor. Air exhaust from the hot cell and BSC are routed through the detector. Air is drawn through the device by a vacuum pump. Any airborne particulates are deposited onto removable filter material, which is changed monthly, or after every processing experiment. The filter is monitored on-line via a passivated implanted-ion planar silicon (PIPS) detector, which provides counts in separate alpha and beta channels. As with the G64, this unit is tied into building power, as well as the building alarm control panel. Additionally, logic circuits and automatic controls are driven by the iCAM. Air inlets to the room, exhaust fans, dampers, and a roof mounted blower are all controlled by the automated logic. In the event of an airborne release, the iCAM is programmed to provide an alarm over a specified threshold count level. This will drive the logic system to maintain negative pressure in the radiochemistry laboratory to contain the airborne release. The system will also minimize exhaust, and route the remaining exhaust through a large volume activated charcoal filter on the roof of the facility, preventing the release of the airborne contaminant to a public area. The G64 and iCam are shown in Fig. 38. Also visible are some of the logic controllers and sensors used to control the airflow state.

Figure 38. The facility radiation monitors are shown. On the left is the iCAM model continuous particulate air monitor. On the right is the G64 model area gamma alarm.

3. RESULTS

A series of five individual experiments were conducted to produce ^{211}At. Extended (8+ h) overnight irradiations of 29 MeV (7.25 MeV u^{-1}) alpha particles at currents up to 7 μA_e were performed with satisfactory results. Production yields ranged between 10.73 – 39.17 MBq μA_p^{-1} h^{-1}, consistent with published yields, at average beam intensities on the order of 5-10 times that used in previous experiments (2-3 μA_p). Recovered yields were on the order of 20 mCi per production run after initial development (median 22.09 mCi ± 0.77). No contamination by ^{210}At or ^{210}Po was detected in any of the recovered product, however, ^{135}I contamination was suspected prior to distillation in two samples. The total time involved for each experiment, including irradiation and post-processing, ranged from 18-24 hours. Irradiations were performed overnight on weekdays, such that a full complement of health physicist and cyclotron personnel would be available to help during the distillation and recovery phase of experimentation.

Beam development was performed by experienced Cyclotron Institute staff, using a phosphor plate. While it is preferable to tune the beam and then irradiate a piece of radiographic film placed on the target holder, this option was not available due to the lack of a nearby vacuum isolation valve. The nearest isolation valve isolated approximately thirty linear feet of beam line, the target enclosure, and the volume involving a large bending magnet leading to other experiment ports. The time involved in purging, and then pulling down the pressure on this large volume made beam characterization impractical. However, a phosphor plate was used to roughly position the beam and adjust focusing.

Upon irradiation, the target and target backing phosphoresced and the beam spot was visible on a black and white CCD camera closed circuit television image. This camera was used to validate beam placement and size, as well as to monitor the target for physical signs of melting and deformation during all experiments.

The initial experiment was used as a proof of production. A water chiller was not available during this run, and the maximum current was therefore limited. Distillation did not occur for this first experiment. A water chiller operating at 4 °C and 1.5 L min^{-1} flow rate was used to cool the target on all other production runs. Thermocouple measurements at the target holder showed a steady state temperature of 11 °C, prior to irradiation, which was consistent from across all experiments. Temperature was not measured on-line, as remote connections for the thermocouple were not available. Table 11 shows a comparison of the produced yields from these experiments, compared to published results (cf Table 4). A summary of the produced yield, decay corrected to EOB, is provided in Table 12. Also shown is the total product activity of ^{211}At for each run. Table 13 shows the decay corrected distillation yields for each experiment, in terms of *RCP* and *RCY*, as well as a comparison to published data. Detailed results of each experiment are given individually in the following paragraphs. Unless otherwise stated, errors are quoted as standard error, and activities are decay corrected to EOB.

Table 11. Produced yields are shown for these experiments, compared to published results.

^{211}At Yield EOB ($MBq\ \mu A_p^{-1}\ h^{-1}$)	Experimental	Published
Minimum	10.7	4
Maximum	39.2	48
Median	27.5	12.4

Table 12. Yields and EOB activities are shown for the experimental production runs.

Exp. No.	^{211}At Yield EOB ($MBq\ \mu A_p^{-1}\ h^{-1}$)	^{211}At Activity EOB (MBq)	^{211}At Activity EOB (mCi)	*RCY* (%)
Exp. 1	--	--	--	--
Exp. 2	10.7 ± 0.101	11.71 ± 3.4	0.316 ± 0.094	21.13 ± 29.05
Exp. 3	39.2 ± 0.103	817.5 ± 80.2	22.09 ± 2.17	55.79 ± 17.68
Exp. 4	29.0 ± 0.100	847.6 ± 35.4	22.91 ± 0.96	50.63 ± 1.17
Exp. 5	26.0 ± 0.102	790.5 ± 21.8	21.36 ± 0.59	62.00 ± 3.08
Median	27.5 ± 0.203	804.0 ± 90.4	21.72 ± 2.45	53.21 ± 34.17

Table 13. Radiochemical yield data for each experiment is compared to published *RCP* and *RCY* values.

Experiment	*RCP* (%)	*RCY* (%)
#1	--	--
#2	99.999 ± 6.036	21.128 ± 29.049
#3	99.964 ± 2.672	55.8 ± 9.81
#4	99.980 ± 0.024	50.63 ± 1.17
#5	99.992 ± 3.157	62.00 ± 3.08
Groppi et al. 2005	99.96+	60-80
Hadley et al. 1991	98+	30 ± 18.9
Yordanov et al. 2001	--	60
Schwarz et al. 1998	--	68

3.1 Experiment 1

Experiment 1 was performed as a preliminary test experiment. The new target system, as seen in Fig. 9, had not been used prior to this experiment. Additionally, the K-150 cyclotron had not been used in any ^{211}At production experiments, and the water chiller was not available due to scheduling conflicts. Finally, this experiment was before implementation of the clamping system used to hold the target backing to the target holder. Because of this, the maximum allowable beam current on target was severely limited. An initial beam of 28.88 MeV (7.22 MeV u^{-1}) and 2.1 μA_e was used to bombard the target.

The bismuth showed signs of melting within 2 minutes. A faraday cage was placed while the current was adjusted to 0.4 μA_e. A short amount of time (2 min) was given for the target to cool, followed by irradiation at 0.4 μA_e. for 37 minutes. The target again showed signs of melting, so the beam current was reduced to 0.2 μA_e. The target was irradiated for an additional 9 hours and 20 minutes, giving a total integrated current of approximately 1.09 μA_p-hr. After a 30-minute cool down time, dose rate measurements were taken using an ion chamber (Fluke 451P). The target, in the holder, measured approximately 5 mR hr^{-1} on contact with the vacuum enclosure. A picture of the beam line entering the vacuum enclosure is given in Fig. 39. A view from the top of the vacuum enclosure, looking down onto the target face, is shown in Fig. 40. This target was allowed to decay and was not processed in the radiochemistry facility.

Figure 39. A view of the target vacuum enclosure. The beam line enters from the left. Note the shield wall to the right. The target is accessed by removing the screws and side plate facing the camera.

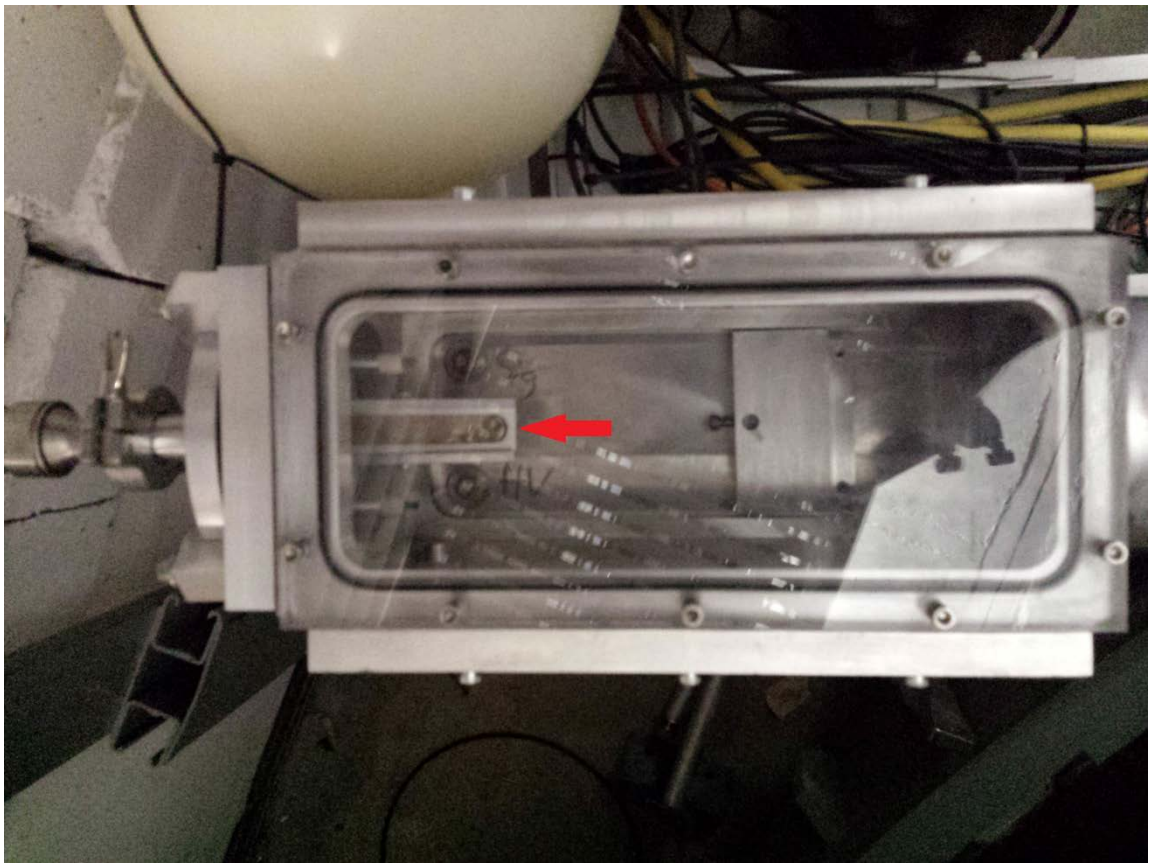

Figure 40. A view from the top of the vacuum enclosure, looking down on the target, located by the red arrow. The beam enters from the right.

3.2 Experiment 2

Experiment 2 was conducted utilizing the water chiller and new style clamps during irradiation. The pyramidal indentions in the target backing were not incorporated, and thermal grease was not used. A picture of the target prior to irradiation is shown in Fig. 41, highlighting the new clamping system.

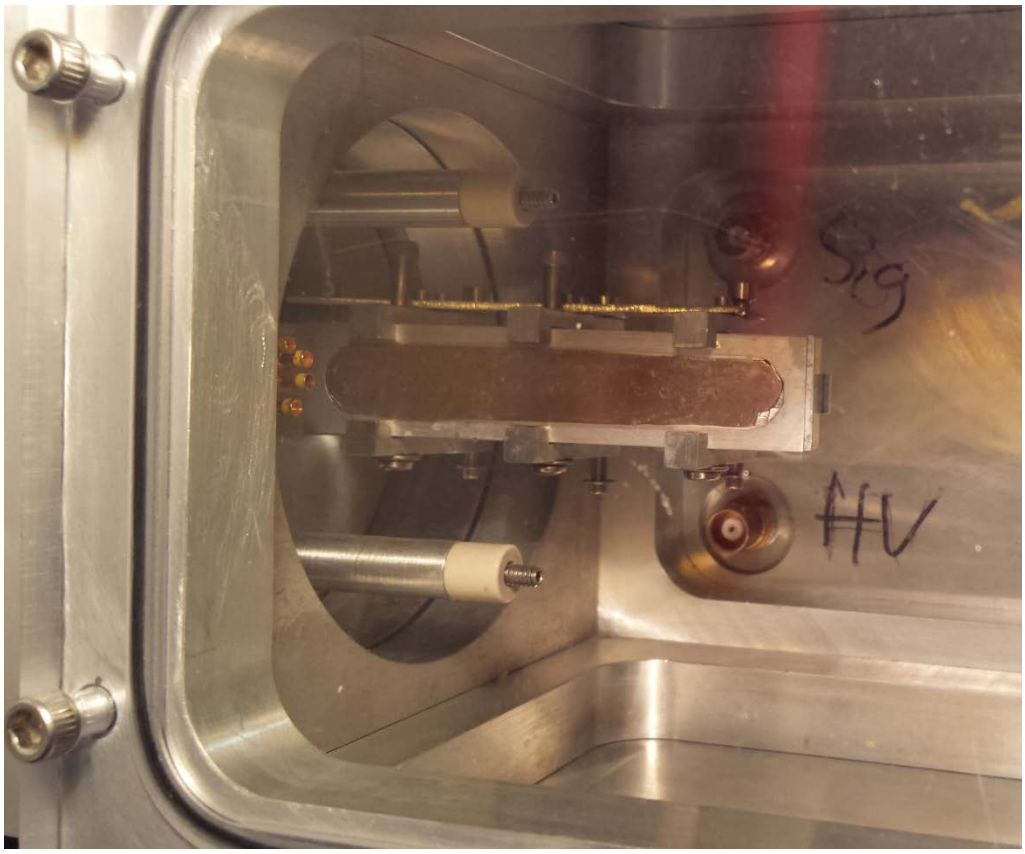

Figure 41. The new target clamping system is shown. BNC connectors visible behind the target are for beam tuning instrumentation.

Beam current during Experiment 2 was periodically increased in an effort to determine the maximum allowable current. The water chiller was used to bring the target to a steady state temperature of 11 °C before irradiation. Temperature was not measured during irradiation. Beam energy was the same as Experiment 1: 28.88 MeV (7.22 MeV u^{-1}). Beam current on target as a function of time is provided in Table 14. The total integrated current for Experiment 2 was approximately 4.78 μA_p-hr, better than four times that in Experiment 1.

Table 14. Beam current as a function of time is tabulated for Experiment 2.

Time on Target (hh:mm)	Beam Current (μA_e)	Notes
00:00	0.37	
00:03	--	Ion gauge malfunctioned. Vault opened to reset.
00:20	0.42	
00:32	0.6	
00:42	0.8	
00:52	1.0	
01:03	1.2	
01:11	1.6	
01:27	2.0	
01:28	--	Beam stopped. Signs of melting.
01:39	1.0	Beam restarted.
10:04	--	EOB

After a 30-minute cooling time, the target was removed and transported to the radiochemistry laboratory for processing. The target was counted by HPGe at the 2 m location, with tabulated yield data shown in Table 15. Difficulties in setting up the distillation apparatus and other factors delayed the onset of distillation by approximately an hour and a half. Several items were noted during this initial recovery work for improvements in timing and efficiency in further experiments. Distillation was begun, with a programmed maximum furnace temperature of 700 °C. Target temperature

increased, as measured with an infrared thermometer, and the furnace temperature was reset to 650 °C. After 42 minutes at this temperature, the furnace was ramped back to 700 °C, as it was noted that bismuth in the far end of the crucible was not molten. This observation emphasized the need for proper target placement in future experiments. During distillation, activity in the cold trap was measured both by the dose calibrator and with a Geiger-Mueller (G-M) probe located near the cold trap entrance. The dose calibrator did not provide meaningful readings, indicating that the geometry in use was incompatible with this detector. The temperature profile and G-M count rate are shown as a function of time in Fig. 42.

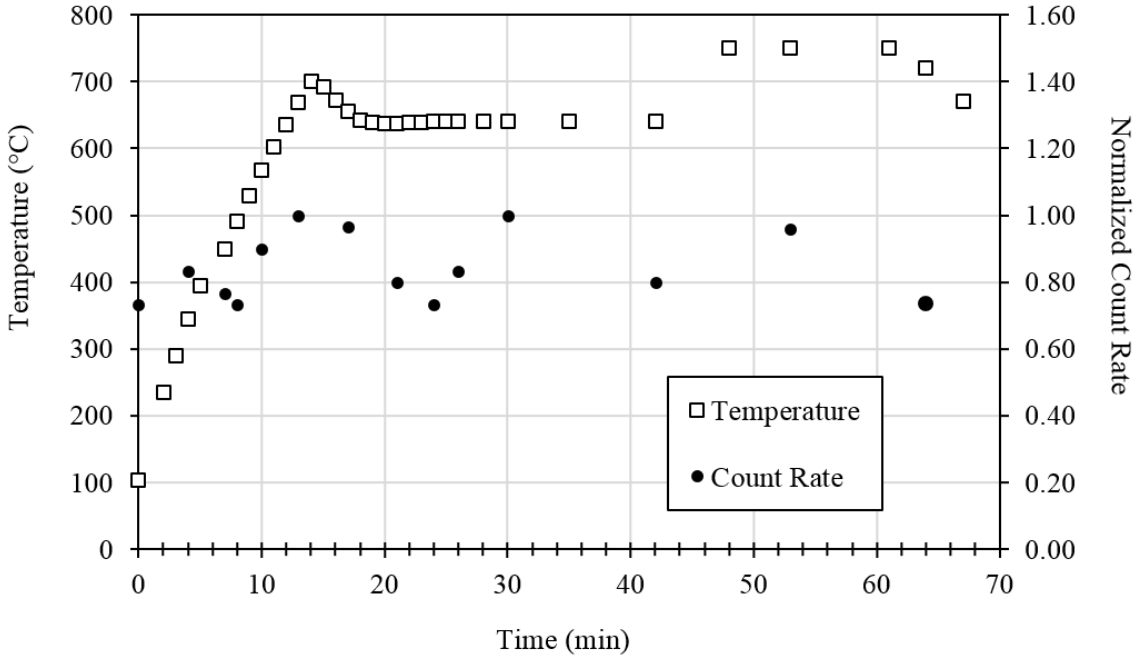

Figure 42. Count rate and furnace temperature data are shown for experiment two during distillation.

At the end of distillation, measurements were made of the charcoal filter, the PEEK tubing in the cold trap, and the target. The amount remaining in each item is tabulated in Table 16. Note that ^{28}Al and other contaminants are likely present in the target, contributing to the measured count rate. It is not clear why a large amount of activity remained in the target. The target and quartz tray used during distillation are shown in Fig. 43. The quartz tray cracked upon cooling, most likely due to uneven contraction. Note that the aluminum target backing appears melted in places, and the entire target is charred. It was decided to increase the furnace temperature for future experiments.

Following distillation, the PEEK capillary was washed twice with 2 mL of sodium citrate solution, and captured in a 5-mL vial. This sample was placed in the 10 cm counting location and counted for 20 minutes. Calculated yields based on spectral data for a two-hour count from the aliquot are presented in Table 17. No contamination by ^{210}At or other radionuclides was detected, although recovered yield was very low.

Table 15. The calculated yields based on spectral data are provided for the target of Experiment 2, prior to distillation.

Radionuclide	*Eγ* (keV)	Net Peak Area (Counts)	Net Peak Uncertainty (%)	Activity (MBq)	Activity (mCi)
^{211}At	687.0	932	4.5	16.5 ± 2.8	0.45 ± 0.077
^{211}Po	569.7	1343	0.3	11.1 ± 1.5	0.30 ± 0.042
	897.8	820	4.4	7.5 ± 1.3	0.21 ± 0.035
Median ^{211}At/^{211}Po				11.71 ± 3.4	0.316 ± 0.094
^{210}At	245.3	--	--	--	--
	1181.4	--	--	--	--
	1436.7	--	--	--	--
	1483.4	--	--	--	--
	1599.5	--	--	--	--

Table 16. Recovered count rate fractions post-distillation for Experiment 2.

Location	Percent Count Rate
Target	92.5
Cold Trap	2.9
Charcoal Filter	4.6

Figure 43. The target/target backing and quartz tray for Experiment 2 are shown after distillation.

Table 17. The calculated yields based on spectral data are provided for the final sample from Experiment 2, decay corrected to EOB.

Radionuclide	*Eγ* (keV)	Net Peak Area (Counts)	Net Peak Uncertainty (%)	Activity (MBq)	Activity (mCi)
^{211}At	687.0	2920	2.1	4.089 ± 0.087	0.1105 ± 0.0023
^{211}Po	569.7	4220	1.7	2.474 ± 0.042	0.0669 ± 0.0011
	897.8	2890	1.9	2.255 ± 0.043	0.0609 ± 0.0012
Median ^{211}At/^{211}Po				2.474 ± 0.106	0.0669 ± 0.0028
Median ^{210}At				--	--
RCP ^{211}At/^{211}Po (%)				99.999 ± 6.036	
RCY ^{211}At/^{211}Po (%)				21.128 ± 29.049	

3.3 Experiment 3

Experiment 3 used the water chiller and new style clamps during irradiation. In addition, the pyramidal indentions in the target backing and thermal grease between the target holder and target backing plate were incorporated. As can be seen in Table 18, these changes allowed for a substantial increase in beam current on the target. Beam energy remained at 28.88 MeV (7.22 MeV u^{-1}), with an approximate total integrated current of 20.87 μA_p-hr.

Similar distillation procedures were followed as in previous experiments. The furnace temperature was preset to 950 °C to ensure full target melting, in an attempt to increase recovery. The target bismuth/astatine matrix was able to be separated from the aluminum target backing plate for distillation. The cold trap arrangement was altered for this distillation. Instead of submersion in liquid nitrogen within the dose calibrator well, a small plastic bucket was used with a mixture of ethanol and dry ice at -72 °C. Larger diameter coils of the capillary tubing were submerged in this bath, with a G-M detector placed next to the bucket. Count rate data from the G-M detector and target temperature data are provided as a function of time in Fig. 44.

Table 18. Beam current as a function of time is tabulated for Experiment 3.

Time on Target (hh:mm)	Beam Current (μA_e)	Notes
00:00	1.00	
00:09	1.50	
00:20	1.75	
00:30	2.0	
00:40	2.30	
00:55	2.50	
01:06	2.80	
01:11	3.10	
01:16	3.50	
01:21	3.75	
01:26	4.00	
01:33	4.50	
01:38	5.00	
01:43	5.50	Vault neutron monitor at 2146 mR hr^{-1}
01:50	5.00	Reduced to 5.0 μA_e for overnight. 2129 mR hr^{-1}
05:20	5.00	Noticed wandering in current. Reset to 5.0 μA_e.
09:10	0.00	EOB

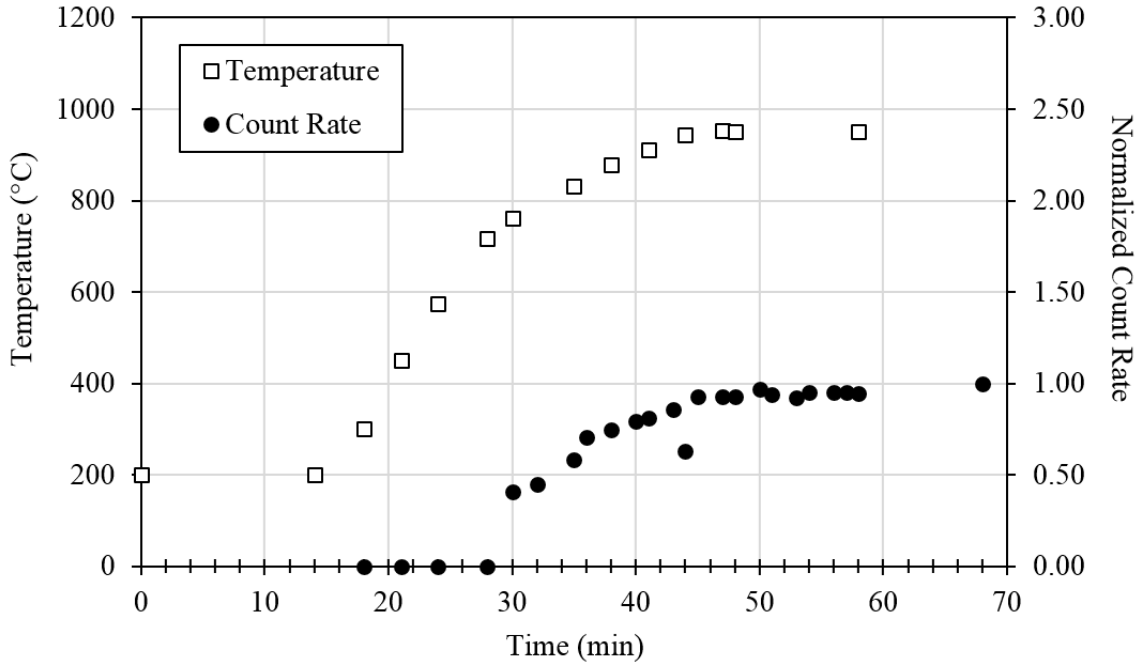

Figure 44. Count rate and furnace temperature data are shown for experiment three during distillation.

A background corrected spectrum of the target and target backing prior to distillation is shown in Fig. 45. As can be seen, there are impurities present. The lines present at 511 keV and 1275 keV indicate that one contaminant is ^{22}Na ($T_{1/2}$ = 2.602 y, y_{511} = 1.81, $y_{1273.6}$ = 0.99), likely a contaminant from the aluminum backing plate or activation of a component of the thermal grease. However, the relative number of counts between the ^{22}Na photopeaks do not correlate to the published yields. Therefore it is likely that annihilation radiation from another source is also present. Other impurity gamma lines at approximately 1039 keV and 1368 keV could likely correspond to ^{135}I ($T_{1/2}$ = 6.57 hr, $y_{1038.8}$ = 0.08, $y_{1367.9}$ = 0.06). The source for this radionuclide is unclear, but likely comes

from activation of the thermal grease. Initial target yields for products are shown in Table 19, with impurity yields shown in Table 20.

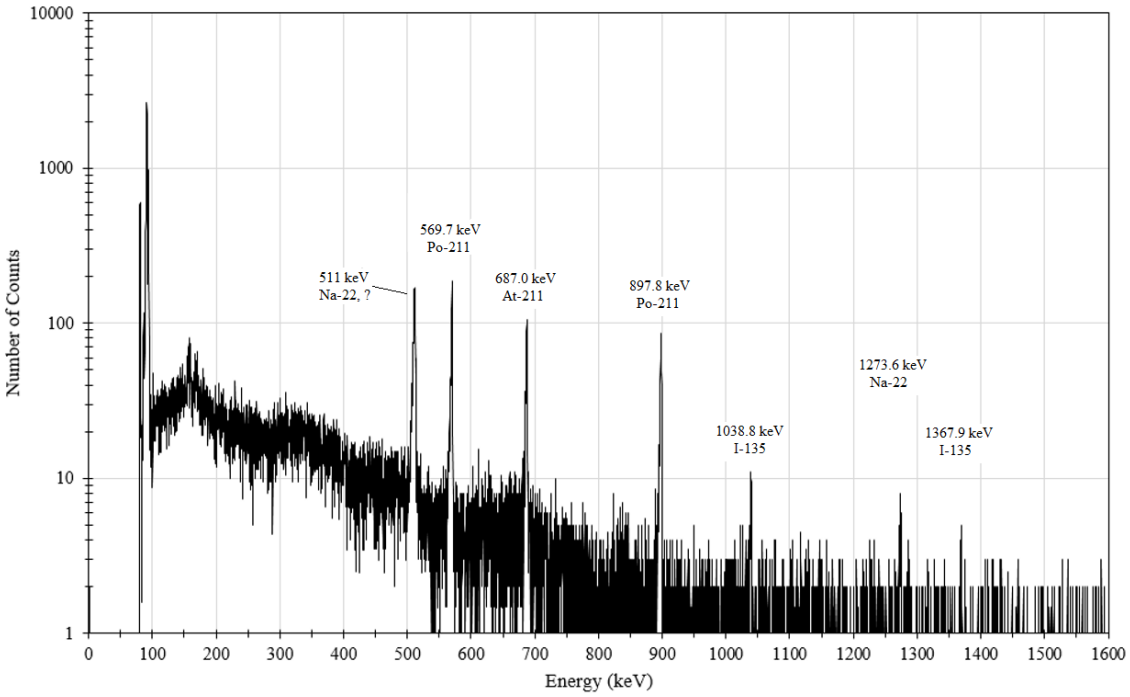

Figure 45. The gamma spectrum of the target for Experiment 3 prior to distillation.

Table 19. Calculated yields based on spectral data are provided for the target prior to distillation from Experiment 3.

Radionuclide	*Eγ* (keV)	Net Peak Area (Counts)	Net Peak Uncertainty (%)	Activity (MBq)	Activity (mCi)
^{211}At	687.0	464	5.3	1222 ± 65.7	33.05 ± 1.78
^{211}Po	569.7	681	4.2	817.4 ± 34.8	22.09 ± 0.94
	897.8	476	4.7	631.7 ± 30.1	17.07 ± 0.81
Median ^{211}At/^{211}Po				817.5 ± 80.2	22.09 ± 2.17

Elution from the new cold trap apparatus was finished in several steps. Prior to elution, one-minute G-M measurements of the cold trap showed 1318 ± 62 counts. The capillary was removed from the cold trap, and an initial flush with 2 mL of ethanol was washed back and forth through the capillary three times, prior to recovery in a 5 mL empty vial. One minute G-M measurements of the capillary coils after this flush averaged 1295 ± 51 counts. This suggested that negligible astatine was eluted, and was likely retained in the PEEK due to low temperature. The tubing was allowed to warm for several minutes, followed by the same washing procedures, using the same 2 mL of ethanol. One minute counts taken after the washing averaged 1314 ± 63 counts, essentially the same as the previous readings. Finally, the PEEK tubing was washed with 2 mL of sodium citrate solution, yielding an average cold trap count rate of 481 ± 38 counts, or approximately 37% of the average initial readings. The 5 mL vial containing the 4 mL mixture of ethanol and sodium citrate was counted in both dose calibrators using the ^{99m}Tc dial value (37.1), resulting in yields of 29.2 μCi and 30.4 μCi (average = 29.8 μCi).

Table 20. Estimated yields of contaminants are shown for the target prior to distillation from Experiment 3.

Radionuclide	*Eγ* keV)	Net Peak Area (Counts)	Net Peak Uncertainty (%)	Activity (MBq)	Activity (μCi)
^{210}At	245.3	--	--	--	--
	1181.4	--	--	--	--
	1436.7	--	--	--	--
	1483.4	--	--	--	--
	1599.5	--	--	--	--
Median ^{210}At				--	--
^{22}Na	511.0	708	4.7	2.124 ± 0.101	57.39 ± 2.73
	1273.6	43	12.1	0.401 ± 0.049	10.81 ± 1.33
Median ^{22}Na				1.262 ± 0.112	34.10 ± 3.04
^{135}I[a]	1038.8	38	18.1	4.158 ± 0.763	112.4 ± 20.6
	1367.9	25	22.3	3.873 ± 0.875	104.7 ± 23.7
Median ^{135}I[a]				4.015 ± 1.161	108.5 ± 31.4

a. Possible contaminant identity

Following elution, the 5-mL sample vial was counted with the HPGe detector at the close position, while the remaining target activity was sealed in a plastic bag and shielded by the hot cell. Estimated yield calculations following elution are shown in Table 21, with a spectrum shown in Fig. 46. The retained target was counted using the HPGe approximately 13 hours after the initial target assay. This long delay was an attempt to

characterize the impurity radionuclides by half-life. The change in activity of the ^{22}Na was negligible, as expected with a 2.602 y half-life. However, the number of counts at 511 keV still exceeded the number of counts at 1273 keV by approximately a factor of 10. This suggests the presence of annihilation radiation from a separate unknown source, with a half-life significantly greater than 13 hours. The ^{135}I half-life was estimated as 6.42 hr for the 1038.8 keV line, and as 4.61 hr for the 1367.9 keV line. Given the variance in the estimated activity seen in Table 18, and the nearness of the calculated value to the published value of 6.57 h (2.3 % and 29.8 %), the presence of ^{135}I was confirmed with some confidence. An additional benefit of the 13-hour delay was an attempt to measure the in-growth of ^{135}Xe. Iodine-135 decays into radioactive ^{135}Xe ($T_{1/2}$ = 9.14 hr), a well-known process that results in xenon precluded startup in nuclear reactors (Stacey 2004). Xenon-135 has several gamma emissions, with a predominant peak at 249.8 keV ($y_{249.8}$ = 0.9). None of the ^{135}Xe peaks were detected after counting, leading to the conclusion that the supposed ^{135}I was another radionuclide, or that the ^{135}Xe could escape the plastic bag enclosing the target. No ^{210}At impurity was present in the distillation sample, and only trace amounts of ^{135}I were detected, resulting in *RCP* = 99.964 ± 2.672 % and *RCY* = 55.79 ± 17.68 %.

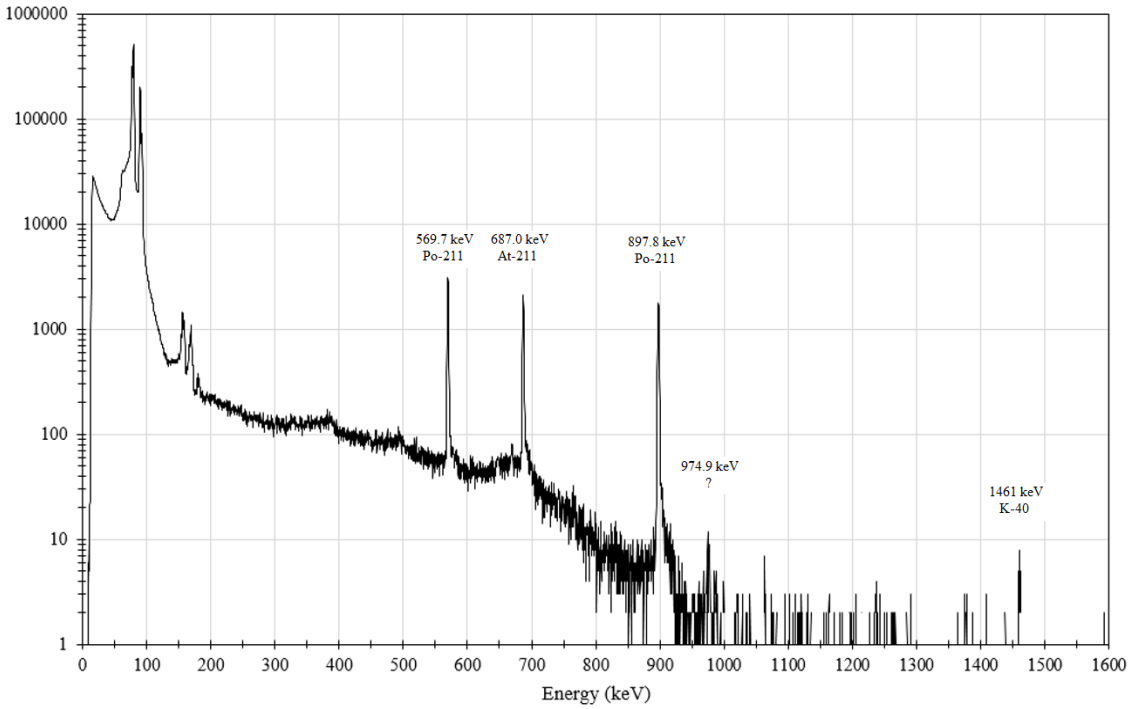

Figure 46. The gamma spectrum of the distillation aliquot from Experiment 3 is shown.

Table 21. Calculated yields based on spectral data are provided for the distillation aliquot for Experiment 3, including *RCP* and *RCY*.

Radionuclide	*Eγ* (keV)	Net Peak Area (Counts)	Net Peak Uncertainty (%)	Activity (MBq)	Activity (mCi)
^{211}At	687.0	12600	1.05	665.5 ± 7.04	17.99 ± 0.19
^{211}Po	569.7	18500	0.82	456.3 ± 3.76	12.33 ± 0.10
	897.8	12600	0.94	346.2 ± 3.25	9.36 ± 0.09
^{135}I	1038.8	83	22.49	0.186 ± 0.042	0.0050 ± 0.0011
	1367.9	45	27.42	0.143 ± 0.039	0.0039 ± 0.0011
Median ^{211}At/^{211}Po				456.3 ± 8.62	12.33 ± 0.23
Median ^{135}I				0.164 ± 0.057	0.0044 ± 0.0015
RCP ^{211}At/^{211}Po (%)				99.964 ± 2.672	
RCY ^{211}At/^{211}Po (%)				55.79 ± 17.68	

3.4 Experiment 4

The setup for Experiment 4 was identical to Experiment 3. The aluminum target backing for this experiment was made from high purity aluminum, obtained from the Cyclotron Institute, in an effort to remove ^{22}Na contaminants. Having gained confidence in target integrity from the previous run, Experiment 4 was run at slightly higher currents, that were stepped up to the maximum at a greater rate, resulting in a higher integrated

current of 29.19 μA_p-hr at 28.88 MeV (7.22 MeV u^{-1}). After a brief step-up regimen during the first hour, the target was irradiated for better than 7.5 hours at 6.9 μA_e.

The gamma spectrum for the target and target backing prior to distillation is shown in Fig. 47. Yield calculations based on the gamma spectrum are given in Table 22. The pyramidal indentations made it extremely difficult to separate the bismuth/astatine matrix from the aluminum backing plate, so they were counted together. Clear product gamma emissions are visible, with no visible contribution by ^{210}At. However, several impurity peaks not seen previously were present, at approximately 833 keV, 1038.8 keV, 1106.8 keV, and 1368.0 keV. The peaks at 1038.8 keV and 1367.9 were likely the ^{135}I contamination, as seen previously. The remaining peaks did not provide any definitive identification. Possible radionuclides are given in Table 23.

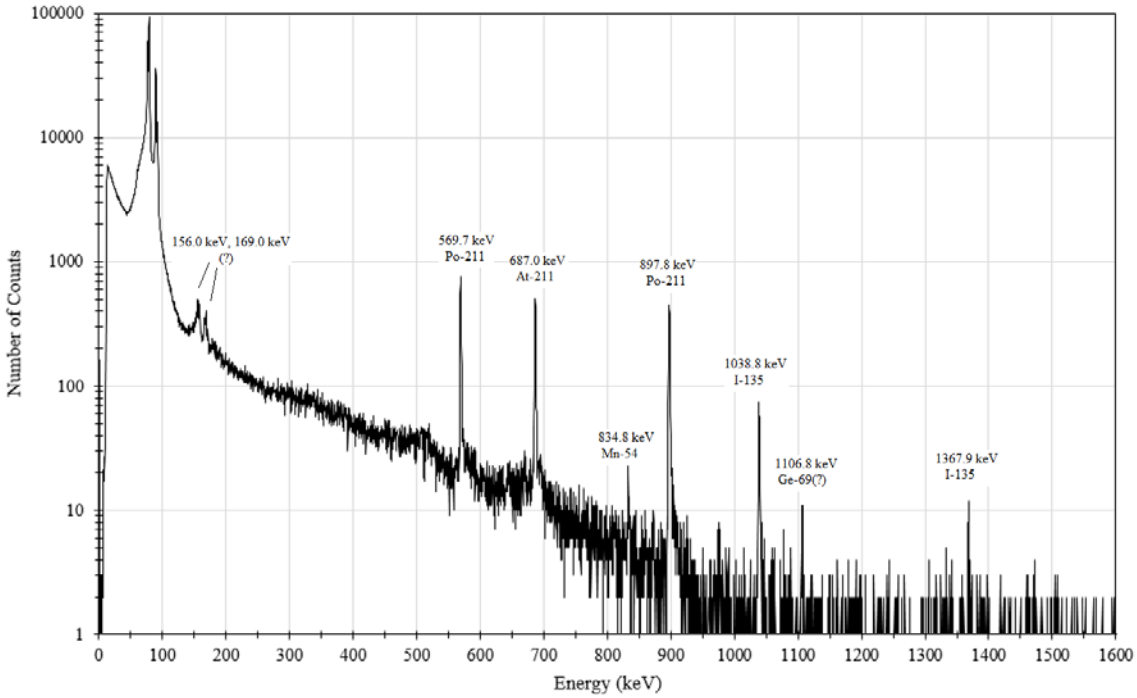

Figure 47. The gamma spectrum of the target and backing prior to distillation is shown for Experiment 4.

Table 22. Calculated yields based on spectral data are provided for the target prior to distillation from Experiment 4.

Radionuclide	*Eγ* (keV)	Net Peak Area (Counts)	Net Peak Uncertainty (%)	Activity (MBq)	Activity (mCi)
^{211}At	687.0	2710	2.58	1112.7 ± 29.2	30.45 ± 0.79
^{211}Po	569.7	3730	2.11	724.1 ± 15.3	19.57 ± 0.41
	897.8	3920	1.53	847.6 ± 12.9	22.91 ± 0.35
Median ^{211}At/^{211}Po				847.58 ± 35.37	22.091 ± 0.956

Table 23. Impurity gamma emissions and possible sources are shown (NNDC 2016).

$E\gamma$ (keV)	Radionuclide	$E\gamma$ (keV)	y_γ (Fraction)	$T_{1/2}$
833.0	^{54}Mn	834.8	1.00×10^{0}	312.2 d
1038.8	^{135}I	1038.8	7.95×10^{-2}	6.57 hr
1106.8	^{69}Ge	1107	3.60×10^{-1}	39.05 hr
1367.9	^{135}I	1367.9	6.08×10^{-3}	6.57 hr

Distillation followed the same general procedure as for Experiment 3, with a temperature ramp to 950 °C. However, in this case, the aluminum target backing remained attached to the bismuth/astatine target during distillation. Count rate and temperature are given as a function of time in Fig. 48. The same capillary tubing used in Experiment 3 was reused. After starting the furnace and submerging the coils in the cold bath, it was noticed that the flow had stopped, indicated by the lack of bubbles in the bubble trap, approximately 4 minutes after the process began. The coils and bubble trap were removed from the cold bath and allowed to warm until flow resumed. Intermittent flow stoppages occurred until sufficient warm argon had flowed through the tubing to warm it or elute the remaining solution within the tube. A full blockage again occurred at 24 minutes. After warming the capillary coils, the count rate significantly increased, indicating the volatilization of the astatine.

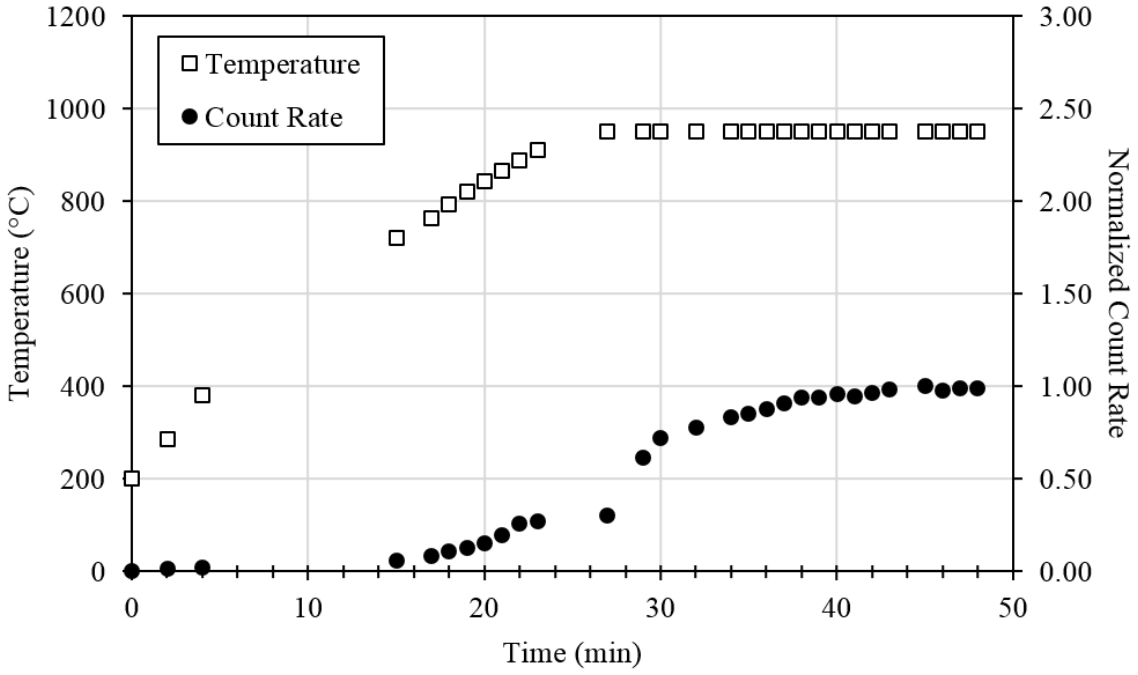

Figure 48. Count rate and furnace temperature data are shown for Experiment 4 during distillation. Blockages occurred in the cold trap coils at 4 minutes and 24 minutes, impeding argon flow.

Following successful distillation, elution occurred using 2 mL of sodium citrate solution, followed by a second wash of the same volume. The solution was collected into a 5 mL vial. Net count rate in the capillary tubing decreased from 9184 ± 192 to 1670 ± 58 during elution, correlating to an initial estimate of recovery of approximately 92%. The sample aliquot was counted with the HPGe in the close position. A spectrum is shown in Fig. 49, with tabulated yields in Table 24. The unknown peaks at 833.0 keV and 1106.8 keV were not distilled. A small fraction of ^{135}I was distilled, and no measurable ^{210}At was detected. This resulted in an *RCY* of 50.63 ± 1.17.

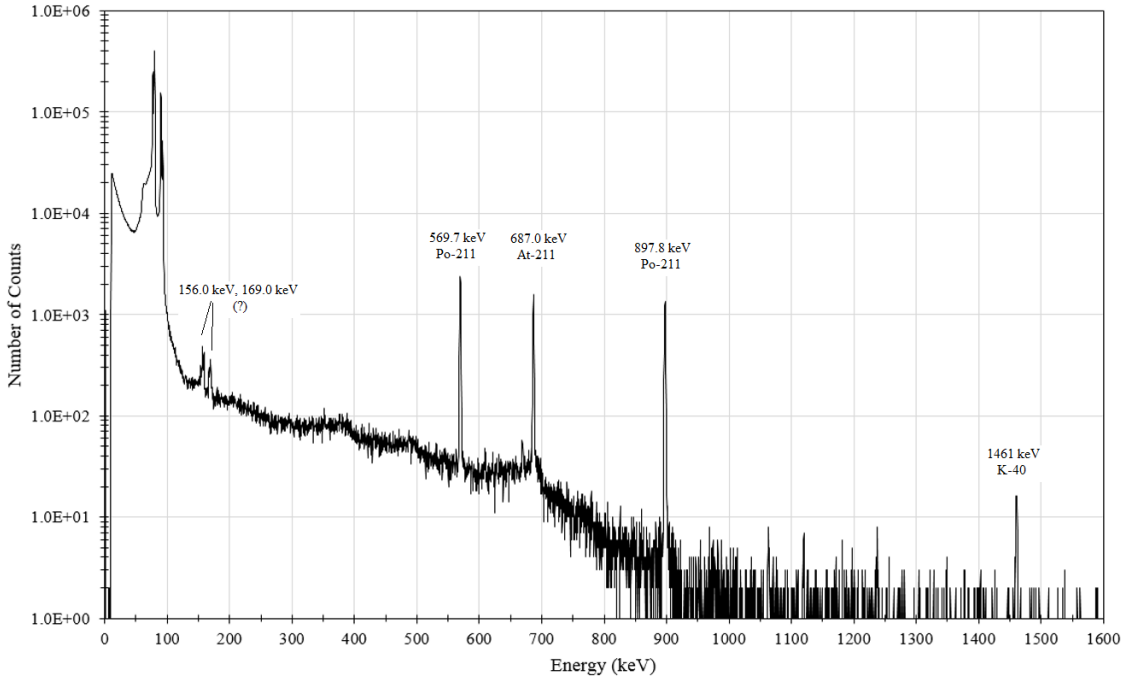

Figure 49. The gamma spectrum of the sample for Experiment 4 is shown after distillation.

Table 24. Calculated yields based on spectral data are provided for the sample after elution from Experiment 4.

Radionuclide	*Eγ* (keV)	Peak Area (Counts)	Peak Uncertainty (%)	Activity (MBq)	Activity (mCi)
^{211}At	687.0	7870	1.35	623.53 ± 8.42	16.85 ± 0.23
^{211}Po	569.7	11600	1.05	429.18 ± 4.51	11.60 ± 0.12
	897.8	8020	1.16	330.50 ± 3.82	8.93 ± 0.10
^{135}I	1038.8	33	25.15	0.110 ± 0.028	0.0030 ± 0.0007
	1367.9	13	35.46	0.062 ± 0.006	0.0017 ± 0.0006
Median ^{211}At/^{211}Po				429.18 ± 10.29	11.59 ± 0.28
Median ^{135}I				0.086 ± 0.035	0.0023 ± 0.0009
RCP ^{211}At/^{211}Po (%)				99.980 ± 0.024	
RCY ^{211}At/^{211}Po (%)				50.63 ± 1.17	

3.5 Experiment 5

The setup for Experiment 5 was identical to Experiment 4, including the new target backing. This new backing prevented the ^{22}Na contamination found in the previous experiment, and showed excellent thermal qualities. The target was quickly stepped to a maximum beam current of 6.5 μA_e at 28.88 MeV (7.22 MeV u^{-1}), and was irradiated for nearly 9 hours, resulting in an integrated current of 30.37 μA_p-hr. The target was firmly attached to the aluminum backing plate, so these components were assayed and distilled together.

The gamma spectrum prior to distillation is shown in Fig. 50, with initial yield calculations in Table 25. As can be seen, some impurity peaks are apparent, including at approximately 203 keV, 245 keV, and 511 keV. Also visible is the ^{40}K peak at 1650 keV. The source of the 203 keV and 511 keV is unknown. The 245 keV peak is indicative of ^{210}At, although other dominant ^{210}At peaks (1181 keV, 1436 keV, 1483 keV, 1600 keV) are not visible.

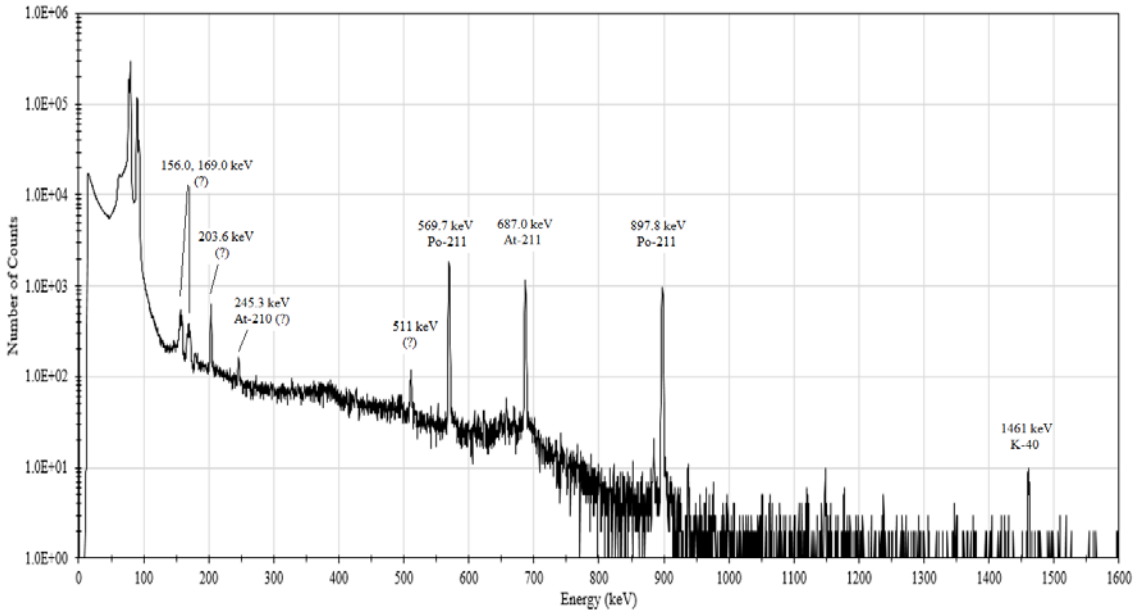

Figure 50. The gamma spectrum of the target for Experiment 5 is shown prior distillation.

Table 25. Estimated yields are shown prior to distillation for the Experiment 5 target.

Radionuclide	*Eγ* (keV)	Peak Area (Counts)	Peak Uncertainty (%)	Activity (MBq)	Activity (mCi)
^{211}At	687.0	6729	1.43	1250.6 ± 17.85	33.80 ± 0.48
^{211}Po	569.7	10160	1.10	790.5 ± 8.72	21.37 ± 0.24
	897.8	6903	1.25	714.9 ± 8.93	19.32 ± 0.24
Median ^{211}At/^{211}Po				790.5 ± 21.78	21.36 ± 0.59
^{210}At	245.3	391	8.73	0.069 ± 0.006	0.002 ± 0.0002
Unknown	511.1	435	11.77	--	--

New capillary tubing was used during the distillation for Experiment 5. The target and backing plate were heated together. The distillation procedure followed was the same as previously. Count rate plateaued for a significant amount of time. The cold trap coils were removed from the bath 55 minutes after the distillation began, as noted by the vertical line in Fig. 51. As the coils warmed, the count rate increased significantly, indicating that there was a partial blockage of the tubing.

After distillation, the coils were washed twice with 2 mL volumes of sodium citrate into a 5 mL vial. Counting occurred using the HPGe in the close position. The spectrum after elution, and estimated yields, are shown in Fig. 52 and Table 26. The line at 511 keV was still visible, but note the lack of peaks at 203 keV and 245 keV, indicating that they were not distilled. However, a peak at 976 keV became visible after the distillation process. The origin of the 967 keV peak was unclear, as was the 511 keV peak. However, using an assumed yield of 1.8 for the 511 keV peak (e.g. ^{18}F = 1.90, ^{22}Na = 1.81, ^{68}Ga = 1.78), an estimated activity approximately four orders of magnitude less than the product ^{211}At.

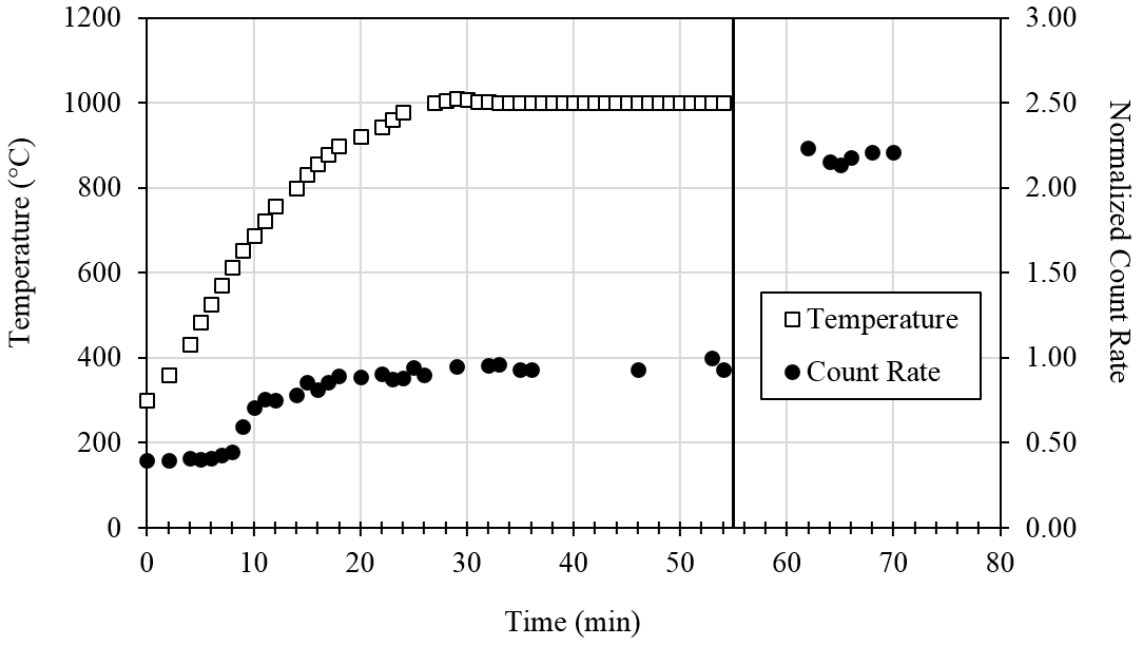

Figure 51. Count rate and furnace temperature data are shown for Experiment 5 during distillation. Cold trap coils were removed from the ice bath at 55 minutes.

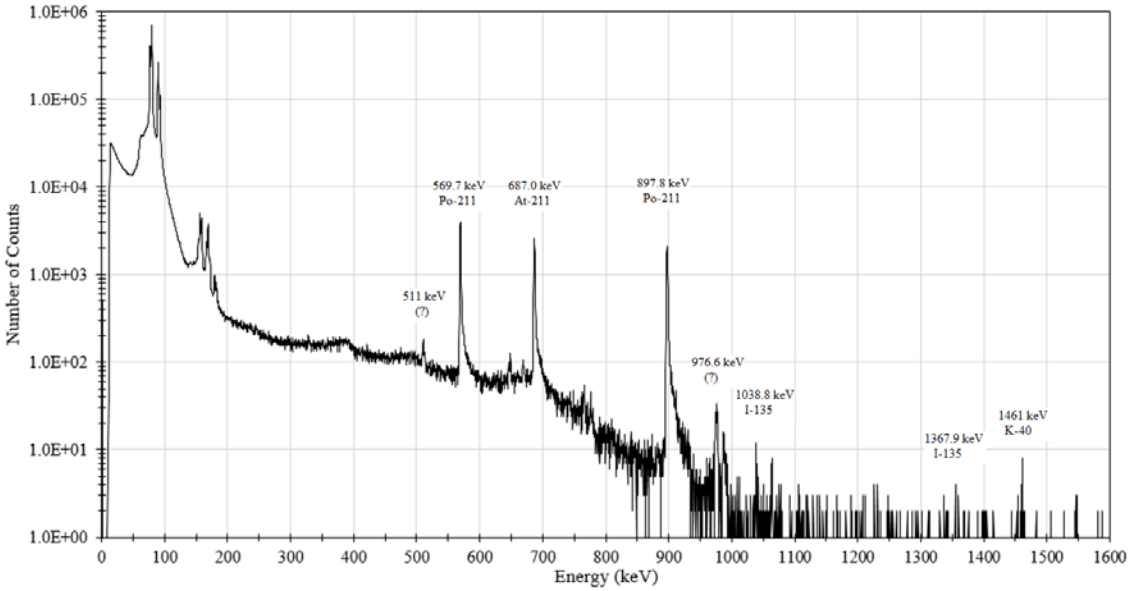

Figure 52. The gamma spectrum is shown for the sample of Experiment 5 after elution.

Table 26. Estimated yields are shown after distillation for the Experiment 5 sample.

Radionuclide	*Eγ* (keV)	Net Peak Area (Counts)	Net Peak Uncertainty (%)	Activity (MBq)	Activity (mCi)
^{211}At	687.0	14600	1.11	817.9 ± 9.1	22.10 ± 0.24
^{211}Po	569.7	20900	0.89	490.1 ± 4.4	13.25 ± 0.12
	897.8	14500	0.96	452.6 ± 4.4	12.23 ± 0.12
Median ^{211}At/^{211}Po				490.1 ± 10.9	13.25 ± 0.30
^{210}At	245.3	--	--	--	--
Unknown	511.1	676	12.41	0.038 ± 0.005	0.001 ± 0.00009
Unknown	976.6	234	8.40	--	--
RCP ^{211}At/^{211}Po (%)				99.992 ± 3.157	
RCY ^{211}At/^{211}Po (%)				62.00 ± 3.08	

3.6 Summary of Production Results

These five experiments satisfactorily produced ^{211}At with yields ranging between 10.73 – 39.17 MBq μA_p^{-1} h^{-1}, consistent with published yields, at maximum beam intensities on the order of 6-7 μA_p. Recovered yields were on the order of 20 mCi per production run after initial development (median 22.09 mCi ± 0.77). No contamination by ^{210}At or ^{210}Po was detected. However, the impurity ^{135}I was detected, as was ^{22}Na and possibly another positron emitter. Na-22 was successfully removed during distillation, and the remaining ^{135}I was present in the final product at levels much less than 0.005 kBq

MBq^{-1} ($\mu Ci\ mCi^{-1}$). The initial experiment, Experiment 1, was used as a proof of production. Production runs 2-5 followed the full distillation procedures, and were recovered for *RCP* and *RCY* analysis. Results are summarized below in Table 27.

Table 27. Yields and purity results are summarized for all production runs.

Exp.	**Yield EOB**	**Activity EOB**		***RCY***	***RCP***
	($MBq\ \mu A_p^{-1}\ h^{-1}$)	**(MBq)**	**(mCi)**	**(%)**	**(%)**
1	--	--	--	--	--
2	10.7 ± 0.101	11.71 ± 3.4	0.316 ± 0.09	21.13 ± 29.05	99.999 ± 6.036
3	39.2 ± 0.103	817.5 ± 80.2	22.09 ± 2.17	55.79 ± 17.68	99.964 ± 2.672
4	29.0 ± 0.100	847.6 ± 35.4	22.91 ± 0.96	50.63 ± 1.17	99.980 ± 0.024
5	26.0 ± 0.102	790.5 ± 21.8	21.36 ± 0.59	62.00 ± 3.08	99.992 ± 3.157

3.7 Radioactive Nanoparticles

Astatine from the final experiment was incorporated into colloidal gold nanoparticles. After recovery from the capillary with 38.8 mM sodium tricitrate solution, an aliquot of 35 μCi (approximately 100 μL after decay) was prepared. This solution was added in the nanoparticle formation process as described before, following the standard procedure, albeit scaled to 10 mL total volume. Following production, the nanoparticles were centrifuged at 11,540 G for 10 minutes. The supernatant was removed, and the nanoparticles were re-suspended and washed with fresh sodium citrate. The sample was

spun again, and the nanoparticles were re-suspended in 100 μL of sodium citrate. The supernatant and the samples were measured using the dose calibrator, and showed 28 μCi (~80%) retention of activity in the nanoparticles. This established that the colloidal gold nanoparticles were successfully formed with radioactive ^{211}At strongly encapsulated within the nanoparticles. The final solution was placed in a cuvette and diluted to a volume of 1 ml. Using UV-Vis, the wavelength and absorbance peak were measured to assess the nominal nanoparticle size and concentration. The measured wavelength was 525 nm with an absorbance peak of 0.8 (a.u.). The nominal nanoparticle diameter was estimated at 35.1 nm, consistent with preliminary results with non-radioactive nanoparticles. The estimated extinction coefficient was 8.45×10^{9} M cm^{-1}. Based on the Beer-Lambert equation, the resulting nanoparticle concentration was estimated at 5.7×10^{10} cm^{-3}. The total number of radioactive atoms in the nanoparticles was 3.88×10^{10} cm^{-3}, which corresponds to a nominal μ of 1.47. The resulting distribution of radioactive atoms per nanoparticle is given in Fig. 53. The present strategy of encapsulating radioactive atoms in nanoparticles will allow for further functionalization of the nanoparticle corona with biologically active molecules, such as mAbs and positron emitting radionuclides for further detection as shown in Fig. 54, and as described previously using the anti-HER2 MAb.

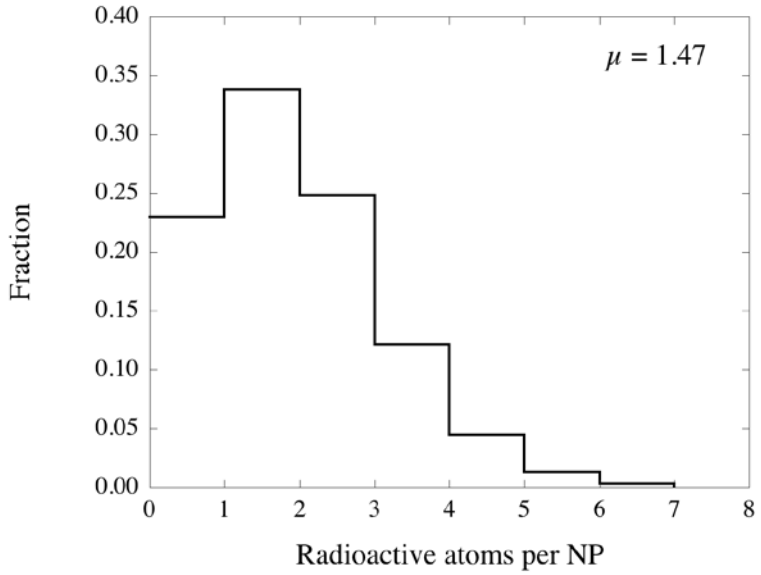

Figure 53. Distribution of radioactive atoms per nanoparticle based on a nominal mean of μ = 1.47. The fraction of nanoparticles with no radioactive atoms was 0.23, and the fraction with one or more radioactive atoms was 0.77.

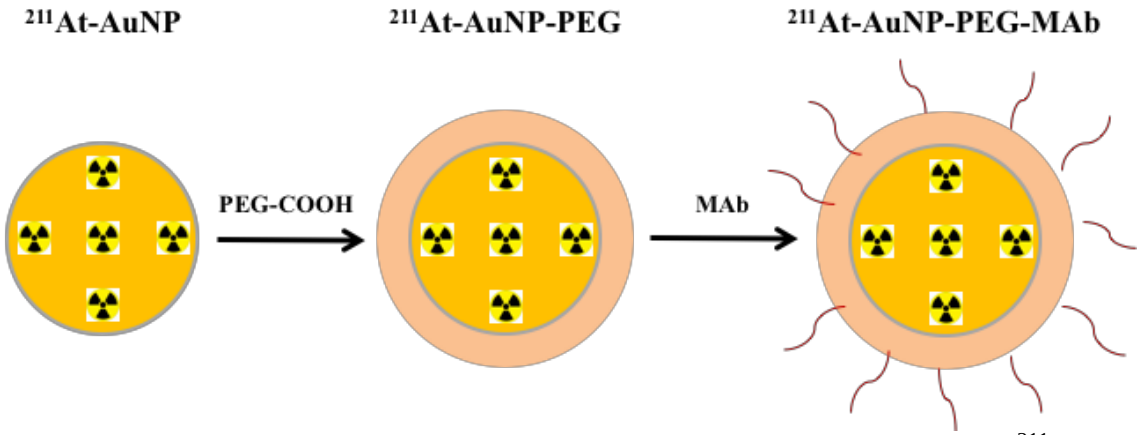

Figure 54. Sketch showing the strategy for encapsulating radioactive atoms of ^{211}At and further functionalizing the nanoparticles using a monoclonal antibody.

4. DISCUSSION AND FUTURE WORK

The production experiments presented herein highlight the ability to consistently produce ^{211}At at levels acceptable for preclinical research utilizing a research cyclotron. Experiments 1 and 2 were proof of concept trials of the new target and distillation apparatus. Experiment 1 showed that passive cooling is not an option, with negligible ability to produce ^{211}At under these conditions. Experiment 2 included use of the water chiller and allowed for significant production. However, the radiochemistry lab set up and preparation, distillation process, and general procedures left much to be desired. Several small changes were made to the room preparation and process flow to expedite handling of the target in Experiment 3. Experiments 3-5 showed marked improvements in yield and total recovered product.

Radionuclidic purity was sufficiently pure in Experiments 3-5 for preclinical trials. Official guidelines are not in place for ^{211}At radionuclidic purity in clinical use, but expected values can be compared to other radionuclides. For example, pertechnetate must meet 1.5×10^{-4} mCi of ^{99}Mo per mCi of ^{99m}Tc (U.S. Pharmacopeia 2005). In our case, Experiment 5 meets this requirement at 7.5×10^{-5}, while Experiments 3 and 4 ranged from $1.9 – 3.6\times10^{-4}$. This level of purity may prove to be adequate. Understanding the source of the iodine impurity and removing it from future production runs will be key to increasing radionuclidic purity, as no other contaminants, including ^{210}At or ^{210}Po, were detected in the final solutions. As ^{135}I was not reported in any of the literature, the most likely source is from the thermal conduction grease used on the target backing. Removing

this grease from future experiments will reduce the maximum beam current on target; however, with the water chiller in place, the expected decrease in allowable current should be negligible, on the order of 5-6 μA_e. Further developments in target preparation, primarily in reducing the thickness of the bismuth layer to less than 30 μm, will allow the Bragg peak to be centered in the aluminum backing plate, allowing for higher currents. It was impossible to confirm the identity of the ^{135}I by measuring its daughter ^{135}Xe. This is due to the constant removal of air from the fume hood and hot cell where the target was stored, as well as the air turnover rate in the radiochemistry room. The relatively long half-life (9.14 h) of ^{135}Xe means it was likely exhausted prior to decay. Decays that did occur near the detector were not quantifiable due to the low decay rate, relatively low gamma-emission rate (see Appendix A), and inconsistent geometry due to the dispersion of the gas. The inert nature of the noble gas ensured that it was not captured in the effluent air monitors or charcoal exhaust filters. The distillation apparatus and vessels were continuously vented through the charcoal filter and flushed with the argon gas flow. The boiling point of xenon (-108.1 °C) is below the temperature of the cold trap, so no impurity ^{135}Xe was captured during the distillation process.

Developed targetry and recovery apparatus have proven satisfactory as the basis for routine production development. However, to realize routine production able to meet consistent research demand, several improvements and considerations must be taken into account. Key elements are automation and modularization of components, adapting the apparatus to current widespread cyclotron infrastructure, assessing cost reduction

methods, furthering long-term preclinical *in vivo* studies to assess late radiotoxicity effects, and standardization of delivery methods.

Several attempts have been made to facilitate automation and routine production capabilities using ^{211}At. Use of premade components to shorten handling time is a development goal, as they could be sold and used in kit-like form. Commercial biomedical cyclotron facilities utilize kit-based components for the large-scale manufacture of radiopharmaceuticals, such as ^{18}FDG (Martin and Akabani 2012). Long-term storage of Anti-HER2 (Anti-CD340) tin-based immunoconjugates has been shown to be stable in Phosphate Buffered Saline (PBS) at pH>7 and 4 °C for greater than 3 months (Aneheim et al. 2015c). Similarly, development of kit based ^{211}At-MABG, the astatine analog to MIBG, has been favorable at clinical studies scales (Vaidyanathan et al. 2007). This would be ideal for long distance shipping, and for reliable and repeatable radiochemistry at newly established facilities.

A necessary development is the inclusion of automatic synthesis instead of manual manipulation. Automated controls, which can be run by dedicated computer software, are fundamental to routine use within a hot cell. While it is helpful to have a flexible laboratory during preclinical investigations, where concentrations and methods can be optimized for the task at hand, routine production and FDA approvals mandate reproducible and consistent methods. An essential part of this quality control step is the minimization of human interaction. However, automation is not without its own problems. Miniaturization of equipment, and the associated reduction in volume of components and feedstock, can lead to large percentage errors and significant loss in dead volumes, such as the capillary

cold trap coils and valves. Automation has been partially developed for tin-based immunoconjugates, but more work is needed. An estimate of 100 μL minimum volumes are needed to minimize variation to an acceptable level, but these amounts still result in approximately 10% deviations (Anaheim et al. 2015c).

An example of a preliminary distillation and recovery apparatus utilizing standard modular and microfluidic components is shown in Fig. 55 (Anaheim 2015a). In this figure, the various components are given as: a) tube furnace; b) quartz crucible; c,d) 3-way automated valves; e) cold trap; f) reaction vial for radiolabeling; g) bubbler and charcoal traps; h) vacuum pump; i,j) reactants; k) size-exclusion column and PIN diode detector; l) syringe loader; m) end-product. This unit has been developed by Anaheim, part of the Lindegren group at Gothenburg University in Sweden. This is the latest development by this group, which has been one of the leaders in investigating ^{211}At production and recovery since the early 2000's. Use of this automated apparatus has resulted in distillation yields from 87-92% using a mixture of methanol and NIS, with labeling yields of N-succinimidyl 3-(trimethylstannyl)benzoate (m-MeATE) immunoconjugates on the order of 75% with excellent *RCP* (Anaheim et al. 2015a, 2015c).

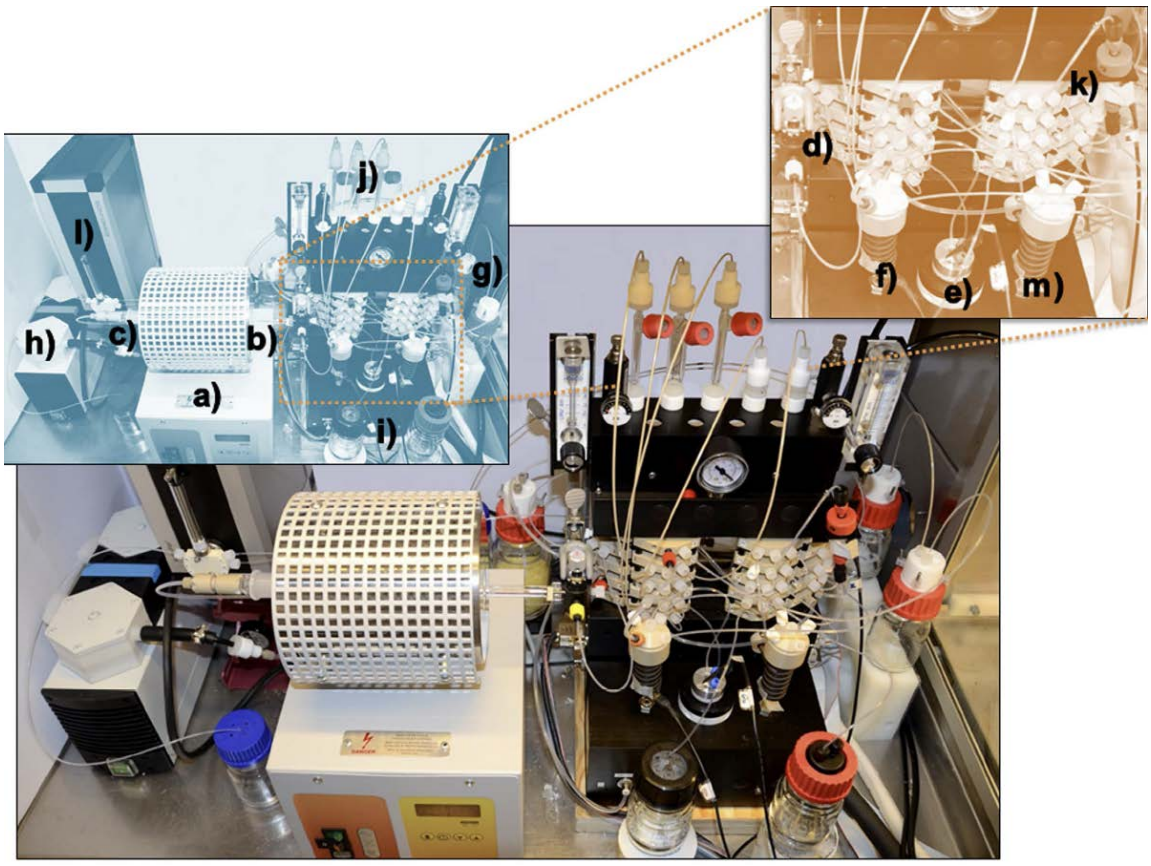

Figure 55. A semi-automated and modular system for distillation and synthesis of ^{211}At to m-MeATE-conjugates. See text for explanation of individual components.

The apparatus in Fig. 55 is contained within a glove box, and is similar in size to the apparatus used in these experiments (c.f. Fig. 16). The tube furnace is by far the bulkiest item in both setups. By implementing an induction furnace, it is expected to reduce the overall size of the distillation apparatus such that is can fit in a standardized hot cell module enclosure. An example of a commercially available miniature induction furnace is shown in Fig. 56. A device similar to this could be adapted to astatine production by changing the geometry of the induction coils to contain the quartz crucible. The power

supply and controller could be conveniently located outside of the hot cell. Induction furnaces provide several advantages in addition to size: heating time is greatly reduced, and temperature can be easily controlled using a PLC controller to adjust current. This means the control system can be integrated, without having to drive proprietary components, as is the case with the Carbolite tube furnace. Heating requires that the aluminum target backing plate remains attached to the target; however, this is not an issue as the final target design was firmly fixed to the backing plate.

Figure 56. A commercially available miniature induction furnace. The coil is capable of inducing temperatures more than 1100 °C. The power supply and controller may be remotely mounted.

A simplified method for producing ^{211}At in methanol and sodium citrate solution has been examined. Automating the process to produce no-carrier-added ^{211}At in a common buffer solution will provide the radionuclide in a form compatible with almost all standard immunoconjugation applications (Dadachova 2010, Cederkrantz et al. 2015). The standardized product could then be tailored to study-specific needs. A schematic of the proposed method is given in Fig. 57.

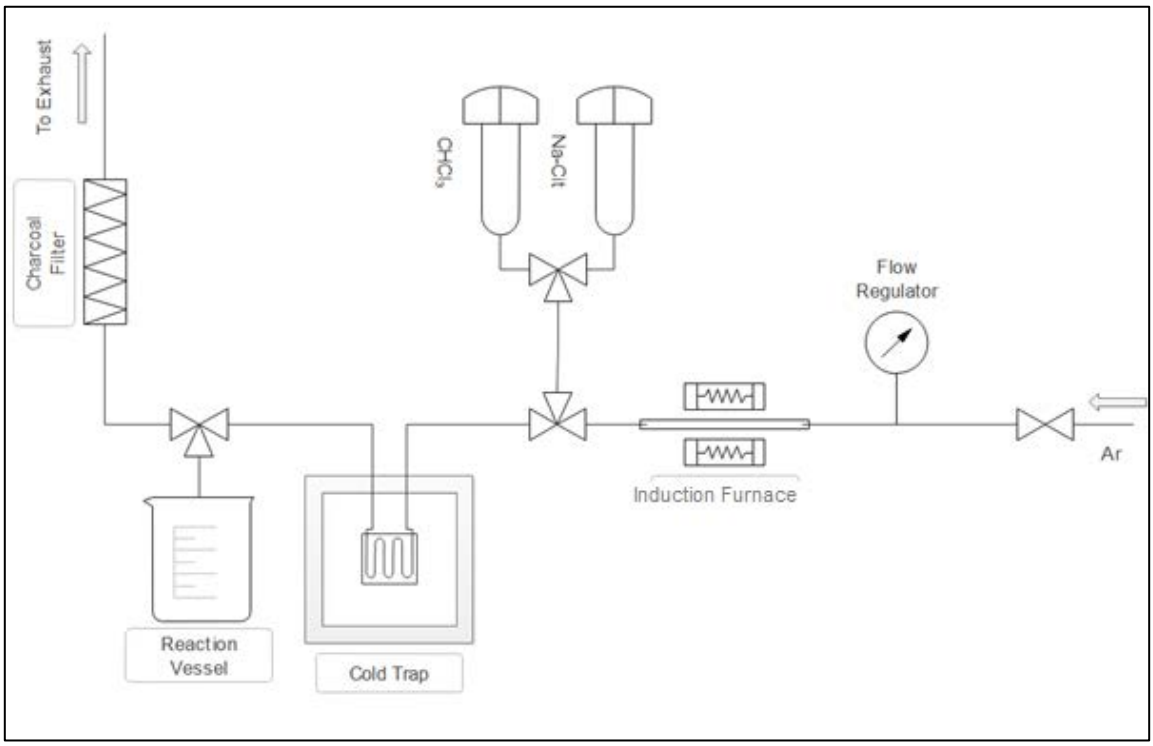

Figure 57. A schematic of a modularized and automated ^{211}At distillation apparatus.

Standard components utilizing PEEK capillary tubing and Upchurch microfluidic connectors (IDEX Health and Science LLC, 619 Oak Harbor, WA 98277) will make the module compatible with pre-existing cyclotron facility components. Laboratory supplied inert gas, usually helium, is used both to entrain the volatilized ^{211}At, as well as to operate the pneumatic valves and syringe pumps. An example of a similar module, in use to synthesize ^{18}FDG, is shown in Fig. 58 (ABX GmbH, Heinrich-Glaeser-Strasse 10-14, D-0454, Germany). This shows an example of what the completed module would look like. Automation and control will be provided by the industry standard LabVIEW control software (National Instruments, 11500 N. Mopac Expwy, TX 78759).

Figure 58. An example of a production module, showing pneumatically controlled syringe pumps and valves (ABX, Germany).

Introduction of targetry compatible with automated methods is of additional importance. Remote loading and unloading of targets required for reducing operator dose in high-yield routine batches. While dose rate from the product ^{211}At is relatively low, activated equipment and target backing aluminum (^{28}Al) will have high dose rates, especially for batches with hundreds of mCi end-product. In the routine production scenario, it is impractical and uneconomical to wait for these activation products to decay;

furthermore, routine daily production would cumulatively expose workers beyond ALARA considerations. Remote target unloading is therefore essential. One such target is the NIRTA solid target solid system from IBA (IBA USA, 2000 Edmund Halley Drive Ste. 210, VA 20191). This target has been purchased for future development, and is shown in Fig. 59.

The NIRTA target features remote loading and unloading of target disks, and extensive active cooling through chilled water on the rear of the target, and helium cooling on the front face of the target. The solid target version of the NIRTA system was developed for high activity production of ^{64}Cu and ^{62}Zn/^{62}Cu, and is more than capable of tolerating routine heat loads for ^{211}At production, provided the bismuth target layer is sufficiently thin. Due to these features, the target is held perpendicularly to the incident beam. While this does not allow for spreading the beam out on target, it does allow a for an optimal target thickness of approximately 30 μm, as opposed to ~ 5 μm for the angled target. In collaboration with material science specialist in the Mechanical Engineering department, it is expected that these target thicknesses can be produced uniformly using pulsed laser deposition (PLD) or conventional sputtering and physical vapor deposition (PVD) techniques. Uniformity of thickness and reproducibility will be required to reliably maintain routine production.

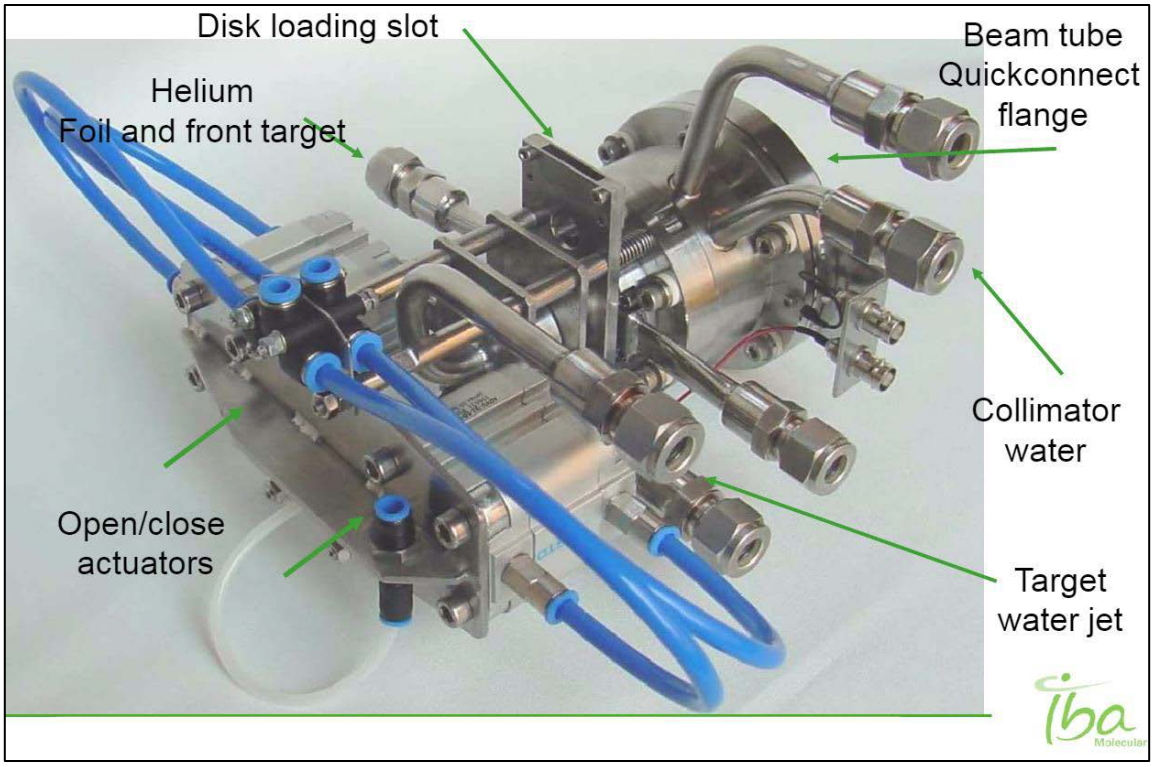

Figure 59. The NIRTA solid target system is shown. In this view, the beam enters from the top right, through the center of the circular flange.

An additional purpose of future work is to assess the cost of production. In 2011, estimated cost of high-level production at an established facility was on the order of $50-60 per mCi of ^{211}At, contrasted with approximately $70 per mCi of ^{123}I (Zalutsky and Pruszynski 2011). However, the cost of facility set up is very prohibitive, as well as for a cyclotron capable of using alpha particle beams. What is not considered is the wide availability of cyclotrons capable of producing ^{123}I in current usage via the common p or d beams on tellurium targets. While considerable finances are available for medical

research and administration, ^{211}At based targeted therapy must be shown to be significantly more effective, and/or comparable in costs, or no market for it will develop.

In addition to automation, more long-term studies are needed for effects of ^{211}At *in vivo*. While the effectiveness of targeted therapies using ^{211}At is well known, toxicity and long-term effects in the body are poorly quantified (McLendon et al 1999, Akabani et al. 2006). The FDA put out requirements in 2011 requiring extensive long-term study of late radiotoxicity of therapeutic radiopharmaceuticals prior to approval for use in humans (U.S. FDA 2011). For example of the importance of this, the long-term effects of anti-tenascin (anti-81C6) labeled ^{211}At as an endoradiotherapeutic agent for the treatment of brain tumors has been investigated. Long term radiotoxicity is present, with an LD_{10} of approximately half that found for ^{211}At in astatide form. However, toxic effects are not seen except in the highest animal doses, approaching 100 kBq g^{-1}. This would provide an initial upper limit of doses for human tests (McLendon et al. 1999).

Other promising future studies include development using immunoconjugation techniques coupled with colloidal gold-based nanoparticles. Colloidal gold nanoparticles with incorporated ^{211}At would provide an interesting, and potentially very effective, route of treatment for several types of tumors, especially hepatocellular carcinoma and renal cancers (Wilbur et al. 1993, Paciotti et al. 2006). This is especially promising for NHS/EDC coupling to antibodies for increased efficacy in targeting (Bartczak and Kanaras 2011). Gold nanoparticles also have the benefit of being easily imaged using MR or CT. Alternatively, diagnostic radionuclides, such as ^{124}I, may be incorporated as well, allowing for a hybrid diagnostic and therapeutic approach. PET image reconstruction of

the therapeutic distribution within the body would make for accurate dose estimates without the need to sacrifice the subject to harvest individual organs or perform autoradiography. The benefit in human research for such a use is obvious. We have previously investigated these methods utilizing radioiodine as astatine analogs (Clanton and Akabani, 2017). Preliminary research has been completed using the ^{211}At produced in these experiments, as discussed in the results section. Future development of this method, including higher specific activity per nanoparticle, protein labelling, and *in vitro* experiments will be forthcoming following future ^{211}At production experiments.

5. CONCLUSION

An inclined external solid target was developed capable of undergoing extended (8+ h) irradiations of 29 MeV (7.25 MeV u^{-1}) alpha particles at currents up to 7 μA_e. A dry distillation apparatus and process was developed to recover the astatine while negating radiochemical contamination from target byproduct materials. Several production irradiations were performed with favorable results. Production yields ranged between 10.73 – 39.17 MBq μA_p^{-1} h^{-1} (0.290 – 1.058 mCi μA_p^{-1} h^{-1}), consistent with published yields, at average beam intensities on the order of 5-10 times that used in previous experiments (2-3 μA_p). Recovered yields were on the order of 740 MBq (20 mCi) per production run after initial development (median 22.09 mCi ± 0.77). No contamination by ^{210}At or ^{210}Po was detected in any of the final products. Trace amounts of ^{135}I were present in some instances, with maximum amounts of < 0.04% final yield.

Overall, production utilizing these methods has proven feasible for small-scale studies utilizing 1-20 mCi per experiment. Development of further process automation and miniaturization, as well as quality assurance and control protocols, will be required for forthcoming standardized production.

REFERENCES

Aaij C, Tschroots WRJM, Linder L, Feltkamp TEW. The preparation of astatine labelled proteins. Int J Appl Radiat Isot 26(1):25IN129-28IN230; 1975.

Akabani G, Carlin S, Welsh P, Zalutsky MR. In vitro cytotoxicity of At-211-labelled trastuzumab in human breast cancer cell lines: effect of specific activity and HER2 receptor heterogeneity on survival fraction. Nucl Med Biol 33:333-347; 2006.

Alfarano A, Abbas K, Holzwarth U, Bonardi M, Groppi F, Alfassi Z, Menapace E, Gibson PN. Thick target yield measurement of (211)At through the nuclear reaction 209Bi(alpha, 2n). J Phys Conference Series 41(1):115; 2006.

Amendola V, Meneghetti M. Size evaluation of gold nanoparticles by UV-Vis spectroscopy. J Phys Chem C 113:4277-4285; 2009.

Andersson H, Palm S, Lindegren S, Back T, Jacobsson L, Leser G, Horvath G. Comparison of the therapeutic efficacy of (211)At and (131)I labelled monoclonal antibody MOv18 in nude mice with intraperitoneal growth of human ovarian cancer. Anticancer Res 21(1A):409-412; 2000.

Andersson H, Elgqvist J, Horvath G, Hultborn R, Jacobsson L, Jensen H, Borje Karlsson, Lindegren S, Palm S. Astatine-211-labeled antibodies for treatment of disseminated ovarian cancer. Clin Cancer Res 9(10):3914s-3921s; 2003.

Andersson H, Cederkrantz E, Back T, Divgi C, Elgqvist J, Himmelman J, Horvath G, Jacobsson L, Jensen H, Lindegren S, Palm S, Hultborn R. Intraperitoneal alpha-particle radioimmunotherapy of ovarian cancer patients: pharmacokinetics and dosimetry of At-211-F(ab')2 - a phase I study. J Nucl Med 50:1153-1160; 2009.

Aneheim E, Albertsson P, Back T, Jensen H, Palm S, Lindegren S. Automated astatination of biomolecules – a stepping stone towards multicenter clinical trials. Scientific Reports 5:1-11; 2015a.

Aneheim E, Foreman MRSJ, Jensen H, Lindegren S. N-[2-(maleimido)ethyl]-3-(trimethylstannyl)benzamide, a molecule for radiohalogenation of proteins and peptides. Appl Radiat Istot 96:1-5; 2015b.

Aneheim E, Hallerod J, Albertsson P, Jensen H, Holgersson S, Lindegren S. Shelf-life of eta-lysyl-3-(trimethylstannyl)benzamide immunoconjugates, precursors for At-211 labeling of antibodies. Cancer Biother and Radiopharm 30(1):41-45; 2015c.

Aneheim E, Jensen H, Albertsson P, Lindegren S. Astatine-211 labeling: a study towards automatic production of astatinated antibodies. J Radioanal Nucl Chem 303:979-983; 2015d.

Ansoborlo E, Berard P, Den Auwer C, Leggett R, Menetrier F, Younes A, Montavon G, Moisy P. Review of chemical and radiotoxicological properties of polonium for internal contamination purposes. Chem Res Toxicol 25:1551-1564; 2012.

Appelman EH. The radiochemistry of astatine. US Atomic Energy Commission, Report NAS-NS 3012: Washington DC, USA; 1960.

Attix FH. Introduction to radiological physics and radiation dosimetry, 2nd ed. Weinheim: WILEY-VCH Verlag GmbH & Co. KGaA; 2004.

Aurlien E, Larsen RH, Kvalheim G, Bruland OS. Demonstration of highly specific toxicity of the alpha-emitting radioimmunoconjugate (211)At-rituximab against non-Hodgkin's lymphoma cells. Brit J Cancer 83(10)1375; 2000.

Azad TD, Razavi SM, Jin B, Lee K, Li G. Glioblastoma antigen discovery – foundations for immunotherapy. J Neurooncol 123(3):347-358; 2015.

Back T, Andersson H, Divgi CR, Hultborn R, Jensen H, Lindegren S, Palm S, Jacobsson L. (211)At radioimmunotherapy of subcutaneous human ovarian cancer xenografts: evaluation of relative biologic effectiveness of an alpha-emitter in vivo. J Nucl Med 48(12):2061-2067; 2005.

Back T, Haraldsson B, Hultborn R, Jensen H, Johansson ME, Lindegren S, Jacobsson L. Glomular filtration rate after alpha-radioimmunotherapy with At-211-MX35-F(ab')2: a long term study of renal function in nude mice. Cancer Biotherapy Radiopharm 24:649-658; 2009.

Balkin ER, Hamlin DK, Gagnon K, Chyan MK, Pal S, Watanabe S, Wilbur DS. Evaluation of a wet chemistry method for isolation of cyclotron produced At-211. Appl Sci 3:636-655; 2013.

Bartczak D, Kanaras AG. Preparation of peptide-functionalized gold nanoparticles using one pot EDC/sulfo-NHS coupling. Langmuir 27(16):10119-10123; 2011.

Basunia MS, Shugart HA, Smith AR, Norman EB. Measurement of cross sections for alpha-induced reactions on (197)Au and thick-target yields for the (a,y) process on (64)Zn and (63)Cu. Physical Rev C 75(1): 015802; 2007.

Bergeron DE, Cessna JT, Golas DB, Young RK, Zimmerman BE. Dose calibrator manufacturer-dependent bias in assays of (123)I. Appl Radiat Isot 90:79-83; 2014.

Bhakta VS. Production of the alpha-particle emitting radionuclide astatine-211 at the Texas A&M Cyclotron Institute. College Station, TX: Texas A&M University; 2011. Thesis.

Birattari C, Bonardi M, Groppi F, Martinotti A, Morzenti S, Ridone S, Acchini M, Abbas K, Alfarano A, Holzwarth U, Menapace E. First experiment for alpha-cyclotron production, radiochemical processing and quality controls of the alpha emitter astatine-211/polonium-211g for high-LET metabolic radiotherapy. Quart J Nucl Med Mol Imag 48; 2004.

Biodex Atomlab 500 dose calibrator operation and service manual, 10-096, Rev G:1-248; 2016.

Blasberg RG, Nakagawa H, Bourdon MA, Groothuis DR, Patlak CS, Bigner DD. Regional localization of a glioma-associated antigen defined by monoclonal antibody 81C6 in vivo: kinetics and implications for diagnosis and therapy. Cancer Res 47(16):4432-4443; 1987.

Boskovitz A, McLendon RE, Okamura T, Sampson JH, Bigner DD, Zalutsky MR. Treatment of HER2-positive breast carcinomatous meningitis with intrahecal administration of alpha-particle-emitting (211)At-labeled trastuzumab. Nucl Med Biol 36(6):659-669; 2009.

Bourgeois M, Guerard F, Alliot C, Mougin-Degraef M, Rajerison H, Saec PRL, Gestin JF, Davodeau F, Cherel M, Barbet J, Faivre-Chauvet A. feasibility of the radioastatination of a monoclonal antibody with astatine-211 purified by wet extraction. J Label Compd Radiopharm 51:379-383; 2008.

Brown I, Carpenter RN, Mitchell JS. The development of a [211At]-astatinated endoradiotherapeutic drug: Part I. Localization by alpha-particle autoradiography in a murine tumor model. Int J Radiat Onc Biol Phys 23(3):563-572;1992.

Brown I, Mitchell JS. The development of a [211At]-astatinated endoradiotherapeutic drug: Part II. Therapeutic results for transplanted adenocarcinoma of the rectum in mice and associated studies. Int J Radiat Onc Biol Phys 29(1):115-124; 1994.

Cederkrantz E, Andersson H, Bernhardt P, Back T, Hultborn R, Jacobsson L, Jensen H, Lindegren S, Ljungberg M, Magnander T, Palm S, Albertsson P. Absorbed doses and risk estimates of At-211-MX35 F(ab')-2 in intraperitoneal therapy of ovarian cancer patients. Int J Radiation Oncol Biol Phys 93(3):569-576; 2015.

Cederkrantz E, Back T, Jacobsson L, Jensen H, Lindegren S, Palm S, Albertsson P. Effective dose of intraperitoneal alpha-radioimmunotherapy with At-211. J Nucl Med 55:214; 2014.

Chattopadhyay N, Cai Z, Pignol JP, Keller B, Lechtman E, Bendayan R, Reilly RM. Design and characterization of HER-2-targeted gold nanoparticles for enhanced x-radiation treatment of locally advanced breast cancer. Molecular pharmaceutics 7:2194-206; 2010.

Cheetham PJ, Petrylak DP. Alpha particles as radiopharmaceuticals in the treatment of bone metastases: Mechanism of action of Radium-223 chloride (alpharadin) and radiation protection. Oncology 26(4):330-341; 2012.

Chen Y, Kornblit B, Hamlin DK, Sale GE, Santos EB, Wilbur DS, Storer BE, Storb R, Sandmaier BM. Durable donor engraftment after radioimmunotherapy using alpha-emitter astatine-211-labeled anti-CD45 antibody for conditioning in allogeneic hematopoietic cell transplantation. Blood 119:1130-1138; 2012.

Cheng J, Ekberg T, Engstrom M, Nestor M, Jensen HJ, Tolmachev V, Anniko M. Radioimmunotherapy with Astatine-211 using chimeric monoclonal antibody U36 in head and neck squamous cell carcinoma. Laryngoscope 117(6):1013-1018; 2007.

Claesson AK, Stnerlow B, Jacobsson L, Emroth K. Relative biological effectiveness of the alpha-particle emitter (211)At for double-strand break induction in human fibroblasts. Rad Res 167(3):312-318; 2007.

Claesson K, Magnander K, Kahu H, Lindegren S, Hultborn R, Elmroth K. RBE of alpha-particles from (211)At for complex DNA damage and cell survival in relation to cell cycle position. Int J Rad Biol 87(4):372-384; 2011.

Clanton R, Akabani G. Rapid synthesis of 125-I integrated gold nanoparticles for use in combined neoplasm imaging and targeted radionuclide therapy. Submitted to: Appl Radiat Isot; 2016.

Clark JL. The carrier-free isolation of astatine from thick bismuth targets. Collected Radiochemical and Geochemical Procedures, 5th Ed. Los Alamos National Lab, NM: Report Number LA-1721-5th-Ed; 1990.

Dadachova E. Cancer therapy with alpha-emitter labeled peptides. Semin Nucl Med 40: 204-208; 2010.

Danielsson A, Claesson K, Parris TZ, Helou K, Nemes S, Elmroth K, Elgqvist J, Jensen H, Hultborn R. Differential gene expression in human fibroblasts after alpha-particle emitter At-211 compared with Co-60 irradiation. Int. J. Rad. Biol. 89(4):250-258; 2013.

Dashko EA, Kizhaev EV, Yuminov OA, Tultaev AV, Eremenko DO, Platonov SY, Fotina OV, Pankratova TV. Estimating equivalent doses of internal radiation for the alpha-emitting radiopharmaceutical astatine-211. Bulletin Russian Acad Sci: Physics 74(11):1591-1594; 2010.

Decristoforo C, Siller R, Chen F, Riccabona G. Radiochemical purity of routinely prepared (99m)Tc radiopharmaceuticals: a retrospective study. Nucl Med Communications 21(4):349-354; 2000.

Elgqvist J, Andersson H, Back T, Hultborn R, Jensen H, Karlsson B, Lindegren S, Palm S, Warnhammar E, Jacobsson L. Therapeutic efficacy and tumor dose estimations in radioimmunotherapy of interperitoneally growing OVCAR-3 cells in nude mice with At-211-labeled mAb MX35. J Nucl Med 46:1907-1915; 2005.

Elgqvist J, Andersson H, Back T, Claesson I, Hultborn R, Jensen H, Johansson BR, Lindegren S, Olsson M, Palm S, Warnhammar E, Jacobsson L. Alpha-radioimmunotherapy of intraperitoneally growing OVCAR-3 tumors of variable dimensions: outcome related to measured tumor size and mean absorbed dose. J Nucl Med 47:1342-1350; 2006a.

Elgqvist J, Andersson H, Bernhardt P, Back T, Claesson I, Hultborn R, Jensen H, Johansson BR, Lindegren S, Olsson M, Palm S. Administered activity and metastatic cure probability during radioimmunotherapy of ovarian cancer in nude mice with (211)At-MX35F(ab')2. Int J Radiat Oncol Biol Phys 66(4):1228-1237; 2006b.

Elgqvist J, Andersson H, Back T, Claesson I, Hultborn R, Jensen H, Lindegren S, Olsson M, Palm S, Warnhammer E, Jacobsson L. Fractionated radioimmunotherapy of intraperitoneally growing ovarian cancer in nude mice with (211)At-MX35F(ab')2: therapeutic efficacy and myelotoxicity. Nucl Med Biol 33(8):1065-1073; 2006c.

Elgqvist J, Andersson H, Jensen H, Kahu H, Lindergren S, Warnhammer E, Hultborn R. Repeated intraperitoneal alpha-radioimmunotherapy of ovarian cancer in mice. J Oncology, 2010.

Eriksson SE, Back T, Elgstrom E, Jensen H, Nilsson R, Lindegren S, Tennvall J. Successful radioimmunotherapy of established syngeneic rat colon carcinoma with At-211-mAb. EJNMMI Res 3(1):23-32; 2013.

Eriksson SE, Elgstrom E, Back T, Ohlsson T, Jensen H, Nilsson R, Lindegren S, Tennvall J. Sequential radioimmunotherapy with (177)Lu- and (211)At-labeled monoclonal antibody BR96 in a syngeneic rat colon carcinoma model. Cancer Biother Radiopharm 29(6):238-246; 2014.

Ersahin D, Doddamane I, Cheng D. Targeted radionuclide therapy. Cancers 3:3838-3855; 2011.

Fischer MJE, de Mol NJ. Surface plasmon resonance. Methods in molecular biology 627. New York: Springer; 2010

Foulon CF, Adelstein SJ, Kassis AI. One-step synthesis of radioiodinated biotin derivatives. Biorganic Medicinal Chem Letters 6(7):779-784;1996.

Foulon CF, Schoutz BW, Zalutsky MR. Preparation and biological evaluation of an astatine-211 labeled biotin conjugate: biotinyl-3-[211At]astatoanilide. Nuc Med Biol 24(2):135-143; 1997.

Foulon CF, Alston KL, Zalutsky MR. Astatine-211-labeled biotin conjugates resistant to biotinidase for use in pretargeted radioimmunotherapy. Nucl Med Biol 25(2):81-88; 1998.

Frens G. Controlled nucleation for the regulation of the particle size and concentration of gold nanoparticles from UV-Vis spectra. Nature Phys Sci 241:20-22; 1973.

Friedman AM, Zalutsky MR, Wung W, Buckingham F, Harper PV Jr., Scherr GH, Wainer B, Huster RL, Appelman EH, Rothberg RM, Fitch FW, Stuart FP, Simonian SJ. Preparation of a biologically stable and immunogenically competent astatinated protein. Int J Nucl Med Biol 4:219; 1977.

Frier M, Hesslewood SR. Quality assurance of radiopharmaceuticals. Nucl Med Communications. 12(7):1-58; 1980.

Frost SHL, Back T, Chouin N, Hultborn R, Jacobsson L, Elgqvist J, Jensen H, Albertsson P, Lindegren S. Comparison of At-211-PRIT and At-211-RIT of ovarian microtumors in a nude mouse model. Cancer Biother Radiopharm 28(2):108-114; 2013.

Garg PK, Harrison CL, Zalutsky MR. Comparative tissue distribution in mice of the alpha-emitter (211)At and (131)I labels of a monoclonal antibody and F(ab')2 fragment. Cancer Res 50(12):3514-3520; 1990.

Giljohann DA, Seferos DS, Daniel WL, Massich MD, Patel PC, Mirkin CA. Gold nanoparticles for biology and medicine. Ang Chem 49(19):3280-3294; 2010.

Groppi F, Bonardi ML, Birattari C, Menapace E, Abbas K, Holzwarth U, Alfarano A, Morzenti S, Zona C, Alfassi ZB. Optimisation study of alpha-cyclotron production of At-211/Po-211g for high-let metabolic radiotherapy purposes. Appl Radiat Isot 63:621-31; 2005.

Guerard F, Gestin JF, Brechbiel MW. Production of (211)At-astatinated radiopharmaceuticals and applications in targeted alpha-particle therapy. Cancer Biother Radiopharm 28(2):1-20; 2013.

Gustaffson AM, Back T, Elgqvist J, jacobsson L, Hultborn R, Albertsoon P, Morgenstern A, Bruchertseifer F, Jensen H, Lindegren S. Comparison of therapeutic efficacy and biodistribution of (213)Bi and (211)At-labelled monoclonal antibody MX35 in an ovarian cancer model. Nucl Med Biol 39(1):15-22; 2012.

Hadley SW, Wilbur DS, Gray MA, Atcher RW. Astatine-211 labeling of an antimelanoma antibody and its Fab fragment using N-succinimidyl p-[211At] astatobenzoate: comparisons in vivo with the p-[125I] iodobenzyoyl conjugate. Bioconjugate Chem 2(3):171-179; 1991.

Hainfeld JF, Slatkin DN, Smilowitz HM. The use of gold nanoparticles to enchance radiotherapy in mice. Phys Med Biol 49(18):N309-N315; 2004.

Haiss W, Thanh NTK, Aveyard J, Fernig DG. Determination of size and concentration of gold nanoparticles from UV-Vis spectra. Anal Chem 79:4215-4221; 2007.

Hamoui ZB. In vitro cytotoxicity of (198)Au-NP labeled HIV-1 Tat CPP for the treatment of metastatic breast cancer. College Station, TX: Texas A&M University; 2015. Thesis.

Hamwi W, Fischer S, Lohs G, Huebner S, Brueckner R, Odrich H, Taut T. Optimization of the synthesis of At-211 by the Bi-209(alpha,2n)At-211 nuclear reaction and the nuclear physical characterization of astatine preparations. ZFI-MITT 165:18-25; 1991.

Hauck ML, Larsen RH, Welsh PC, Zalutsky MR. Cytotoxicity of alpha-particle-emitting astatine-211-labelled antibody in tumour spheroids: no effect of hyperthermia. Brit J Cancer 77(5):753; 1998.

Henriksen G, Messelt S, Olsen E, Larsen RH. Optimisation of cyclotron production parameters for the Bi-209(alpha, 2n) At-211 reaction related to biomedical use of at-211. Appl Radiat Isotopes 54:839-844; 2001.

Hermanne A, Tarkanyi F, Takacs S, Szucs Z, Shubin YN, Dityuk AI. Experimental study of the cross-sections of alpha-particle induced reactions on Bi-209. Appl Radiat Isot 63:1-9; 2005.

Hoffman TJ, Quinn TP, Volkert WA. Radiometallated receptor-avid peptide conjugates for specific in vivo targeting of cancer cells. Nucl Med Biol 28: 527-539; 2001.

Hopkins K, Chandler C, Eatough J, Moss T, Kemshead JT. Directed injection of Y-90 moabs into glioma tumor resection cavities leads to limited diffusion of the radioimmunoconjugates into normal brain parenchyma: a model to etimate absorbed radiation dose. Int J Radiat Oncol Biol Phys 40:835-844; 1998.

Hull S, Roberson M. Effluent considerations with At-211 production. Proceedings from Health Physics Society meeting. Scottsdale; 2011.

International Atomic Energy Agency. Directory of cyclotrons used for radionuclide produciton member states – 2006 update. Vienna: International Atomic Energy Agency; 2006.

International Atomic Energy Agency. Cyclotron produced radionuclides: Physical characteristics and production methods. Technical report series no. 468. Vienna: International Atomic Energy Agency; 2009a.

International Atomic Energy Agency. Cyclotron produced radionuclides: Principles and Practice. Technical report series no. 465. Vienna: International Atomic Energy Agency; 2009b.

International Atomic Energy Agency. Cyclotron produced radionuclides: Guidelines for setting up a facility. Technical report series no. 471. Vienna: International Atomic Energy Agency; 2009c.

International Commission on Radiation Units and Measurements. Conversion coefficients for use in radiological protection against external radiation. Bethesda, Md.: International Commission on Radiation Units and Measurements; 1998.

Ishii T, Otsuka H, Kataoka K, Nagasaki Y. Preparation of functionally PEGylated gold nanoparticles with narrow distribution through autoreduction of auric cation by alpha-Biotinyl-PEG-*block*-[poly(2-(N,N-dimethylamino)ethyl methacrylate)]. Langmuir 20(3):561-564; 2004.

JANIS [database]. Nuclear Energy Agency, Organisation for Economic Co-operation and Development; 2016.

Jazayeri MH, Amani H, Pourfatollah AA, Avan A, Ferns GA, Pazoki-Toroudi H. Enhanced detection sensitivity or prostate-specific antigen via PSA-conjugated gold nanoparticles based on localized surface plasmon resonance: GNP-coated anti-PSA/LSPR as a novel approach for the identification of prostate anomalies. Cancer Gene Ther 23(10):365-369; 2016.

Jokerst JV, Lobovkina T, Zare RN, Gambhir SS. Nanoparticle pegylation for imaging and therapy. Nanomedicine 6:715-28; 2011.

Kang B, Mackey MA, El-Sayed MA. Nuclear targeting of gold nanoparticles in cancer cells induces DNA damage, causing cytokinesis arrest and apoptosis. J Am Chem Soc 132:1517-1519; 2010.

Kannan R, Rahing V, Cutler C, Pandrapragada R, Katti KK, Kattumuri V, Robertson JD, Casteel SJ, Jurisson S, Smith C, Boote E, Katti KV. Nanocompatible chemistry toward fabrication of target-specific gold nanoparticles. J Am Chem Soc 128:11342-11343; 2006.

Kennel SJ, Mirzadeh S, Eckelman WC, Waldmann TA, Garmestani K, Yordanov AT, Stabin MG, Brechbiel MW. Vascular-targeted radioimmunotherapy with the alpha-particle emitter At-211. Rad Res 157:633-641; 2002.

Kim G, Chun K, Park SH, Kim B. Production of alpha-particle emitting At-211 using 45 MeV alpha-beam. Phys Med Biol 59:2849-2860; 2014.

Kim YH, Jeon J, Hong SH, Rhim WK, Lee YS, Youn H, Chung JK, Lee MC, Lee DS, Kang KW, Nam JM. Tumor targeting and imaging using cyclic RGD-PEGylated gold nanoparticle probes with directly conjugated iodine-125. Small 7(14):2052-2060; 2011.

Knoll GF. Radiation detection and measurement, 3rd ed. New York: Wiley; 2000.

Koning AJ, Hilaire S, Duijvestijn MC. Talys-1.0. Proceedings Int Conf Nucl Data Sci Tech 1:211-214; 2008.

Kumar S, Aaron J, Sokolov K. Directional conjugation of antibodies to nanoparticles for synthesis of multiplexed optical contrast agents with both delivery and targeting moieties. Nature Protocols 3(2):314-320; 2008.

Lambrecht RM, Mirzadeh S. Cyclotron isotopes and radiopharmaceuticals-XXXV-Astatine-211. Int J Appl Radiat Isot 36:43-450; 1985.

Langen B, Rudqvist N, Parris TZ, Schuler E, Spetz J, Helou K, Forssell-Aronsson E. Transcriptional response in normal mouse tissues after i.v. (211)At administration – response related to absorbed dose, dose rate, and time. EJNMMI Res 5(1):1-12; 2015.

Larsen RH, Hassfjell SP, Hoff P, Alstad J, Olsen E, Vergote IB, DeVos LN, Rgrum JBJ, Nustad K. (211)At labelling of polymer particles for radiotherapy: synthesis, purification, and stability. J Labelled Comp Radiopharm 33(1):977-986; 1993.

Larsen RH, Hoff P, Vergote IB, Bruland OS, Aas M, De Vos L, Nustad K. Alpha-particle radiotherapy with (211)At-labeled monodisperse polymer particles, (211) At-labeled IgG proteins, and free (211)At in a murine intraperitoneal tumor model. Gynelogic Oncol 57(1):9-15; 1995.

Larsen RH, Wieland BW, Zalutsky MR. Evaluation of an internal cyclotron target for the production of (211)At via the (209)Bi (alpha,2n) (211)At reaction. Appl Radiat Isto 47:135-43; 1996.

Larsen RH, Akabani G, Welsh P, Zalutsky MR. The cytotoxicity and microdosimetry of astatine-211-labeled chimeric monoclonal antibodies in human glioma and melanoma cells in vitro. Rad Res 149(20):155-162; 1998a.

Larsen RH, Bruland OS. Intratumor injection of immunoglobulins labelled with the alpha-particle emitter (211)At: analyses of tumor retention, microdistribution and growth delay. Brit J Cancer 77(7):1115; 1998b.

Larsen RH, Slade S, Zalutsky MR. Blocking [211At]astatide accumulation in normal tissues: preliminary evaluation of seven potential compounds. Nucl Med Biol 25(4):351-357; 1998c.

Larsen RH, Murud KM, Akabani G, Hoff P. (211)At and (131)I labeled bisphosphonates with high in vivo stability and bone accumulation. J Nucl Med 40(7):1197; 1999.

Laune B, May D, Youngblood DH. The Texas A&M coupled-cyclotron system. IEEE Nucl Sci 30:1367-1370; 1983a.

Laune B, May DP, Rogers RC, Chapman WC, Walterscheid WJ, Derrig G, Tsien YL, Smelser P, Youngblood DH. Injection from the K500 superconducting cyclotron into the 88" cyclotron at Texas A&M. IEEE Nucl Sci 30:2111-2113; 1983b.

Lebeda O, Jiran R, Ralis J, Stursa J. A new internal target system for production of (211)At on the cyclotron U-120M. Appl Radiat Isot 63(1):49-53; 2005.

Lewis MR, Kao JY, Anderson ALJ, Shively JE, Raubitschek A. An improved method for conjugating monoclonal antibodies with *N*-hydroxysulfosuccinimidyl DOTA. Bioconjugate Chem 12(2):320-324; 2001.

Lindegren S, Back T, Jensen HJ. Dry-distillation of astatine-211 from irradiated bismuth targets: A time-saving procedure with high recovery yields. Appl Radiat Isot 55: 157-160; 2001.

Lindencrona U, Sillfors-Elverby Lea, Nilsson M, Forssell-Aronsson E. Adsorption and volatility of free (211)At and (125)I-. Appl Radiat Isot 62:395-403; 2005.

Liu X, Atwater M, Wang J, Hou Q. Extinction coefficient of gold nanoparticles with different sizes and different capping ligands. Colloids Surf B Biointerfaces 58:3-7; 2007.

Lyckesvard MN, Delle U, Kahu H, Lindegren S, Jensen H, Back T, Swanpalmer J, Elmroth K. Alpha particle induced DNA damage and repair in normal cultured thyrocytes of different proliferation status. Mutation Res 765:48-56; 2014.

Maeda E, Yokoyama A, Taniguchi T, Washiyama K, Nishinaka I. Extraction of astatine isotopes for development of radiopharmaceuticals using a Rn/At-211 generator. J Radioanal Nucl Chem 303:1465-1468; 2015.

Martin TM, Akabani G. Radiological safety concerns for the accelerator production of diagnostic and therapeutic radionuclides in a university setting. Health Phys 103:S209-S216; 2012.

Martin TM, Bhakta V, Al-Harbi A, Hackemack M, Tabacaru G, Tribble R, Shankar S, Akabani S. Preliminary production of At-211 at the Texas A&M University cyclotron institute. Health Phys 107:1-9; 2014.

McLendon RE, Archer GE, Larsen RH, Akabani G, Bigner DD, Zalutsky MR. Radiotoxicity of systemically administered (211)At-labelled human/mouse chimeric monoclonal antibody: a long-term survival study with histologic analysis. Int J Radiat Oncol Biol Phys 45(2):491-499;1999.

Mock BH, Winkle W, Vavrek MT. A color spot test for the detection of kryptofix 2.2.2 in (18)F-FDG preparations. Nucl Med Biol 24(2):193-195;1997.

Morzenti S, Bonardi ML, Groppi F, Zona C, Persico E, Menapace E, Alfassi ZB. Cyclotron production of (211)At/(211g)Po by (208)Bi(alpha,2n) reaction. J Radioanal Nucl Chem 276(3):843-847; 2008.

Nagatsu K, Minegishi K, Fukada M, Suzuki H, Hasegawa S, Zhang MR. Production of (211)At by a vertical beam irradiation method. Appl Rad Isot 94:363-371; 2014.

Nagatsu K, Suzuki H, Fukada M, Minegishi K, Tsuji A, Fukumura T. An alumina ceramic target vessel for the remote production of metallic radionuclides by in situ target dissolution. Nucl Med Biol 39:1281-1285; 2012.

Nagl MA, Barbosa MB, Vetter U, Correia JG, Hofsass HC. A new tool for the search of nuclides with properties suitable for nuclear solid state physics based on the Evaluated Nuclear Structure Data Files. Nucl Inst Meth A 726: 17-30; 2013.

Nakamae H, Wilbur DS, Hamlin DK, Thakar MS, Santos EB, Fisher DR, Kenoyer AL, Pagel JM, Press OW, Storb R, Sandmaier BM. Biodistributions, myelosuppression, and toxicities in mice treated with an anti-cd45 antibody labeled with the alpha-emitting radionuclides bismuth-213 or astatine-211. Cancer Res 69: 2408-2415; 2009.

National Nuclear Data Center [database]. Nuclear Decay Data in the MIRD Format. Upton, NY: National Nuclear Data Center, Brookhaven National Laboratory; 2016.

Nduom EK, Bouras A, Kaluzova M, Hadjipanayis CG. Nanotechnology applications for glioblastoma. Neurosurgery Clin N Amer 23:439-49; 2012.

Neti P V, Howell RW. Lognormal distribution of cellular uptake of radioactivity: statistical analysis of alpha-particle track autoradiography. J Nucl Med 49(6):1009-1016; 2008.

Ogata Y, Ishigure N, Mochizuki S, Ito K, Hatano K, Abe J, Miyahara H, Masumoto K, Nakamura H. Distribution of thermal neutron flux around a PET cyclotron. Health Phys 100(2):S60-S66; 2011.

Ogawa K, Mizuno Y, Washiyama K, Shiba K, Takahashi N, Kozaka T, Watanabe S, Shinohara A, Odani A. Preparation and evaluation of an astatine-211-labeled sigma receptor ligand for alpha radionuclide therapy. Nucl Med Biol 42:875-879; 2015.

Paciotti GF, Kingston DGI, Tamarkin L. Colloidal gold nanoparticles: a novel nanoparticle platform for developing multifunctional tumor-targeted drug delivery vehicles. Drug Development Res 67:47-54; 2006.

Palm S, Humm JL, Rundqvist R, Jacobsson L. Microdosimetry of astatine-211 single-cell irradiation: role of daughter polonium-211 diffusion. Med Phys 31(2):218-225;2004

Palm S, Back T, Claesson I, Danielsson A, Elgqvist J, Frost S, Hultborn R, Jensen H, Lindegren S, Jacobsson L. Therapeutic efficacy of astatine-211-labeled trastuzumab on radioresistant SKOV-3 tumors in nude mice. Int J Radiat Oncol Biol Phys 69(2):572-579; 2007.

Panchapakesan B, Wickstrom E. Nanotechnology for sensing, imaging, and treating cancer. Surgical Oncol Clin N Amer 16: 293-305; 2007.

Pandey MK, Byrne JF, Jiang H, Packard AB, DeGrado TR. Cyclotron production of (68)Ga via the (68)Zn(p,n)(68)Ga reaction in aqueous solution. Am J Nucl Med Mol Imag 4(4):303-310; 2014.

Pelowitz DB. Monte Carlo N-Particle eXtended (MCNPX) user's manual, version 2.6.0. Los Alamos, NM: Los Alamos National Laboratory; LA-CP-07-1473; 2008.

Pozzi OR, Zalutsky MR. Radiopharmaceutical chemistry of targeted radiotherapeutics, part 1: effects of solvent on the degradation of radiohalogen precursors by (211)At alpha-particles. J Nucl Med 46(4):700-706; 2005a.

Pozzi OR, Zalutsky MR. Radiopharmaceutical chemistry of targeted radiotherapeutics, part 2: radiolytic effects of (211)At alpha-particles influence N-succinimidyl 3-(211)At-astatobenzoate synthesis. J Nucl Med 46(8):1393-1400; 2005b.

Pozzi OR, Zalutsky MR. Radiopharmaceutical chemistry of targeted radiotherapeutics, part 3: alpha-particle-induced radiolytic effects on the chemical behavior of (211)At. J Nucl Med 48(7):1190-1196; 2007.

Pozzi OR, Zalutsky MR. Radiopharmaceutical chemistry of targeted radiotherapeutics, part 4: strategies for (211)At labeling at high activities and radiation doses of (211)At alpha-particles. Nucl Med Biol 46:43-49; 2017.

Pruszynski M, Lyczko M, Bilewicz A, Zalutsky MR. Stability and in vivo behavior of Rh[16aneS_4-diol](211)At complex: a potential precursor for astatine radiopharmaceuticals. Nucl Med Biol 42:439-445; 2015.

Rajerison H, Guerard F, Mougin-Degraef M, Bourgeois M, Cherel M, Barbet J, Faivre-Chauvet A, Gestin JF. Radioiodinated and astatinated NHC rhodium complexes: synthesis. Nucl Med Biol 41:e23-e29; 2014.

Raju MR, Eisen Y, Carpenter S, Inkret WC. Radiobiology of alpha particles: III. Cell inactivation by alpha-particle traversals of the cell nucleus. Rad Res 128(2):204-209; 1991.

Rayburn DC. Determination of response characteristics of the atomlab re-entrant ionization chamber. Melbourne, FL: Florida Institute of Technology; 2007. Thesis.

Reist CJ, Foulon CF, Alston K, Bigner DD, Zalutsky MR. Astatine-211 labeling of internalizing anti-EGFRvIII monoclonal antibody using N-succinimidyl 5-[211At] astato-3-pyridinecarboxylate. Nucl Med Biol 26(4):405-411; 1999.

Robinson MK, Shaller C, Garmestani K, Plascjak PS, Hodge KM, Yuan QA, Marks JD, Waldman TA, Brechbiel MW, Adams GP. Effective treatment of established human breast tumor xenografts in immunodeficient mice with a single dose of the alpha-emitting radioisotope astatine-211 conjugated to anti-HER2/neu diabodies. Clin Cancer Res 14(3):875-882; 2008.

Roeske JC, Stinchcomb TG. Relationships between cell survival and specific energy spectra for therapeutic alpha-particle emitters. Rad Res 145(3):268-273; 1996.

Roeske JC, Stinchcomb TG. The use of microdosimetric moments in evaluating cell survival for therapeutic alpha-particle emitters. Rad Res 151(1):31-38; 1999.

Roeske JC, Stinchcomb TG. Tumor control probability model for alpha-particle-emitting radionuclides. Rad Res 153(1):16-22; 2000.

Rosch F, Henninger J, Beyer G, Dreyer R. Optimization of bombardment conditions of the (209)Bi(alpha, 2n) cyclotron production of (211)At. J Radioanal Nucl Chem 96(3):319-331; 1985.

Rudqvist N, Parris TZ, Schuler E, Helou K, Forssell-Aronsson E. Transcriptional response of BALB/c mouse thyroids following in vivo astatine-211 exposure reveals distinct gene expression profiles. EJNMMI Res 2(32):1-12; 2012.

Rudqvist N, Spetz J, Schuler E, Parris TZ, Langen B, Helou K, Forssell-Aronsson E. Transcriptional response in mouse thyroid tissue after (211)At administration: effects of absorbed dose, initial dose-rate, and time after administration. Plos One 10(7):1-14; 2015.

Schneider CA, Rasband WS, Eliceiri KW. NIH Image to ImageJ: 25 years of image analysis. Nat Meth 9:671-675; 2012.

Schrijvers AH, Quak JJ, Uyterlinde AM, Walsum M van, Meijer CJ, Snow GB, van Dongen GA. mAb U36, a novel monoclonal antibody successful in immunotargeting of squamous cell carcinoma of the head and neck. Cancer Res 53(18):4383-4390; 1993.

Schultz MK, Hammond M, Cessna JT, Plascjak P, Norman B, Szajek L, Garmestani K, Zimmerman BE, Unterweger M. Assessing the (210)At impurity in the production of (211)At for radiotherapy by (210)Po analysis via isotope dilution alpha spectrometry. Applied Radiat Isot 64:1365-1369; 2006.

Schwarz UP, Plascjak P, Beitzel MP, Gansow OA, Eckelman WC, Waldmann TA. Preparation of (211)At-labeled humanized anti-tac using (211)At produced in disposable internal and external targets. Nucl Med Biol 25:89-93; 1998.

Scott BR. Health risk evaluations for ingestion exposure of humans to polonium-210. Dose-Response 5:94-122; 2007.

Sgouros G. Alpha-particles for targeted therapy. Advanced Drug Deliv Rev 60:1402-1406; 2008.

Sgouros G, Roeske JC, McDevitt MR, Palm S, Allen BJ, Fisher DR, Brill AB, Song H, Howell RW, Akabani G, Committee SM, Bolch WE, Brill AB, Fisher DR, Howell RW, Meredith RF, Sgouros G, Wessels BW, Zanzonico PB. MIRD pamphlet no. 22 (abridged): Radiobiology and dosimetry of alpha-particle emitters for targeted radionuclide therapy. J Nucl Med 51:311-328; 2010.

Siegel JA, Zimmerman BE, Kodimer K, Dell M, Simon WE. Accurate dose calibrator activity measurement of (90)Y-ibritumomab tiuxetan. J Nucl Med 45(3):450-454; 2004.

Smith EM. Properties, uses, radiochemical purity and calibration of Tc-99m. J Nucl Med 5(11):871-882; 1964.

Stacey WM. Nuclear reactor physics., 2nd ed. Weinheim: WILEY-VCH Verlag GmbH & Co. KGaA; 2004.

Talanov VS, Yordanov AT, Garmestani K, Milenic DE, Arora HC, Plascjak PS, Eckelman WC, Waldmann TA, Brechbiel MW. Preparation and in vivo evaluation of novel linkers for (211)At labeling of proteins. Nucl Med Biol 31(8):1061-1071; 2004.

Ting G, Chang CH, Wang HE. Cancer nanotargeted radiopharmaceuticals for tumor imaging and therapy. Anticancer Res 29:4107-4118; 2009.

Ting G, Chang CH, Wang HE, Lee TW. Nanotargeted radionuclides for cancer nuclear imaging and internal radiotherapy. J Biomed Biotechnol 2010:1-17; 2010.

Turkington TG, Zalutsky MR, Jaszczak RJ, Garg PK, Vaidyanathan G, Coleman RE. Measuring the astatine-211 distributions with SPECT. Phys Med Biol 38(8):1121-1130; 1993.

Unak T. Some microdosimetric data on astatine-211. Appl Radiat Isot 58:115-117; 2003.

U.S. Food and Drug Administration, Department of Health and Human Services Center for Drug Evaluation and Research. Guidance: Nonclinical evaluation of late radiation toxicity of therapeutic radiopharmaceuticals. Silver Springs, MD: U.S. FDA; 2011.

U.S. Food and Drug Administration, Department of Health and Human Services Center for Drug Evaluation and Research. Guidance: PET drugs - current good manufacturing practices. Silver Springs, MD: U.S. FDA; 2009.

U.S. Pharmacopeia 29, National Formulary 24. Rockville, MD: United States Pharmacopeial Convention; 2005.

Vaidyanathan G, Affleck DJ, Schottelius M, Wester H, Friedman HS, Zalutsky MR. Synthesis and evaluation of glycosylated octreotate analogues labeled with radioiodine and (211)At via a tin precursor. Bioconjugate 17:195-203; 2006.

Vaidyanathan G, Affleck DJ, Alston KL, Zhao XG, Hens M, Hunter DH, Babich J, Zalutsky MR. A kit method for the high level synthesis of [(211)At]MABG. Bioorg Med Chem 15:3430-3436; 2007.

Vaidyanathan G, Affleck DJ, Alston KL, Zalutsky MR. A tin precursor for the synthesis of no-carrier-added [*I]MIBG and [(211)At]MABG. J Label Comp Radiopharm 50:177-182; 2007.

Vaidyanathan G, Boskovitz A, Shankar S, Zalutsky MR. Radioiodine and At-211-labeled guanidinomethyl halobenzoyl octreotate conjugates: potential peptide radiotherapeutics for somatostation receptor-positive cancers. Peptides 25:2087-2097; 2004.

Vaidyanathan G, Larsen RH, Zalutsky MR. 5-[(211)At]Astato-2'-deoxyuridine, an {alpha}-particle-emitting endoradiotherapeutic agent undergoing DNA incorporation. Cancer Res 56(6):1204-1209; 1996.

Walicka MA, Vaidyanathan G, Zalutsky MR, Adelstein SJ, Kassis AI. Survival and DNA damage in Chinese hamster V79 cells exposed to alpha particles emitted by DNA-incorporated astatine-211. Rad Res 150(3):263-268; 1998.

Watanabe S, Ikeda H, Shimosegawa E, Kamiya T, Horitsugi G, Takahashi N, Shinohara A, Hatazawa J. Difference in thyroid uptake between astatine-211 and iodine-123 in normal rats: a comparative study between oral and intravenous administration. J Nucl Med 57(2):1446, 2016.

Wilbur DS, Vessella RL, Stray JE, Goffe DK, Blouke KA, Atcher RW. Preparation and evaluation of para-[211At] astatobenzoyl labeled anti-renal cell carcinoma antibody A6H F(ab')2. In vivo distribution comparison with para-[125I] iodobenzoyl labeled A6H F(ab')2. Nucl Med Biol 20(8):917-927; 1993.

Williams LE, DeNardo GL, Meredith RF. Targeted radionuclide therapy. Med Phy 35:3062-8; 2008.

Williamson AC. Solid target system for use on an 11 MeV cyclotron. Knoxville, TN: University of Tennessee Melbourne; 2010. Thesis.

Wunderlich G, Henke E, Iwe B, Franke WG, Fischer S, Dreyer R. Animal studies on the in vivo stability of (211)At-labelled albumin particles. Nucl Med Communications 7(4):211-214; 1986.

Yang YY, Lin RS, Liu N, Liao JL, Wei M, Jin JN. Astatine-211 labeling of protein using TCP as a bi-functional linker: Synthesis and preliminary evaluation in vivo and in vitro. J Radioanal Nucl Ch 288: 71-77; 2011.

Yordanov AT, Garmestani K, Zhang M, Zhang Z, Yao Z, Phillips KE, Herring B, Horak E, Beitzel MP, Schwarz UP, Gansow OA. Preparation and in vivo evaluation of linkers for (211)At labeling of humanized anti-Tac. Nucl Med Biol 28(7):845-856; 2001.

Yordanov AT, Pozzi O, Carlin S, Akabani G, Wieland B, Zalutsky MR. Wet harvesting of no-carrier-added (211)At from an irradiated (209)Bi target for radiopharmaceutical applications. J Radioanal Nucl Chem 262(3):593-599; 2004.

Youngblood DH. The Texas A&M K500 cyclotron. In: Taro Tamura Memorial Riken Symposium on Nuclear Collective Motion and Nuclear Reaction Dynamics. Singapore:52-63; 1990.

Youngblood DH. The Texas A&M K500 cyclotron facility. Nucl Instrum Meth B 56(7):991-995; 1991.

Yu S. Review of (18)F-FDG synthesis and quality control. Biomed Imaging Interv J 2(4): e57; 2006.

Zalutsky MR, Garg PK, Friedman HS, Bigner DD. Labeling monoclonal antibodies and f(ab')2 fragments with the alpha-particle-emitting nuclide astatine-211: Preservation of immunoreactivity and in vivo localizing capacity. Proc Nat Acad Sci 86:7149-53; 1989.

Zalustksy MR, McLendon RE, Garg PK, Archer GE, Schuster JM, Bigner DD. Radioimmunotherapy of neoplastic meningitis in rats using an alpha-particle-emitting immunoconjugate. Cancer Res 54(17):4719-4725; 1994.

Zalutsky MR, Stabin MG, Larsen RH, Bigner DD. Tissue distribution and radiation dosimetry of astatine-211-labeled chimeric 81C6, and alpha-particle-emitting immunoconjugate. Nucl Med Biol 24(3):255-261; 1997.

Zalutsky MR, Zhao XG, Alston KL, Bigner D. High-level production of alpha-particle-emitting (211)At and preparation of (211)At-labeled antibodies for clinical use. J Nucl Med 42:1508-1515; 2001.

Zalutsky MR. Targeted radiotherapy of brain tumors. Brit J Cancer 90:1469-1473; 2004.

Zalutsky MR, Reardon DA, Pozzi OR, Vaidyanathan G, Bigner DD. Targeted alpha-particle radiotherapy with (211)At-labeled monoclonal antibodies. Nucl Med Biol 34:779-785; 2007.

Zalutsky MR, Reardon DA, Akabani G, Coleman RE, Friedman AH, Friedman HS, McLendon RE, Wong TZ, Bigner DD. Clinical experience with alpha-particle emitting (211)At: Treatment of recurrent brain tumor patients with (211)At-labeled chimeric antitenascin monoclonal antibody 81c6. J Nucl Med 49:30-8; 2008.

Zalutsky MR, Pruszynski M. Astatine-211: Production and availability. Current Radiopharm 4:177-85; 2011.

Zanzonico P, Dauer L, St Germain J. Operational radiation safety for PET-CT, SPECT-CT, and cyclotron facilities. Health Phys 95:554-70; 2008.

Zhang M, Yao Z, Zhang Z, Garmestani K, Talanov VS, Plascjak PS, Yu S, Kim HS, Goldman CK, Paik CH, Brechbiel MW. Then anti-CD25 monoclonal antibody 7G7/B6, armed with the alpha-emitter (211)At, provides effective radioimmunotherapy for a murine model of leukemia. Cancer Res 66(16):8227-8232; 2006a.

Zhang Z, Zhang M, Garmestani K, Talanov VS, Plascjak PS, Beck B, Goldman C, Brechbiel MW, Waldmann TA. Effective treatment of a murine model of adult T-cell leukemia using (211)At-7G7/B6 and its combination with unmodified anti-Tac (daclizumab) directed toward CD25. Blood 108(3):1007-1012; 2006b.

Zhang M, Yao Z, Patel H, Garmestani K, Zhang Z, Talanov VS, Plascjak PS, Goldman CK, Janik JE, Brechbiel MW, Waldmann TA. Effective therapy of murine models of human leukemia and lymphoma with radiolabeled anti-CD30 antibody, HeFi-1. Proc Nat Acad Sci 104(20):8444-8448; 2007.

Ziegler JF, Ziegler MD, Biersack JP. Srim - the stopping and range of ions in matter. Nucl Instrum Meth B 268: 1818-1823; 2010.

Zona C, Bonardi ML, Groppi F, Morzenti S, Canella L, Persico E, Menapace E, Alfassi ZB, Abbas K, Holzwarth U, Gibson N. Wet-chemistry method for the separation of no-carrier-added 211At/211gPo from 209Bi target irradiated by alpha-beam in cyclotron. J Radioanal Nucl Chem 276(3):819-824; 2008.

APPENDIX A

DECAY DATA FOR SELECTED RADIONUCLIDES

Decay data and spectra are provided on the following pages for selected radionuclides. These data were generated by the code Nuclei, utilizing current (2017) Evaluated Nuclear Structure Data Files (ENSDF) (Nagl et al. 2013). These are provided to show gamma and x-ray emissions in a convenient format. Spectra are shown as arbitrary units of intensity as a function of photon energy.The presented radionuclides are listed below, with data on the following pages.

^{211}At and Daughters

1. ^{211}At→^{207}Bi
2. ^{211}At→^{211}Po
3. ^{207}Bi→^{207}Pb
4. ^{211}Po→^{207}Pb

^{210}At and Daughters

5. ^{210}At→^{206}Bi
6. ^{210}At→^{210}Po
7. ^{206}Bi→^{206}Pb
8. ^{210}Po→^{206}Pb

Background Radionuclides and Impurities

9. ^{40}K→^{40}Ar/^{40}Ca
10. ^{22}Na→^{22}Ne
11. ^{135}I→^{135}Xe

Calibration Radionuclides

12. ^{137}Cs→^{137}Ba
13. ^{133}Ba→^{133}Cs
14. ^{152}Eu→^{152}Sm

1. $^{211}At \rightarrow ^{207}Bi$

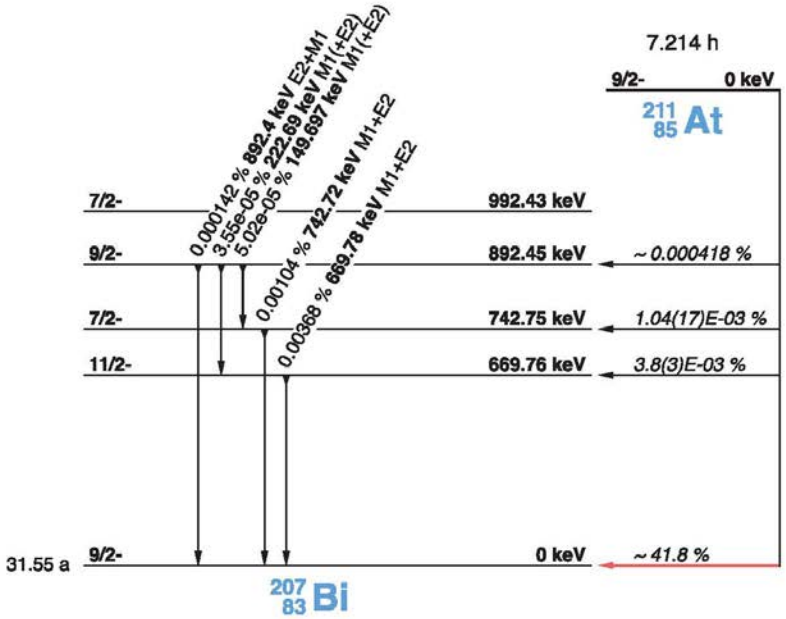

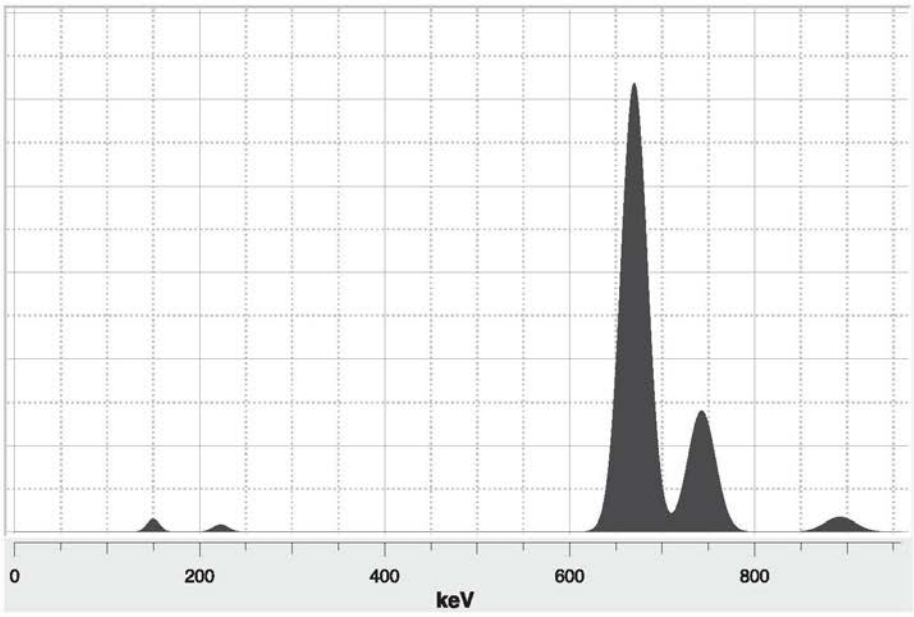

2. $^{211}At \rightarrow ^{211}Po$

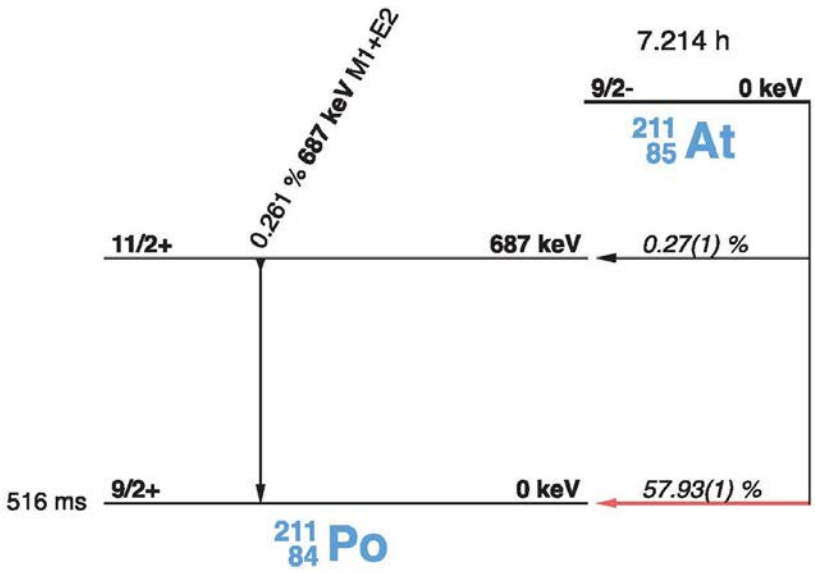

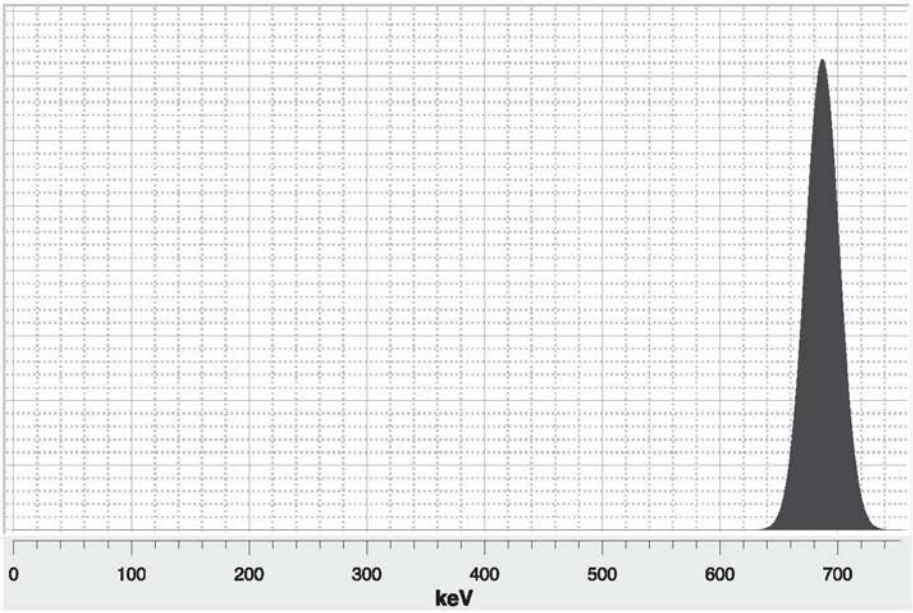

3. $^{207}Bi \rightarrow ^{207}Pb$

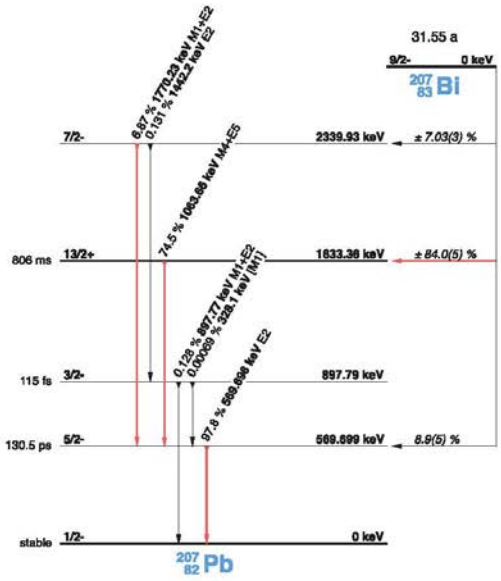

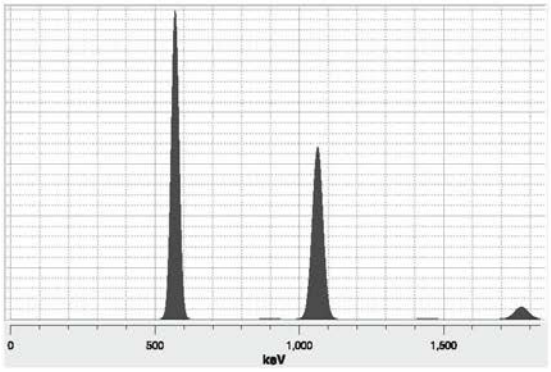

4. $^{211}Po \rightarrow {}^{207}Pb$

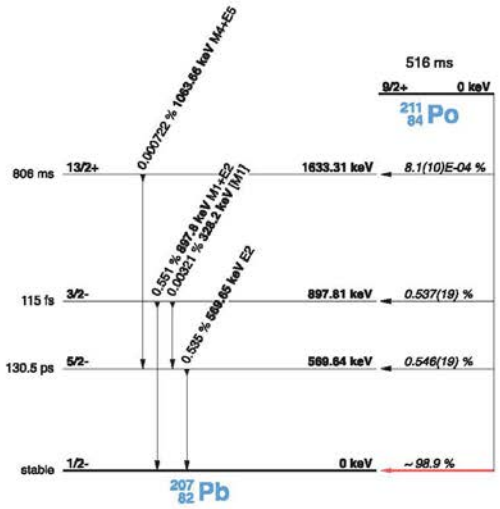

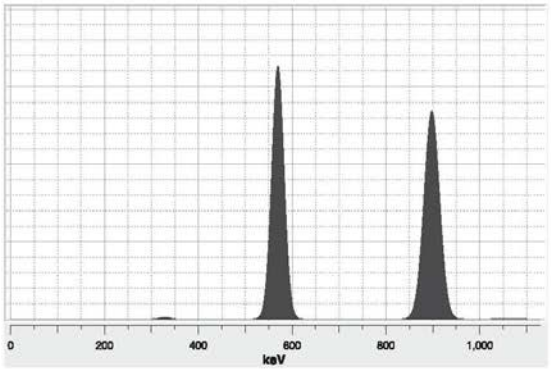

5. $^{210}At \rightarrow ^{206}Bi$

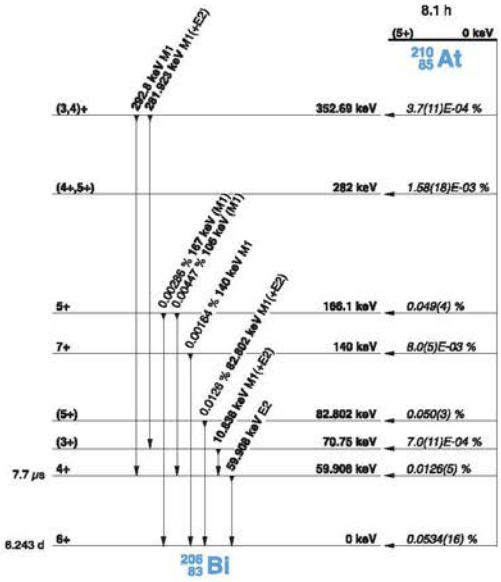

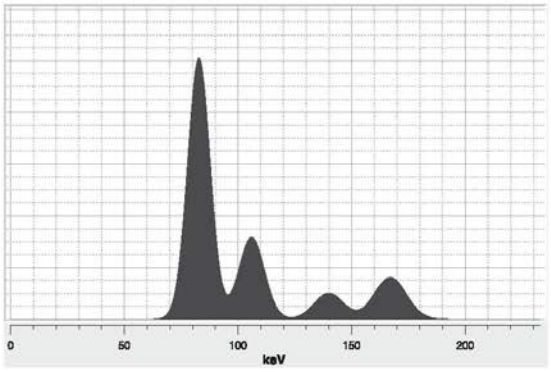

6. $^{210}At \rightarrow {}^{210}Po$

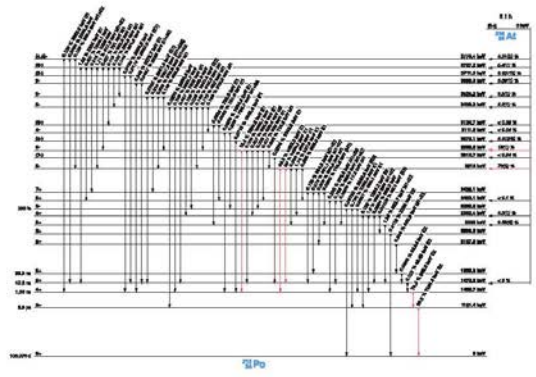

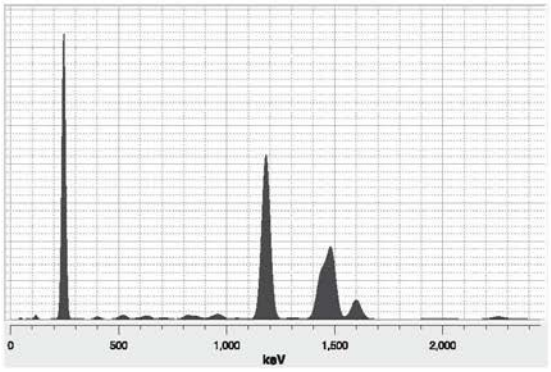

7. $^{206}Bi \rightarrow {}^{206}Pb$

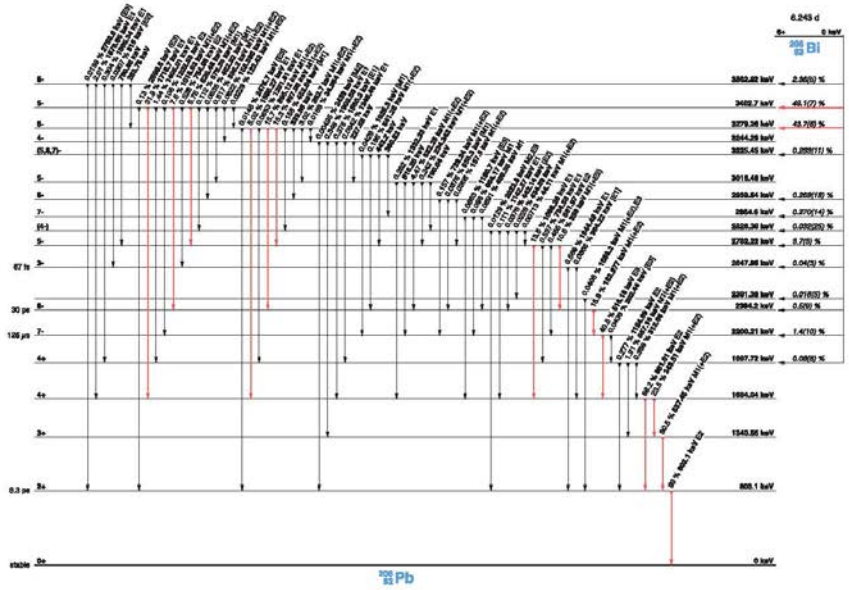

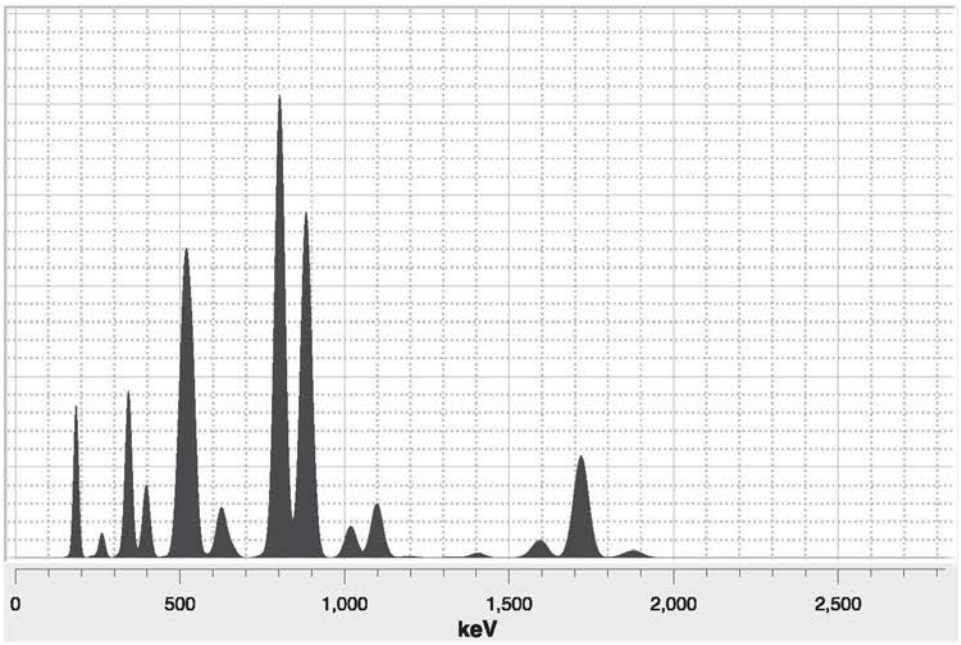

8. $^{210}Po \rightarrow {}^{206}Pb$

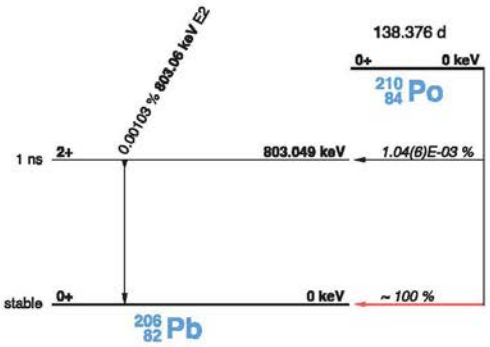

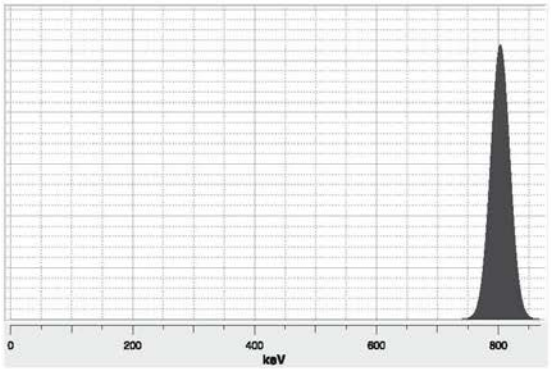

9. $^{40}K \rightarrow {}^{40}Ar/{}^{40}Ca$

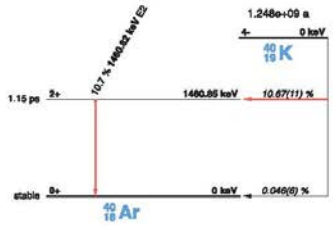

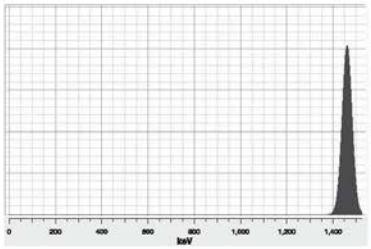

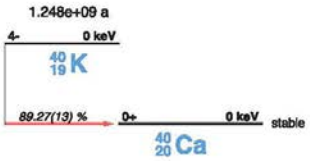

10. $^{22}Na \rightarrow {}^{22}Ne$

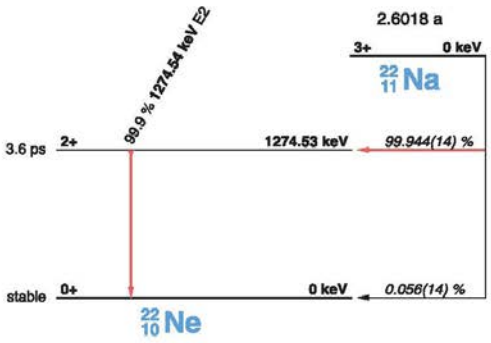

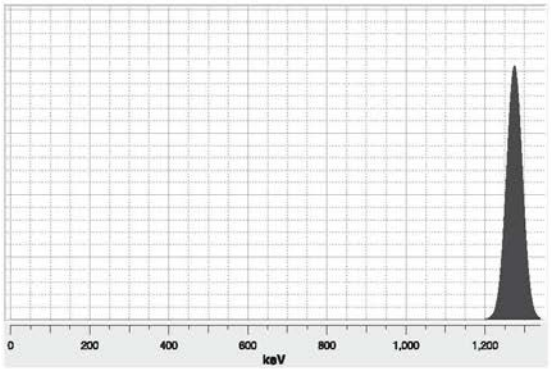

11. $^{135}I \rightarrow {}^{135}Xe$

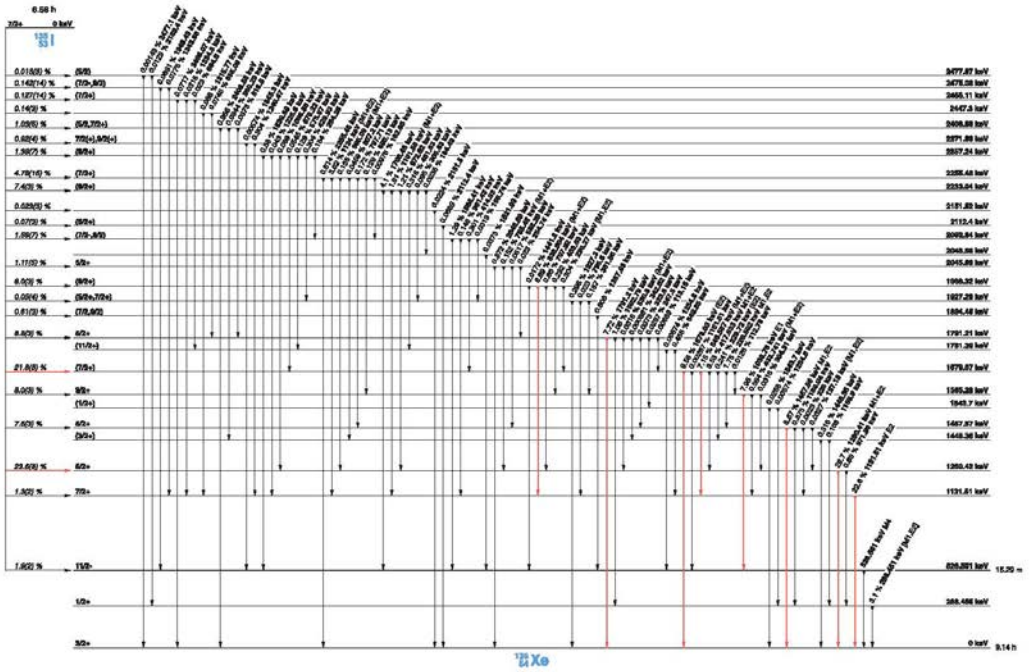

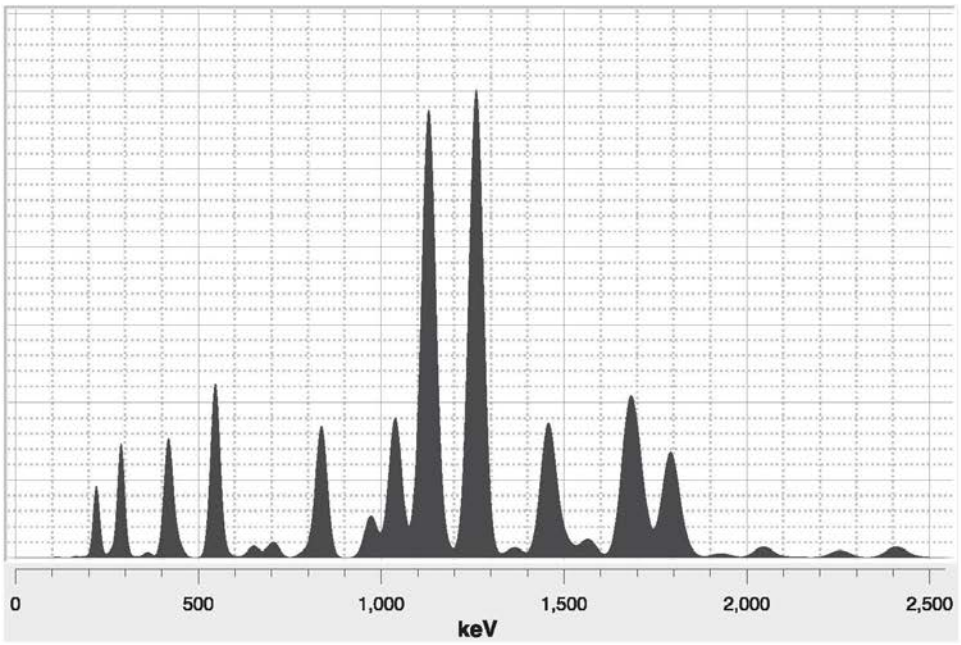

12. $^{137}Cs \rightarrow {}^{137}Ba$

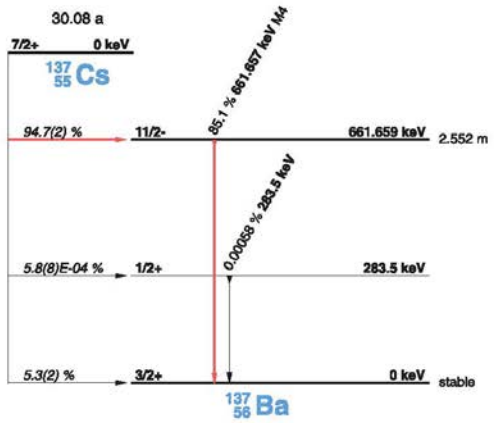

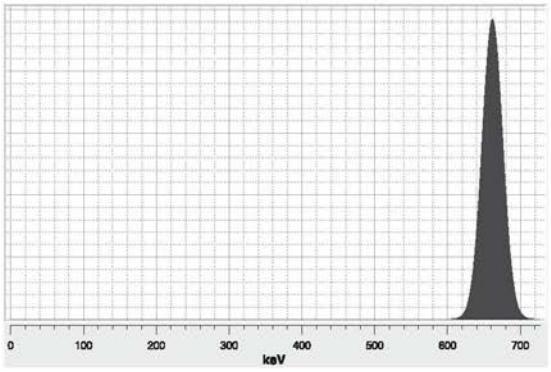

13. $^{133}Ba \rightarrow {}^{133}Cs$

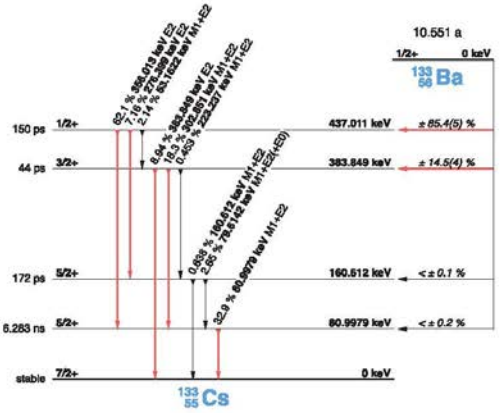

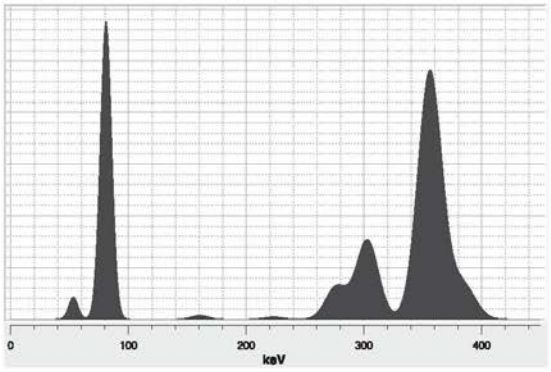

14. $^{152}Eu \rightarrow {}^{152}Sm$

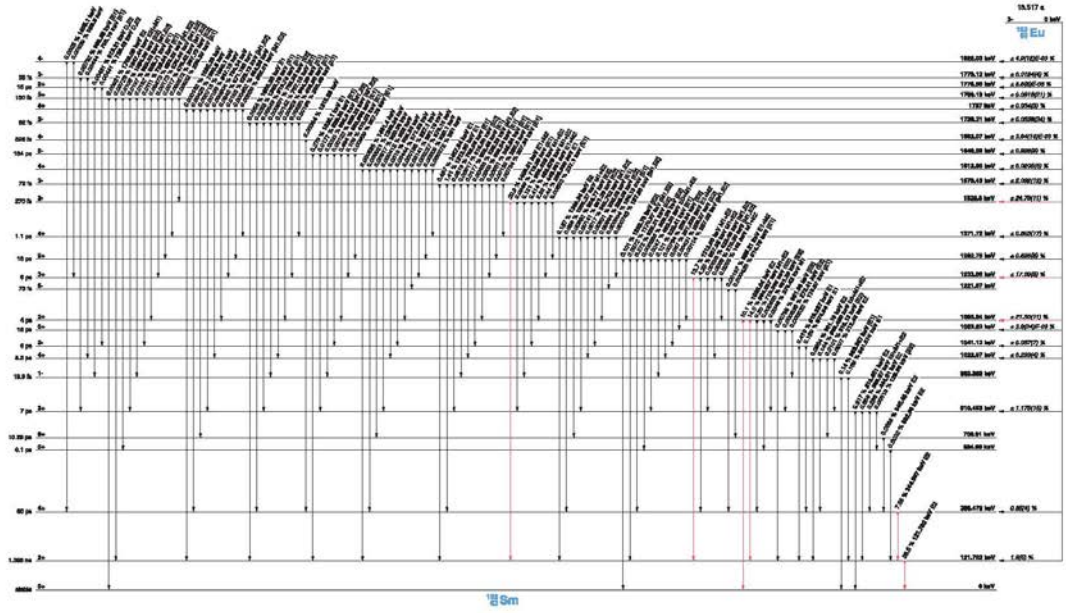

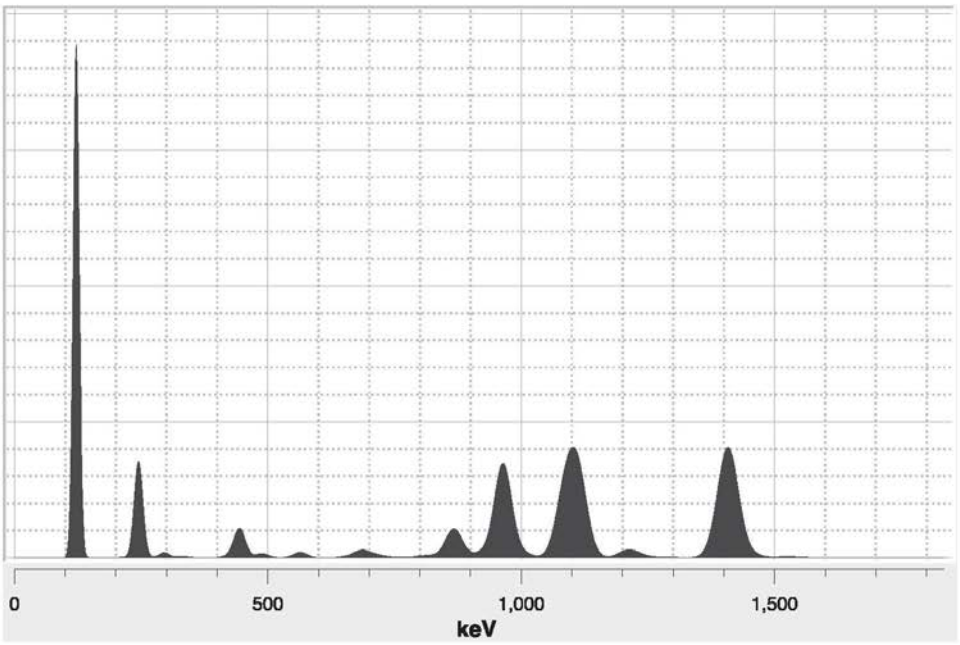

APPENDIX B

TALYS SIMULATION

The nuclear reaction code TALYS was used to simulate production yields and reaction channels for 26 MeV alpha particles incident on a pure ^{209}Bi thick target. A summary of results was presented in Section 2.2.3, Theoretical Yield. More detailed information is provided below. Figure B1 shows the number of nuclei of each reaction channel, normalized to ^{211}At, for a 4 h irradiation. Figure B2 shows the relative activity of all radioactive products for the same conditions. Selected portions of the TALYS input and output file is given following the figures.

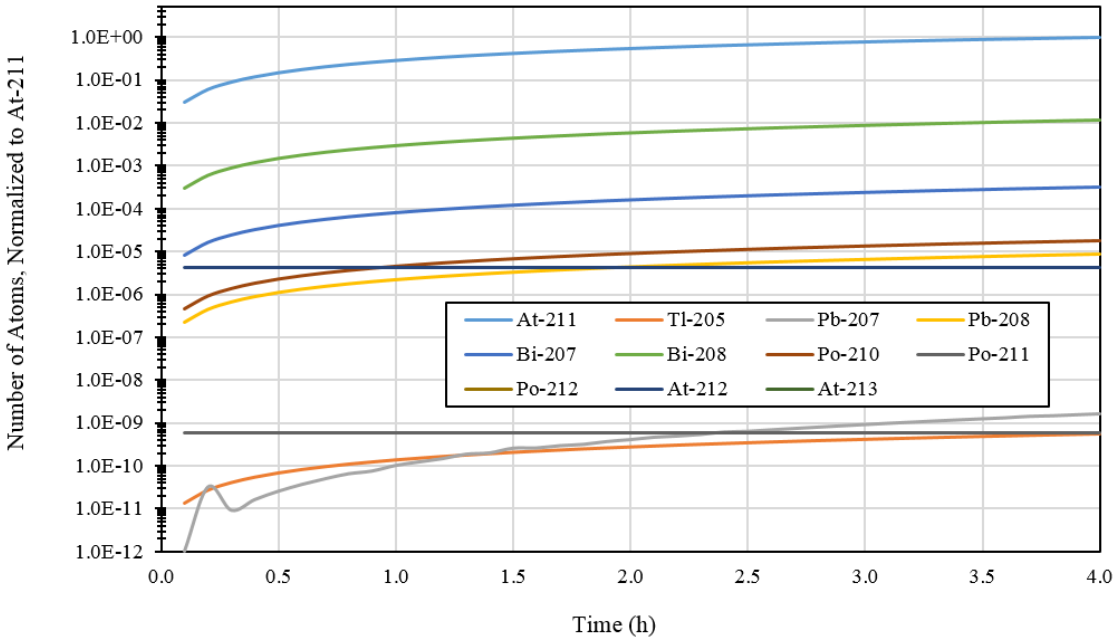

Number of impurity nuclei, normalized to ^{211}At nuclei, during a 4 h bombardment.

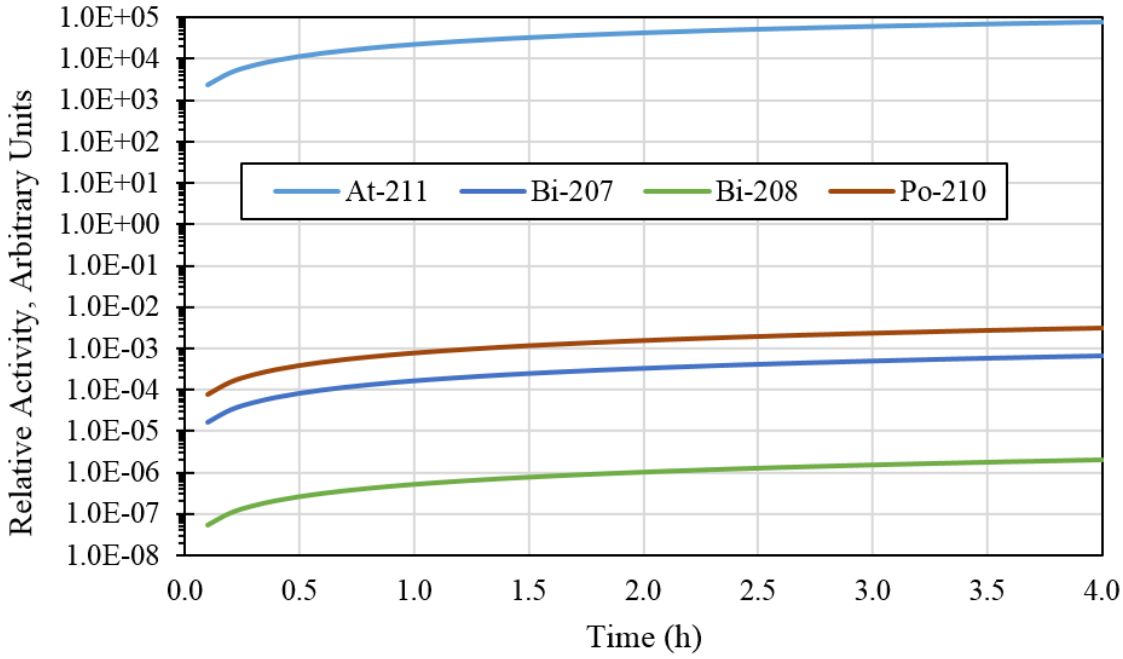

Relative product and impurity activity during a 4 h bombardment.

```
TALYS-1.8 (Version: December 28, 2015)

 Copyright (C) 2015  A.J. Koning, S. Hilaire and S. Goriely
                          NRG          CEA          ULB

 Dimensions - Cross sections: mb, Energies: MeV, Angles: degrees

 ########## USER INPUT ##########

 USER INPUT FILE

 #
 # general
 #
 projectile a
 element bi
 mass 209
 energy 1 30 0.5
 area 1
 rho 9.8
 #
 # spherical model
 #
 spherical y
 #
 # medical isotope production
 #
 production y
 ibeam 1
 ebeam 28.0
 eback 5.0
 radiounit mbq: megabecquerel
 tcool 0.1 d
 tirrad 4 h

 USER INPUT FILE + DEFAULTS

 Keyword           Value   Variable     Explanation

 #
 # Four main keywords
 #
 projectile          a     ptype0       type of incident particle
 element            Bi     Starget      symbol of target nucleus
 mass              209     mass         mass number of target
nucleus
 energy                    energyfile   file with incident energies
 #
 # Basic physical and numerical parameters
 #
 ejectiles g n p d t h a   outtype      outgoing particles
```

```
 maxz               12     maxZ         maximal number of protons
away from the initial compound nucleus
 maxn               32     maxN         maximal number of neutrons
away from the initial compound nucleus
 bins               40     nbins        number of continuum
excitation energy bins
 equidistant         n     flagequi     flag to use equidistant
excitation bins instead of logarithmic bins
 popmev              n     flagpopmev   flag to use initial
population per MeV instead of histograms
 segment             1     segment      number of segments to
divide emission energy grid
 maxlevelstar       30     nlevmax      maximum number of included
discrete levels for target
 maxlevelsres       10     nlevmaxres   maximum number of included
discrete levels for residual nucleus
 maxlevelsbin g     10     nlevbin      maximum number of included
discrete levels for gamma    channel
 maxlevelsbin n     10     nlevbin      maximum number of included
discrete levels for neutron  channel
 maxlevelsbin p     10     nlevbin      maximum number of included
discrete levels for proton   channel
 maxlevelsbin d      5     nlevbin      maximum number of included
discrete levels for deuteron channel
 maxlevelsbin t      5     nlevbin      maximum number of included
discrete levels for triton   channel
 maxlevelsbin h      5     nlevbin      maximum number of included
discrete levels for helium-3 channel
 maxlevelsbin a     30     nlevbin      maximum number of included
discrete levels for alpha    channel
 ltarget             0     ltarget      excited level of target
 isomer           1.00E+00 isomer       definition of isomer in
seconds
 transpower          5     transpower   power for transmission
coefficient limit
 transeps         1.00E-08 transeps     limit for transmission
coefficient
 xseps            1.00E-07 xseps        limit for cross sections
 popeps           1.00E-03 popeps       limit for population cross
section per nucleus
 Rfiseps          1.00E-03 Rfiseps      ratio for limit for fission
cross section per nucleus
 elow             1.00E-06 elow         minimal incident energy for
nuclear model calculations
 angles             90     nangle       number of angles
 anglescont         18     nanglecont   number of angles for
continuum
 anglesrec           1     nanglerec    number of recoil angles
 maxenrec           20     maxenrec     number of recoil energies
 channels            n     flagchannels flag for exclusive channels
calculation
```

```
 maxchannel          4     maxchannel   maximal number of outgoing
particles in individual channel description
 micro               n     flagmicro    flag for completely
microscopic Talys calculation
 best                n     flagbest     flag to use best set of
adjusted parameters
 bestbranch          y     flagbestbr   flag to use flag to use
only best set of branching ratios
 bestend             n     flagbestend  flag to put best set of
parameters at end of input file
 relativistic        y     flagrel      flag for relativistic
kinematics
 recoil              n     flagrecoil   flag for calculation of
recoils
 labddx              n     flaglabddx   flag for calculation of DDX
in LAB system
 recoilaverage       n     flagrecoilav flag for average velocity
in recoil calculation
 channelenergy       n     flagEchannel flag for channel energy for
emission spectrum
 reaction            y     flagreaction flag for calculation of
nuclear reactions
 astro               n     flagastro    flag for calculation of
astrophysics reaction rate
 astrogs             n     flagastrogs  flag for calculation of
astrophysics reaction rate with target in ground state only
 massmodel           2     massmodel    model for theoretical
nuclear mass
 expmass             y     flagexpmass  flag for using experimental
nuclear mass if available
 disctable           1     disctable    table with discrete levels
 production          y     flagprod     flag for isotope production
 outfy               n     flagoutfy    flag for output detailed
fission yield calculation
 gefran          50000     gefran       number of random events for
GEF calculation
 Estop            1000.000 Estop        incident energy above which
TALYS stops
 rpevap              n     flagrpevap   flag for evaporation of
residual products at high incident energies
 maxZrp             12     maxZrp       maximal number of protons
away from the initial compound nucleus before residual evaporation
 maxNrp             32     maxNrp       maximal number of neutons
away from the initial compound nucleus before residual evaporation
 #
 # Isotope production
 #
 Ebeam              28.000 beam         incident energy in MeV for
isotope production
 Eback               5.000 Eback        lower end of energy range
in MeV for isotope  production
```

```
 radiounit             mbq radiounit    unit for radioactivity
 yieldunit             num yieldunit    unit for isotope yield
 Ibeam               1.000 Ibeam        beam current in mA
 Tirrad              4     Tirrad       h of irradiation time
 Area                1.000 Area         target area in cm^2
 rho                 9.800 rhotarget    target density [g/cm^3]
 #
```

.....

```
Production of Z= 85 A=211 (211At) - Total

 Q-value    = -20.329056
 E-threshold=  20.718418

 Energy   Cross section

  1.00000E+00 0.00000E+00
  1.50000E+00 0.00000E+00
  2.00000E+00 0.00000E+00
  2.50000E+00 0.00000E+00
  3.00000E+00 0.00000E+00
  3.50000E+00 0.00000E+00
  4.00000E+00 0.00000E+00
  4.50000E+00 0.00000E+00
  5.00000E+00 0.00000E+00
  5.50000E+00 0.00000E+00
  6.00000E+00 0.00000E+00
  6.50000E+00 0.00000E+00
  7.00000E+00 0.00000E+00
  7.50000E+00 0.00000E+00
  8.00000E+00 0.00000E+00
  8.50000E+00 0.00000E+00
  9.00000E+00 0.00000E+00
  9.50000E+00 0.00000E+00
  1.00000E+01 0.00000E+00
  1.05000E+01 0.00000E+00
  1.10000E+01 0.00000E+00
  1.15000E+01 0.00000E+00
  1.20000E+01 0.00000E+00
  1.25000E+01 0.00000E+00
  1.30000E+01 0.00000E+00
  1.35000E+01 0.00000E+00
  1.40000E+01 0.00000E+00
  1.45000E+01 0.00000E+00
  1.50000E+01 0.00000E+00
  1.55000E+01 0.00000E+00
  1.60000E+01 0.00000E+00
  1.65000E+01 0.00000E+00
```

```
  1.70000E+01 0.00000E+00
  1.75000E+01 0.00000E+00
  1.80000E+01 0.00000E+00
  1.85000E+01 0.00000E+00
  1.90000E+01 0.00000E+00
  1.95000E+01 0.00000E+00
  2.00000E+01 0.00000E+00
  2.05000E+01 0.00000E+00
  2.10000E+01 3.48345E+00
  2.15000E+01 2.93709E+01
  2.20000E+01 6.53661E+01
  2.25000E+01 1.20925E+02
  2.30000E+01 1.89442E+02
  2.35000E+01 2.62839E+02
  2.40000E+01 3.37422E+02
  2.45000E+01 4.09195E+02
  2.50000E+01 4.74891E+02
  2.55000E+01 5.34939E+02
  2.60000E+01 5.92596E+02
  2.65000E+01 6.46036E+02
  2.70000E+01 6.95778E+02
  2.75000E+01 7.41376E+02
  2.80000E+01 7.84275E+02
  2.85000E+01 8.19960E+02
  2.90000E+01 8.48885E+02
  2.95000E+01 8.47699E+02
  3.00000E+01 8.29451E+02
```

.....

```
Summary of isotope production

 Maximal irradiation time    :   0 years   0 days   4 hours   0
minutes   0 seconds
 Cooling time                :   0 years   0 days   0 hours   0
minutes   0 seconds
 Energy range                :  28.000 -->   5.000 MeV
 Beam current                :       1.000 mA
 Target material density     :       9.800 g/cm^3
 Target area                 :       1.000 cm^2
 Effective target thickness  :       0.018 cm
 Effective target volume     :       0.018 cm^3
 Effective target mass       :       0.174 g
 Number of target atoms      :  5.01017E+20
 Number of incident particles:  3.12075E+15 s^-1
 Produced heat in target     :      23.000 kW

 Execution time:  0 hours  1 minutes  3.10 seconds
```